TOWARD CLINICAL TRANSLATION OF MICROVASCULAR ULTRASOUND IMAGING: ADVANCEMENTS IN SUPERHARMONIC ULTRASOUND TECHNOLOGY

Isabel G. Newsome

A dissertation submitted to the faculty at the University of North Carolina at Chapel Hill in partial fulfillment of the requirements for the degree of Doctor of Philosophy in the Department of Biomedical Engineering.

Chapel Hill
2021

Approved by:

Paul A. Dayton

David S. Lalush

Yueh Z. Lee

Gianmarco F. Pinton

Victoria L. Bautch

ABSTRACT

Isabel G. Newsome, Toward Clinical Translation of Microvascular Ultrasound Imaging: Advancements in Superharmonic Ultrasound Technology
(Under the direction of Paul A. Dayton)

Ultrasound imaging is perhaps the safest, most affordable, and most available biomedical imaging modality. However, it suffers from poor specificity for cancer detection, particularly in breast cancer, which affects one in eight women and leads to a high incidence of unnecessary biopsies from inconclusive screening. It is well-known that malignant cancers are accompanied by abnormal angiogenesis, leading to tortuous and disorganized vasculature. Acoustic angiography, a microvascular contrast-enhanced ultrasound technique, was developed to visualize and harness this aberrant vasculature as a biomarker of malignancy. This technique applies a dual-frequency superharmonic strategy to isolate intravascular microbubble contrast from the surrounding tissue with low-frequency transmit and high-frequency receive, resulting in high-resolution microvascular maps.

In preclinical research, acoustic angiography has been a valuable tool for differentiating tumors from healthy tissue by quantifying vascular features like tortuosity. The preclinical success of this technique is attributed to the single-element dual-frequency transducers used, which provide contrast sensitivity and focal depth best suited for imaging small animals at high microbubble doses. In an exploratory clinical study in which these transducers were used to image the human breast, imaging depth, low sensitivity, and motion artifacts significantly degraded image quality.

For acoustic angiography to be successfully translated to clinical use, the technique must be optimized for clinical imaging.

In this dissertation, we explore three ways in which acoustic angiography may be improved for the clinic. First, we evaluate microbubble contrast agents to determine the composition that maximizes superharmonic generation. The results indicate that lipid-shelled microbubbles with perfluorocarbon cores, like the commercial agent, DEFINITY, produce the greatest superharmonic signal. Then, we present a novel transducer, a stacked dual-frequency array, as the next-generation device for acoustic angiography and demonstrate improvements in imaging depth and sensitivity up to 10 mm and 13 dB, respectively. We go on to apply this device in a clinical pilot study and elucidate the challenges that remain to be overcome for clinical acoustic angiography. Finally, we propose custom simulations for superharmonic imaging and identify optimal frequency combinations for imaging at depths up to 8 cm, which can be used to design dedicated clinical dual-frequency arrays in the future.

To my husband, who has been my most steadfast support,

To my parents, who taught me the value of hard work and dedication,

To my teachers and mentors, who led me on this journey,

This is for you.

ACKNOWLEDGMENTS

This dissertation would have never been possible without the help of many, many people. I am incredibly grateful to my family for fostering my love of science since I was a little kid and to my husband, Cornell, for coming along on this ride with me. I deeply appreciate everyone who has supported me over the last five years, whether it was with a helping hand, some wise advice, or simply a cup of coffee.

To my thesis advisor, Paul Dayton – you have been a wonderful mentor. Thank you for believing in me as a wide-eyed college graduate and giving me countless opportunities to grow as a scientist and human being in your lab. I will forever be grateful for those experiences, from traveling to Europe (more than once!) to writing a textbook chapter and working with clinical patients. To the rest of my dissertation committee – David Lalush, Yueh Lee, Gianmarco Pinton, and Vicki Bautch – thank you for all your guidance. If I only absorbed a tiny bit of wisdom from each of you, that would be enough.

Thank you to the members of the Dayton Lab for always being supportive, willing to help each other, and ready to have a laugh. Research can be tough, and you all made it easier to soldier on through those times when things went wrong. I am especially grateful to Thomas Kierski, my lab partner in crime. Thom, thank you for always keeping a cool head when experiments went haywire, teaching me all things engineering, and being a great friend.

None of the work in this dissertation was completed alone. I have had the privilege to work with a myriad of collaborators on these projects, and I am so appreciative of all of you, especially those at Sunnybrook Research Institute and VisualSonics, as well as here at UNC and NCSU.

Finally, I am grateful for support from the National Institutes of Health through a predoctoral fellowship (F31CA24317) and through UNC's Integrative Vascular Biology training program (T32HL069768), which has given me the opportunity to become a more well-rounded scientist.

TABLE OF CONTENTS

LIST OF TABLES

LIST OF FIGURES

LIST OF ABBREVIATIONS

1D	One-dimension/one-dimensional
2D	Two-dimensions/two-dimensional
3D	Three-dimensions/three-dimensional
ASR	Angular spectrum with Rusanov nonlinearity
AUC	Area under the curve
BIRADS	Breast Imaging Reporting and Data System
B-mode	Brightness mode
CEUS	Contrast-enhanced ultrasound
CMUT	Capacitive micromachined ultrasonic transducer
CNR	Contrast-to-noise ratio
CT	Computed tomography
CTR	Contrast-to-tissue ratio
DAPC	Diarachidonoylphosphatidyl-choline
DF	Dual-frequency
DFA	Dual-frequency array
DFB	Decafluorobutane or C_4F_{10}

DF-mode	Dual-frequency mode
DPPA	Dipalmitoyl-phosphate
DPPC	Dipalmitoylphosphatidyl-choline
DPPE	Dipalmitoylphosphatidyl-ethanolamine
DSPC	Distearoylphosphatidyl-choline
DSPE	Distearoylphosphatidyl-ethanolamine
FDA	Food and Drug Administration
FWHM	Full-width at half-maximum
HF	High-frequency
LF	Low-frequency
MB	Microbubble
MCA	Microbubble contrast agent
MI	Mechanical index
MIP	Maximum intensity projection
MR	Magnetic resonance
NLC	Nonlinear contrast
OFP	Octafluoropropane or C_3F_8
PBS	Phosphate-buffered saline

PEG	Polyethylene glycol
PRF	Pulse repetition frequency
PSF	Point spread function
ROI	Region of interest
RF	Radiofrequency
SF_6	Sulfur hexafluoride
SIMB	Size-isolated microbubble
SNR	Signal-to-noise ratio
ULM	Ultrasound localization microscopy

LIST OF SYMBOLS

A	Attenuation and dispersion operator
A_{bubble}	Frequency spectrum of P_{bubble}
A_{tissue}	Frequency spectrum of P_{tissue}
A_{total}	Frequency spectrum of bubble population
β	Nonlinearity coefficient
c	Speed of sound [m/s]
$\bar{c_0}$	Mean speed of sound [m/s]
CNR	Contrast-to-noise ratio [dB]
D	Diffraction operator
$E_{contrast}$	Mean envelope amplitude inside contrast ROI
E_{tissue}	Mean envelope amplitude inside tissue ROI
$E_{tissue,max}$	Maximum of envelope amplitude of simulated tissue
$E_{total,max}$	Maximum of envelope amplitude of simulated bubble population
f	Frequency [Hz]
γ	Adiabatic polytropic gas exponent
κ_s	Shell surface viscosity [kg/s]

μ	Dynamic viscosity [Pa·s]
N	Nonlinearity operator
p	Acoustic pressure [Pa]
P_0	Ambient pressure [Pa]
P_{ac}	Acoustic driving pressure [Pa]
P_{bubble}	Pressure scattered by bubble [Pa]
P_{tissue}	Pressure scattered by tissue [Pa]
ϕ	Pseudo-potential
ρ	Density [kg/m^3]
r	Scattered distance [m]
R	Radius [m]
$\dot{R}$	Wall velocity [m/s]
$\ddot{R}$	Wall acceleration [m/s^2]
R_0	Initial radius [m]
$R_{break\text{-}up}$	Shell break-up radius [m]
$R_{buckling}$	Radius below which shell is buckled [m]
$R_{ruptured}$	Radius above which shell is ruptured [m]
σ	Surface tension [N/m]

$\sigma(R_0)$	Initial surface tension [N/m]
σ_w	Surface tension of water [N/m]
$\sigma_{break\text{-}up}$	Shell break-up surface tension [N/m]
τ	Retarded time [s]
t	Time [s]
W_n	Percentage weight for bubbles of size n
χ	Shell surface elasticity [N/m]

CHAPTER 1
INTRODUCTION TO MICROVASCULAR IMAGING[1]

1.1 Microvasculature in Cancer

Many diseases, such as cancer, are affected by aberrant microvasculature. To fuel their rapid growth, tumors induce angiogenesis, or the formation of new blood vessels from preexisting vasculature, by overexpressing pro-angiogenic factors (1,2). This tumor-associated neovascularization is considered one of the "hallmarks of cancer" (3) and results in vascular structures that differ greatly from those seen in healthy tissue – vessels are highly tortuous, leaky, disorganized, and densely packed, rather than linear and well-organized, as shown in **Figure 1.1** (1). The structural and functional abnormality observed in this microvasculature leads to increased interstitial pressure, acidosis, and hypoxia, which contribute in part to the difficulty of effectively treating cancer (4). This observation has motivated the development of anti-angiogenic therapies in an attempt to "normalize" the vasculature and hence improve treatment efficacy (4).

In addition, angiogenesis may serve as a biomarker of malignant disease as well as a therapeutic target. The increased microvascular density and tortuosity observed in and surrounding cancerous tumors might be used as both qualitative and quantitative metrics in the detection and

[1]Portions of this chapter previously appeared in an article in Ultrasound in Medicine and Biology. The original citation is as follows: Newsome IG, Dayton PA. "Visualization of Microvascular Angiogenesis Using Dual-frequency Contrast Enhanced Acoustic Angiography: A Review," *Ultrasound Med. Biol.* 2020;46(10):2625-2635. doi: 10.1016/j.ultrasmedbio.2020.06.009.

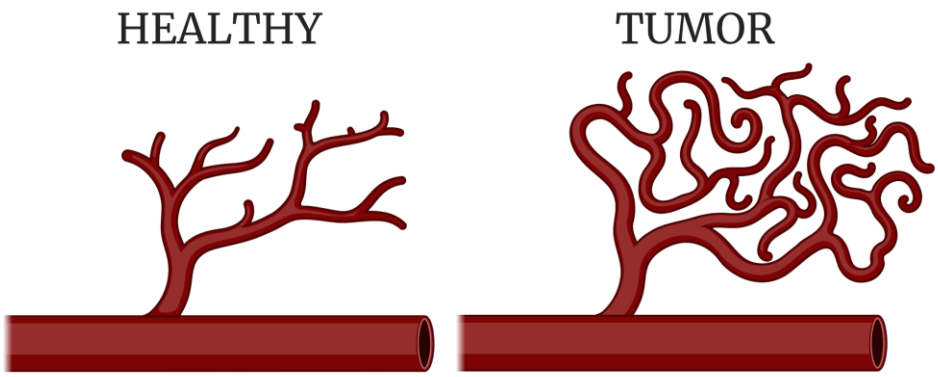

Figure 1.1 Schematic representation of the vascular differences between healthy and cancerous tissue. Figure created with Biorender.com.

diagnosis of these lesions. In order for this to be achieved, a diagnostic method must be able to image these vascular features with high resolution in three dimensions (3D).

In the clinic, angiography, or blood vessel imaging, is traditionally performed with computed tomography (CT) or magnetic resonance (MR) imaging (5). Although these modalities allow vascular imaging in three dimensions, they both present limitations when considered as tools for screening and monitoring disease progression or response to therapy. CT requires the use of ionizing radiation, while MR is time-intensive, and both modalities have limited resolution (~700 μm with the best currently approved clinical systems) (6,7). Neither of these imaging modalities is highly portable nor low cost. As such, there is a clinical need for high-resolution, safe, and accessible vascular imaging.

1.2 Biomedical Ultrasound Imaging

Since the 1960s, ultrasound techniques have been widely used for biomedical imaging (8), and today, ultrasound is arguably the safest, cheapest, and most available form of imaging beyond projection x-ray. Ultrasound imaging is based on the transmission and reception of sound waves. In conventional "B-mode" (brightness-mode) ultrasound, an acoustic wave with a specific frequency is transmitted into tissue from a transducer. As the wave propagates into the tissue,

portions are reflected back to the transducer. The amount of energy reflected depends on the acoustic impedance of the tissue, defined as the product of density and speed of sound. Differences in acoustic impedance between adjacent tissues lead to differing echoes reflected to the transducer, which are processed to form an ultrasound image (9). The frequency used for imaging governs both image resolution and penetration depth (due to frequency-dependent attenuation). Higher frequency results in better resolution but worse penetration depth, while lower frequency provides greater penetration depth at the cost of resolution (9). For clinical B-mode imaging, frequencies in the range of 1 – 10 MHz are typically used (10,11). In this frequency range, blood is effectively invisible on ultrasound images due to the size and impedance of red blood cells. In order to image blood vessels, more advanced techniques are necessary, such as Doppler or contrast-enhanced ultrasound (12,13).

1.2.1 Contrast-Enhanced Ultrasound and Microbubble Contrast Agents

Similar to contrast-enhanced CT or MR, contrast-enhanced ultrasound (CEUS) is a means of visualizing the presence of blood vessels by imaging an intravascular contrast agent in the bloodstream rather than blood itself. For ultrasound, this intravascular contrast is a solution of microbubbles. Microbubble contrast agents (MCAs) are composed of microscopic bubbles that are approximately 1 – 8 μm in diameter (14,15). These microbubbles typically consist of a high molecular weight gas core encapsulated by a lipid, protein, or polymer shell (14). Because they are similar in size to red blood cells, MCAs can circulate through the cardiovascular system anywhere that blood flows. MCAs typically remain in circulation for a few minutes before the core gas dissolves into the bloodstream, after which it is harmlessly expired by the lungs (15). The remaining shell components are cleared from circulation by the reticuloendothelial system of the liver and spleen (15).

MCAs provide acoustic contrast through two mechanisms. First, the impedance difference between the gas core of the microbubbles and the surrounding blood generates strong acoustic reflections. Second, due to their highly compressible core, microbubbles oscillate when exposed to ultrasound waves, producing broadband nonlinear echoes that span multiples of the excitation, or fundamental, frequency (14,16). Tissue behavior is quite distinct from that of MCAs, however. At low acoustic pressures, the energy contained in the ultrasonic echoes from tissue is concentrated at the fundamental frequency, whereas only a small portion of energy is contained within the harmonic frequencies (17). While nonlinear propagation of the acoustic wave causes more energy to shift to the harmonics as the transmitted acoustic pressure is increased, this effect is small at typical parameters used for contrast imaging (11,17).

Traditional CEUS techniques therefore enhance MCAs in the bloodstream over tissue by selectively receiving at the second harmonic, or twice the fundamental frequency, where there is relatively more MCA signal than tissue signal (18). Multi-pulse sequences, such as amplitude modulation or pulse inversion, are often used to further improve this enhancement (19,20). Because second harmonic techniques can be implemented within the bandwidth of a single transducer, these CEUS methods are widely used in the clinic. However, they can suffer from poor sensitivity due to the presence of tissue background in addition to limited temporal and spatial resolution.

1.2.2 Superharmonic Imaging

Superharmonic imaging is a variant of CEUS that employs a strategy for separating signals from tissue and MCAs based on the superharmonic content of microbubble echoes. The broadband echoes generated at the third harmonic and above (*i.e.*, $\geq$ 3x the fundamental frequency) are known as the "superharmonic" microbubble response (21). By selectively receiving these higher

frequency signals, superharmonic imaging can achieve better resolution and contrast-to-tissue ratio (CTR) than conventional B-mode or second harmonic CEUS techniques (21,22). With this technique, increased resolution is provided by the higher frequencies detected, and improved CTR is due to the fact that tissue produces minimal superharmonic content, significantly less than at the second harmonic frequency.

However, implementing superharmonic imaging requires non-traditional transducer technology, as conventional ultrasound transducers have limited bandwidth, meaning they cannot effectively transmit and receive signals at both the fundamental and higher order harmonic frequencies. To achieve the necessary bandwidth for this technique, transducers with completely independent elements for excitation and reception are typically used. **Figure 1.2A** provides an idealistic illustration of this dual-frequency (DF) approach to superharmonic imaging in the frequency domain. In some previous studies, phased arrays have been designed with interleaved transmit and receive elements (21,23). Using one such transducer with 0.8 MHz transmit and 2.9 MHz receive, Bouakaz *et al.* (24) demonstrated high CTR with superharmonic imaging compared to second harmonic imaging in human contrast-enhanced echocardiography. Others have implemented confocal dual-element transducers *in vitro* (22,25). Kruse and Ferrara (22) performed superharmonic M-mode imaging with confocal pistons at 2.25 and 15 MHz for transmit and receive, respectively, while Guiroy *et al.* (25) designed a confocal device with 4 MHz transmit and 14 MHz receive and imaged in 2D by raster-scanning the transducer over the imaging target.

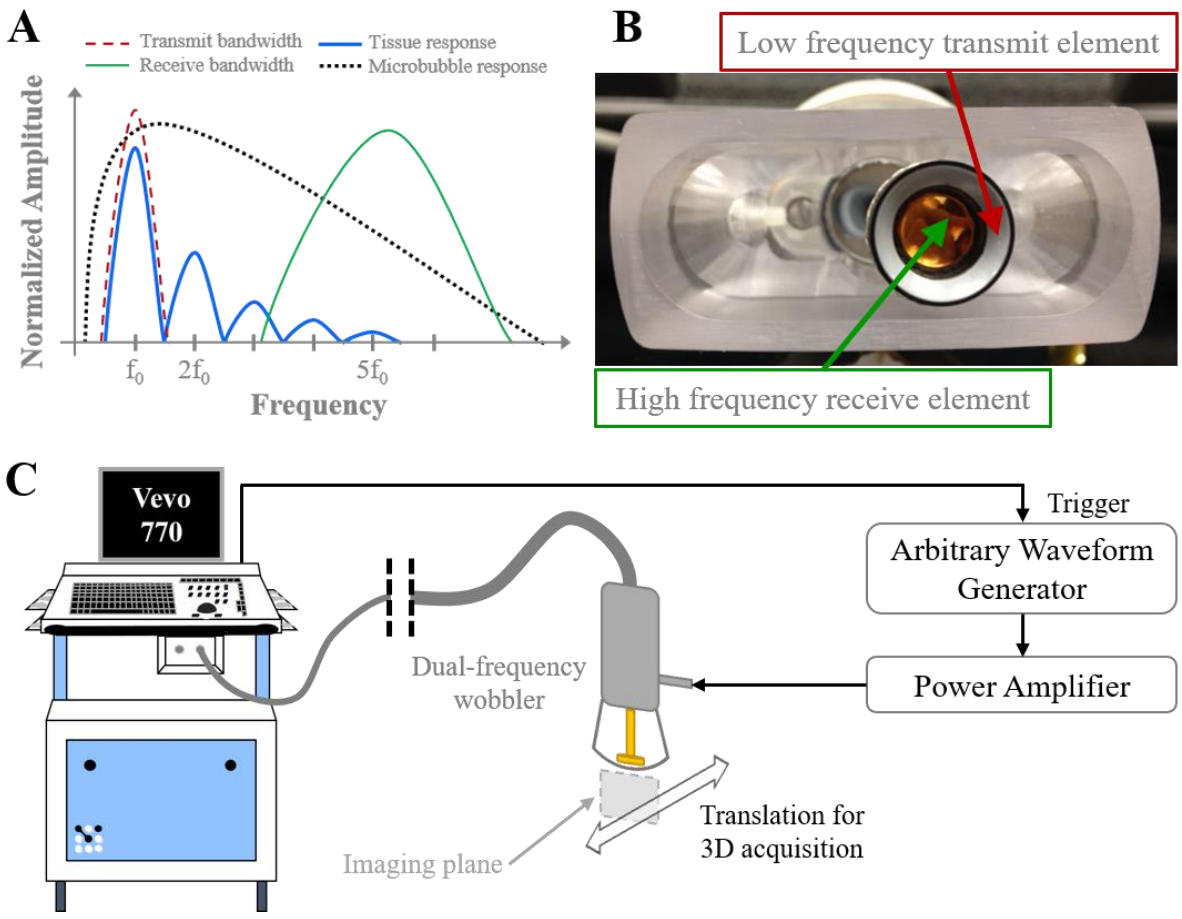

Figure 1.2 Description of acoustic angiography: **A)** Representation of the acoustic angiography technique in the frequency domain, where f_0 is the fundamental frequency, **B)** example of a dual-frequency wobbler transducer, and **C)** schematic diagram of the acoustic angiography imaging setup.

1.3 Acoustic Angiography

Acoustic angiography is a technique that applies superharmonic imaging in 3D to form volumetric maps of microvascular structures. Similar to the works mentioned above, to date, acoustic angiography has employed confocal dual-element transducers, comprised of a high-frequency central element surrounded by a low-frequency annular element, as shown in **Figure 1.2B**, allowing complete isolation of the excitation and reception bandwidths (26). These transducers are used to perform superharmonic imaging with transmit at 2 – 4 MHz on one transducer element and receive at 25 – 30 MHz on the second element (26,27). The transducer

elements are mechanically scanned on a motor-controlled arm, called a "wobbler," to form a 2D image (28). Acoustic angiography was initially performed with these custom transducers (modified RMV scanheads, FUJIFILM VisualSonics, Inc., Toronto, ON, Canada) and a preclinical high-frequency ultrasound system (Vevo 770, FUJIFILM VisualSonics, Inc., Toronto, ON, Canada). High-frequency B-mode and reception during dual-frequency imaging is controlled by this scanner, while low-frequency transmit is controlled by an arbitrary waveform generator (AWG2021, Tektronix, Inc., Beaverton, OR, USA) and power amplifier (model 240L, Electronics & Innovation, Ltd., Rochester, NY, USA). The DF wobbler probes used for acoustic angiography have a fixed focal depth of 13 – 16 mm and a depth of field of approximately 8 – 12 mm. To acquire 3D images, the transducer must be translated on a linear motion stage. A schematic of the acoustic angiography imaging setup is shown in **Figure 1.2C**.

With this system, acoustic angiography can resolve vessels on the order of 120 – 200 μm and displays CTR on the order of 20 dB *in vivo* (27,29,30). **Figure 1.3** provides example images of a subcutaneous fibrosarcoma tumor in a rat flank, including a high-frequency B-mode image (A), the corresponding 2D acoustic angiography slice (B), and three representations of the volumetric acoustic angiography dataset, including the dual-frequency image stack (C), a 3D rendering of the volume (D), and a maximum intensity projection (MIP) through depth (E).

1.3.1 Optimization of Acoustic Angiography

The amount of superharmonic signal generated by MCAs depends on both acoustic parameters of the excitation and characteristics of the microbubbles themselves (16), while the receive frequency bandwidth largely determines imaging depth, resolution, and sensitivity. Lindsey *et al.* (29) have studied the superharmonic response, examining CTR and resolution for various combinations of excitation frequency, pressure, and receive frequency. Their results

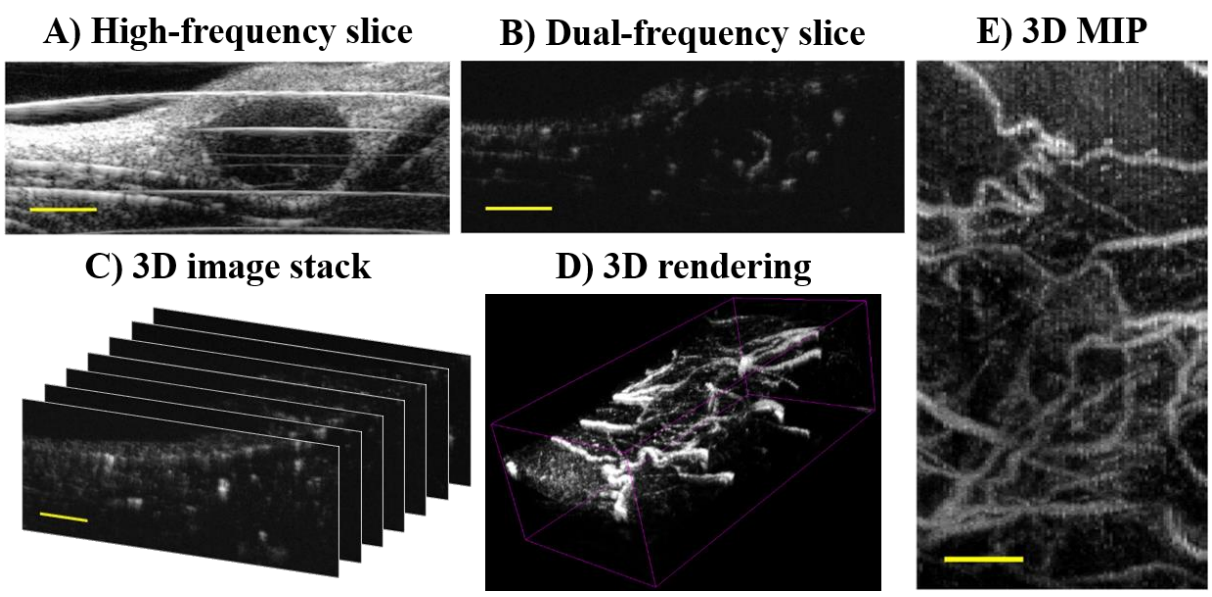

Figure 1.3 Example images of a subcutaneous rat fibrosarcoma tumor: **A)** high-frequency B-mode, **B)** 2D acoustic angiography slice, **C)** 3D acoustic angiography image stack, **D)** volumetric rendering of **(C)**, and **E)** maximum intensity projection (MIP) of **(C)**. Scale bar = 3 mm.

indicated that CTR is maximized for excitation frequencies between 1.5 – 3.5 MHz paired with reception frequencies between 10 – 15 MHz and confirmed that receive frequency is primarily responsible for determining resolution (29).

In a following study, Lindsey and colleagues (31) went on to explore the mechanism behind broadband superharmonic generation at various excitation frequencies and pressures. The authors found that the strongest signals were produced at high pressures that also resulted in microbubble fragmentation, although weaker superharmonic signals could be produced at pressures that were not immediately destructive to bubbles and usually correlated with slow bubble deflation or destruction over multiple pulses (31). This study demonstrated the importance of balancing excitation pressure and frame rate in order to maintain contrast signal throughout imaging. This effect is illustrated in **Figure 1.4**, which shows acoustic angiography MIPs of a subcutaneous fibrosarcoma tumor in a rat flank collected with two different pressures. At 1200 kPa incident pressure, microbubble destruction is dominant, resulting in an image of larger, fast-flowing

microvessels (**Figure 1.4A**). At 560 kPa, microbubbles persist through many pulses, emphasizing smaller, slow-flowing microvasculature (**Figure 1.4B**). It should be noted that the larger vessels are captured in both cases, but because the images are displayed as MIPs through depth, and there is relatively less signal at 560 kPa, the signal from the larger vessels is buried beneath the capillaries that are closer to the transducer in **Figure 1.4B**. Lindsey *et al.* (30) also showed that the shape of the low-frequency transmit pulse can be optimized for improved CTR.

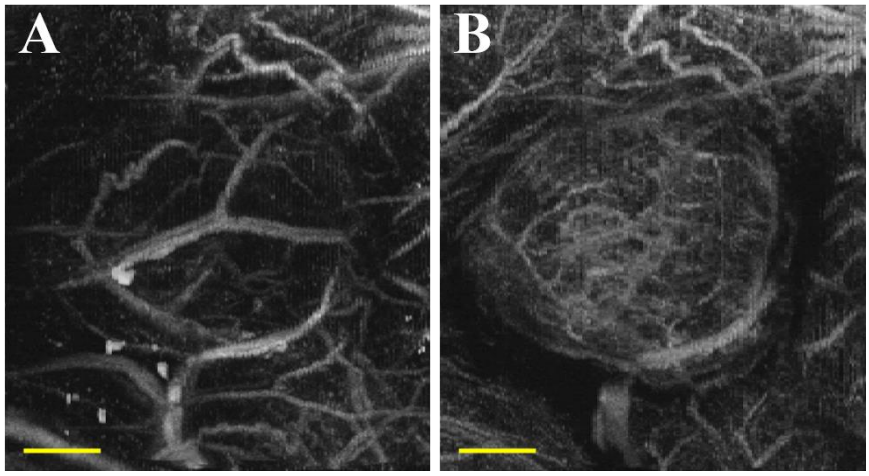

Figure 1.4 Effect of transmit pressure on acoustic angiography images: Acoustic angiography maximum intensity projections of a rat fibrosarcoma tumor at **A)** 1200 kPa and **B)** 560 kPa peak negative pressure. Scale bar = 4 mm.

1.3.2 Preclinical Applications of Acoustic Angiography

As mentioned previously, vascular morphology is altered in the presence of malignant tumors, resulting in highly tortuous vessels. Measures of tortuosity, such as the sum-of-angles metric and the distance metric (32), can be used to quantify the morphology of the microvasculature. Before this quantitative analysis, vessels must first be segmented from the image volume (33).

Morphological analysis has been performed in various small animal cancer models with acoustic angiography. Gessner *et al.* (34) collected acoustic angiography images from healthy and tumor-bearing tissue in a subcutaneous rat fibrosarcoma model and found significantly higher

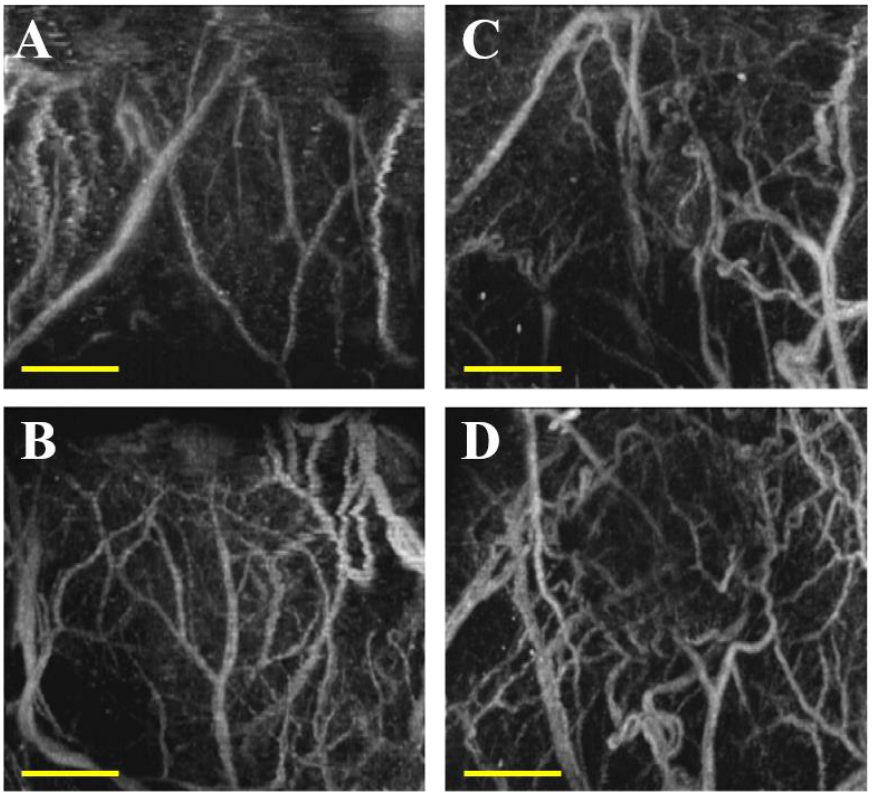

Figure 1.5 Acoustic angiography maximum intensity projections showing microvasculature in healthy or tumor-bearing tissue: Tumor vasculature **(C–D)** is significantly more tortuous and disorganized than healthy vasculature **(A–B)** in a subcutaneous rat fibrosarcoma model. Scale bar = 5 mm.

tortuosity in tumor-bearing compared to healthy tissue, suggesting that this form of quantitative analysis may be able to differentiate tumors from normal tissue (**Figure 1.5**). Shelton *et al.* (35) went on to use acoustic angiography to monitor angiogenesis throughout tumor development in a spontaneous murine model of breast cancer. In this work, the authors showed that tumor microvasculature is significantly more tortuous than that of healthy tissue, even early in development, when tumors are as small as 2 mm (35). In a following study, through analysis of B-mode images, which reflect tissue anatomy, as well as microvascular acoustic angiography images, Rao *et al.* (36) examined the location of tortuous vessels feeding solid tumors and observed that cancer-associated angiogenesis extended beyond what is typically considered the boundaries of solid tumors. Shelton *et al.* (37) then showed that tumors on the order of 5 mm in diameter could

be detected with high specificity and sensitivity through both qualitative and quantitative analysis of acoustic angiography images in a murine model of breast cancer. Altogether, these studies demonstrated that acoustic angiography, followed by visual assessment, microvascular segmentation, and morphological analysis, can provide insight into vascular biomarkers of tumor growth and progression, and that this technique has the potential to improve diagnostic accuracy in clinical cancer care.

Besides evaluating tumor angiogenesis, acoustic angiography has been applied for various purposes in other preclinical models, including observing tumor response to therapy (38–41), assessing molecular expression in tumors (42,43), monitoring vascular formation in new animal models (44,45), and validating novel imaging techniques (46,47). This plethora of previous work demonstrates the versatility of acoustic angiography as a non-invasive microvascular imaging tool in preclinical research.

1.3.3 Acoustic Angiography in the Clinic

Recently, the first human acoustic angiography data was published by Shelton *et al.* (48). The authors showed that acoustic angiography with DF wobbler transducers was able to resolve vessels as small as 200 μm in human breast (48). However, this pilot study also elucidated several limitations of the current acoustic angiography technology. Imaging depth was significantly limited by the fixed focus, shallow field of view, and high receive frequency of the prototype DF wobbler used in the study, such that only lesions within 1.5 cm of the skin surface could be imaged (48). Severe artifact was introduced by respiration motion due to the relatively slow data acquisition required for the mechanical steering of the transducer elements (48). In addition, clinical images exhibited reduced sensitivity (*i.e.*, CTR) compared to preclinical acoustic angiography images due to restrictions in the MCA dose allowed in clinical patients (48). Overall,

this study served to emphasize both the feasibility of acoustic angiography and its current limitations for clinical use.

1.4 Dissertation Scope

While it has been amply demonstrated that acoustic angiography is an excellent tool for microvascular imaging in preclinical small animal models, it is clear that this technique must be specifically optimized for imaging in humans to achieve the goal of clinical translation. Therefore, the objective of this dissertation is to identify methods to improve acoustic angiography for clinical applications. Because the sensitivity of acoustic angiography is inherently dependent on the behavior of MCAs, Chapter 2 explores how superharmonic signal production is affected by microbubble parameters *in vitro*, which may be used to inform the selection of MCAs in the clinic. Chapters 3 and 4 focus on the implementation of the next-generation dual-frequency transducer, a novel stacked dual-frequency array (DFA). Chapter 3 provides a characterization of this transducer both *in vitro* and *in vivo* in a small animal model, while Chapter 4 presents the first in-human data collected with the DFA and addresses the challenges that are yet to be overcome for clinical acoustic angiography. Finally, in Chapter 5, custom simulations are developed to evaluate *in silico* CTR in superharmonic imaging as a function of acoustic parameters. These simulations will be used as a tool to identify optimal parameters for performing acoustic angiography at clinically relevant depths and aid in the design of future dual-frequency transducers.

1.5 Alternative Angiographic Ultrasound Methods

While this dissertation focuses on acoustic angiography, it would be remiss not to discuss alternative methods for imaging microvasculature with ultrasound. The following paragraphs briefly delve into a few such techniques, but it should be noted that more comprehensive reviews have been published elsewhere (49–52).

1.5.1 Doppler-Based Techniques

While conventional Doppler-based ultrasound techniques, such as color Doppler or power Doppler, can suffer from poor spatial or temporal resolution, they are a critical component of clinical care in the diagnosis and monitoring of cancer and cardiovascular disease (12). These aptly named methods rely on the Doppler effect to visualize blood vessels by estimating the velocity and direction of blood flow (9). Recent advances in acquisition and processing have led to the development of new Doppler-based modalities. One example is superb microvascular imaging, a commercially available, state-of-the-art Doppler mode that relies on improved tissue clutter rejection (52). This imaging mode has been used for evaluation of breast lesions (53,54), liver masses (55), lymph nodes (56), and even brain surgery (57).

With the availability of high-frame-rate ultrasound technology, ultrafast Doppler imaging (12) has emerged as a promising technique for visualization of small blood vessels, particularly in the brain. This technique can reach resolutions on the order of 100 μm and can even provide functional information (58,59). Others have implemented novel beamforming techniques as a different approach to improve Doppler sensitivity; for example, acoustic sub-aperture processing can improve signal-to-noise ratio by 10 dB over traditional power Doppler and exhibits high sensitivity and resolution *in vivo* (60,61). Overall, these Doppler-based methods can provide qualitative or quantitative information about vascular structures without administration of contrast. However, Doppler methods typically require repeated acoustic interrogation of the same imaging plane, which can significantly increase acquisition time.

1.5.2 Photoacoustic Imaging

Photoacoustic imaging methods rely on the photoacoustic effect, a physical phenomenon in which an object produces acoustic waves due to irradiation with optical energy (49). This effect

is exhibited by hemoglobin in the bloodstream, allowing angiographic imaging without the use of exogenous contrast agents (49). Photoacoustic techniques are highly scalable, from photoacoustic microscopy with 5 μm resolution and up to 1 mm penetration depth, to photoacoustic computed tomography with 500 μm resolution and up to 50 mm penetration depth (49,62).

While the utility of these techniques has been demonstrated in a variety of preclinical studies for quantitative vascular analysis (63,64), monitoring tumor treatment (65), and imaging larger fields of view at optical resolutions (66), photoacoustic-based angiography has also been applied clinically. Many studies focused on breast imaging, showing that photoacoustic tomography can be used to image breast vasculature up to 50 mm in depth (67,68) and that breast tumor characteristics can be detected with photoacoustic imaging (69–71). Others have applied photoacoustic methods for imaging peripheral vasculature in the limbs (72,73) and skin (74,75). The greatest limitation of these powerful photoacoustic methods is the need for laser components that can quickly become complex and expensive to utilize.

1.5.3 Super-Resolution Ultrasound

Super-resolution ultrasound techniques have recently rose to the forefront of ultrasound research. Ultrasound localization microscopy (ULM) is a super-resolution technique inspired by advances in optical imaging that forms images by localizing individual microbubbles over thousands of consecutive frames to populate the vascular tree (51). ULM images are typically created with a procedure that involves the following steps: 1) collecting thousands of contrast-enhanced frames, 2) spatiotemporal filtering to enhance microbubbles over background tissue, and 3) localizing individual microbubbles on a high-resolution grid (51). Since the introduction of ULM, this general protocol has been adapted by countless groups to optimize different aspects of the novel technique.

Early ULM studies demonstrated the great potential of this technique for imaging and quantitative velocimetry with resolution on the order of 10 μm (76,77). Many groups went on to use ULM for imaging different disease states, including preclinical applications in tumors (78,79), lymph nodes (80), and skeletal muscle (81). Others focused on optimizing different steps in the ULM pipeline, including imaging parameters (82), microbubble composition (83,84), and microbubble detection (85). To address limitations of spatiotemporal filtering, nonlinear imaging techniques have been applied for bubble detection prior to ULM processing (85,86); Kierski *et al.* (86) described a novel combination of dual-frequency imaging and ULM. Studies using phase-change contrast agents, rather than microbubbles, have also been published (87–89).

The abundance of recent literature on ULM highlights the extraordinary abilities of this technique – namely, the ability to image vessels at micron-scale resolution with sufficient penetration depth for clinical applications. To improve the power of this method even further, translation of ULM into 3D is actively being pursued (90,91). However, acquiring ULM data requires considerable time to populate the smallest vessels in a region of interest, particularly in slow-flowing vasculature. In addition, the formation of ULM images is quite computationally intensive, requiring significant computational power and time. Nevertheless, it has been shown that ULM can be performed in human patients with clinically approved imaging and microbubble parameters (92).

CHAPTER 2
SUPERHARMONIC RESPONSE OF MICROBUBBLE CONTRAST AGENTS[2]

2.1 Introduction

Since the first use of microbubbles for ultrasound contrast enhancement (93), microbubble contrast agents (MCAs) have become a common tool in clinical use and preclinical research worldwide. Several contrast agents are now commercially available and routinely used in the clinic. A recent evaluation of the most common clinical agents in the United States found differences in the performance of these agents at clinical doses (94). As the field of contrast-enhanced ultrasound has grown, studies have been published on methods of microbubble synthesis (95,96) and contrast-specific techniques, such as harmonic imaging (97), subharmonic imaging (98,99), pulse-inversion imaging (19,20), and combinations of these methods. Applications of these contrast-specific techniques include perfusion imaging (100–102) and molecular imaging (103–106).

As described in the previous chapter, superharmonic imaging is an extension of harmonic imaging that has been developed to take advantage of the broadband frequency response of microbubbles, with the goal of achieving signal separation between the excitation signal and scattered bubble responses (21,22,27). One such method optimally uses dual-frequency devices

[2]This chapter previously appeared in an article in Ultrasound in Medicine and Biology. The original citation is as follows: Newsome IG, Kierski TM, Dayton PA. "Assessment of the Superharmonic Response of Microbubble Contrast Agents for Acoustic Angiography as a Function of Microbubble Parameters," *Ultrasound Med. Biol.* 2019;45(9):2515-2524. doi: 10.1016/j.ultrasmedbio.2019.04.027.

to excite microbubble contrast at a low frequency (2 – 4 MHz) and receive the superharmonic response at a much higher frequency (25 – 30 MHz) (27). By doing so, the acoustic signals of microbubbles are isolated from the signals of tissue, creating detailed, high-resolution maps of the microvasculature (27). Applications of this approach in 3D enable "acoustic angiography," which provides volumetric imaging of microvascular patterns akin to computed tomography angiography, yet with contrast ultrasound (34). Previous work has focused on optimizing microbubble response for this technique, examining contrast-to-tissue ratio as a function of peak negative pressure for varying transmit frequencies, contrast concentrations, and microbubble diameters (29). A similar study investigated the generation of superharmonic energy from microbubbles, finding that shell fragmentation creates the strongest superharmonic signals (31).

To date, clinical implementation of acoustic angiography has demonstrated that increased signal-to-noise ratio would improve the utility of this technique in humans, where contrast dose is regulated (48). One means to achieve a superharmonic signal increase might be to use optimally-sized microbubble contrast agents, as it is well known that the microbubble diameter can influence scattered signal intensity (103,107–110). We also note that the composition of the encapsulating shell and gas core of microbubbles may affect echogenicity. Previous studies have suggested increased microbubble stability (111) and nonlinear response (112) with increasing acyl (carbon) chain length of the main phospholipid in the encapsulating shell. However, to date, a comprehensive study of the superharmonic signal produced as a function of microbubble parameters has not been performed. Thus, the purpose of this study is to evaluate differences in superharmonic signal production across various compositions and sizes of MCAs under conditions of varying acoustic pressure, with the goal of establishing which MCA might provide the best performance for acoustic angiography and similar applications in the clinic.

2.2 Materials and Methods

2.2.1 Contrast Agent Preparation

The MCAs tested in this work are summarized in **Table 2.1**. In-house microbubble contrast was formulated as described previously (35). Briefly, dried lipids were dissolved in a mixture of phosphate buffered saline (PBS), propylene glycol, and glycerol at the molar ratios and volume percentages described in **Table 2.2**. The lipid solution was then aliquoted into vials, the headspace in each vial was exchanged with the selected gas, and each vial was shaken with a mechanical agitator (Vialmix, Lantheus Medical Imaging, North Billerica, MA, USA) to form polydisperse, lipid-shelled microbubbles. Several commercially available contrast agents were used in addition to those formulated in-house: Optison (GE Healthcare, Inc., Marlborough, MA, USA), Definity (Lantheus Medical Imaging, Inc., North Billerica, MA, USA), Micromarker (FUJIFILM VisualSonics, Inc., Toronto, ON, Canada), and a variety of preclinical size-isolated microbubbles (SIMBs, Advanced Microbubbles Laboratories, Boulder, CO, USA). Clinical agents were prepared according to manufacturer-provided instructions (113,114).

The fourteen contrast agents were separated into four groups for comparison: 1) gas core, 2) lipid shell, 3) clinical and preclinical, and 4) bubble diameter. **Table 2.1** lists the contrast agents chosen for each group. Although SIMBs are a preclinical agent, in this work, they were used specifically for examining the effect of microbubble diameter and were not compared in the clinical and preclinical group. To examine the effect of lipid composition, four lipid formulations were tested with varying carbon chain lengths: 1) C16-2L and 2) C16-3L, both with 16 carbons in their acyl chains; 3) C18-2L, which has an 18-carbon acyl chain; and 4) C20-2L, aptly named for its 20-carbon chain. More detail on these formulations can be found in **Table 2.2**. Microbubbles with the same shell (the in-house lipid formulation referred to as C18-2L) and either

Table 2.1: Summary of contrast agents.

Group	Name	Shell	Core	Distribution	Manufacturer
Clinical and Preclinical	Definity	lipid	C_3F_8	polydisperse	Lantheus Medical Imaging
	Optison	protein	C_3F_8	polydisperse	GE Healthcare
	Micromarker	lipid	N_2 and C_4F_{10}	polydisperse	FUJIFILM VisualSonics
Gas Core	DFB	lipid	C_4F_{10}	polydisperse	Dayton Lab
	OFP	lipid	C_3F_8	polydisperse	Dayton Lab
	SF_6	lipid	SF_6	polydisperse	Dayton Lab
Lipid Shell	C16-2L	lipid	C_3F_8	polydisperse	Dayton Lab
	C20-2L	lipid	C_3F_8	polydisperse	Dayton Lab
	C16-3L	lipid	C_3F_8	polydisperse	Dayton Lab
	C18-2L	lipid	C_3F_8	polydisperse	Dayton Lab
Bubble Diameter	SIMB1-2	lipid	C_4F_{10}	size-sorted	Advanced Microbubbles Laboratories
	SIMB3-4	lipid	C_4F_{10}	size-sorted	Advanced Microbubbles Laboratories
	SIMB4-5	lipid	C_4F_{10}	size-sorted	Advanced Microbubbles Laboratories
	SIMB5-8	lipid	C_4F_{10}	size-sorted	Advanced Microbubbles Laboratories

Table 2.2: In-house lipid formulations.

Name	Acyl Chain Length	Number of Lipids	Lipid Composition	Molar Ratio	Propylene Glycol	Glycerol
C16-2L	16	2	DPPC:DPPE-PEG2000	9:1	15%	5%
C20-2L	20	2	DAPC:DSPE-PEG2000	9:1	15%	5%
C16-3L	16	3	DPPC:DPPA:DPPE-PEG5000	8.2:1:0.5	10%	10%
C18-2L	18	2	DSPC:DSPE-PEG2000	9:1	15%	5%

Abbreviations:
DPPC = dipalmitoylphosphatidyl-choline
DPPE = dipalmitoylphosphatidyl-ethanolamine
DPPA = dipalmitoyl-phosphate
DSPC = distearoylphosphatidyl-choline
DSPE = distearoylphosphatidyl-ethanolamine
DAPC = diarachidonoylphosphatidyl-choline
PEG = polyethylene glycol

octafluoropropane (C_3F_8 or "OFP"), decafluorobutane (C_4F_{10} or "DFB"), or sulfur hexafluoride (SF_6) as the gas core were compared to evaluate the effect of gas core composition. The concentration and size distribution of all contrast agents were measured with a single particle optical sizing device (0.5 – 400 μm measurable range, Accusizer 780A, Particle Sizing Systems, Santa Barbara, CA, USA). In this work, we have focused on quantifying superharmonic production from a population of bubbles, where the size of the population (*i.e.*, #/mL) is a constant variable

across all measurements. As such, all concentration and size measurements presented are number- rather than volume-matched. After concentration analysis of the stock solution, all microbubbles were diluted in PBS to a target concentration of 10^8 #/mL, and the final concentration was tested again before data collection. For preclinical acoustic angiography, 10^8 #/mL is a typical dose and was therefore chosen as the target concentration for comparison in this work (35,36,43,115).

2.2.2 Ultrasound Parameters and Setup

For this work, a prototype dual-frequency transducer (modified RMV 710, FUJIFILM VisualSonics, Inc., Toronto, ON, Canada) with two confocally aligned single elements was used (26). At a pulse repetition frequency (PRF) of 20 Hz, a single cycle cosine-windowed sine wave at 4 MHz was transmitted with the low-frequency element of this transducer, which has been described in detail previously (30). The high-frequency element received at 25 MHz, and both elements had a focal depth of 16 mm. The resulting transmit and receive beamwidths were approximately 474 μm and 142 μm, respectively. The peak negative pressure of the transmit waveform was varied from 400 to 2400 kPa, corresponding to a mechanical index (MI) range of 0.2 to 1.2. This MI range was chosen to cover acoustic pressures that have previously been explored for superharmonic imaging. Previous studies have demonstrated that acoustic pressures that typically result in microbubble fragmentation generate the greatest superharmonic content, although lower pressures that do not result in immediate bubble fragmentation can also produce weaker superharmonic signals (29). A cellulose tube with 200 μm inner diameter was placed at the focal depth of the transducer and aligned perpendicular to the direction of acoustic propagation in a water bath maintained at 37°C (±1°C). The contrast agent of interest was infused through the tube at a rate of 15.9 mm/s using an infusion pump (Pump 11 Elite, Harvard Apparatus, Holliston, MA, USA). With this flow rate, a PRF of 20 Hz, and the beamwidths given above, fresh contrast

was insonified with each transmission. Between different trials and contrast agents, the tube was flushed with distilled water until no bubble signal remained.

2.2.3 Data Acquisition and Analysis

To collect raw radiofrequency (RF) data, a custom circuit was built to allow connection of the modified RMV probe to a broadband receive amplifier (Ritec, Inc., Warwick, RI, USA), removing the need for a Vevo770 preclinical ultrasound scanner (FUJIFILM VisualSonics, Inc., Toronto, ON, Canada). Collecting data through a simple receive amplifier was preferable for this work because it allowed greater control over experimental parameters, such as PRF, and removed possible unknown data transformations that could be performed in the scanner. The experimental setup used is depicted in **Figure 2.1**. After amplification, the RF data was sampled at 200 MS/s and digitized with a 12-bit digitizer board (CSE1222, DynamicSignals LLC, Lockport, IL, USA) before collection with a custom LabVIEW program (National Instruments Corporation, Austin, TX, USA). For all contrast agents, twelve trials were performed. The twelve trials were split equally among four vials of each contrast agent, with an exception for SIMB1-2, for which only

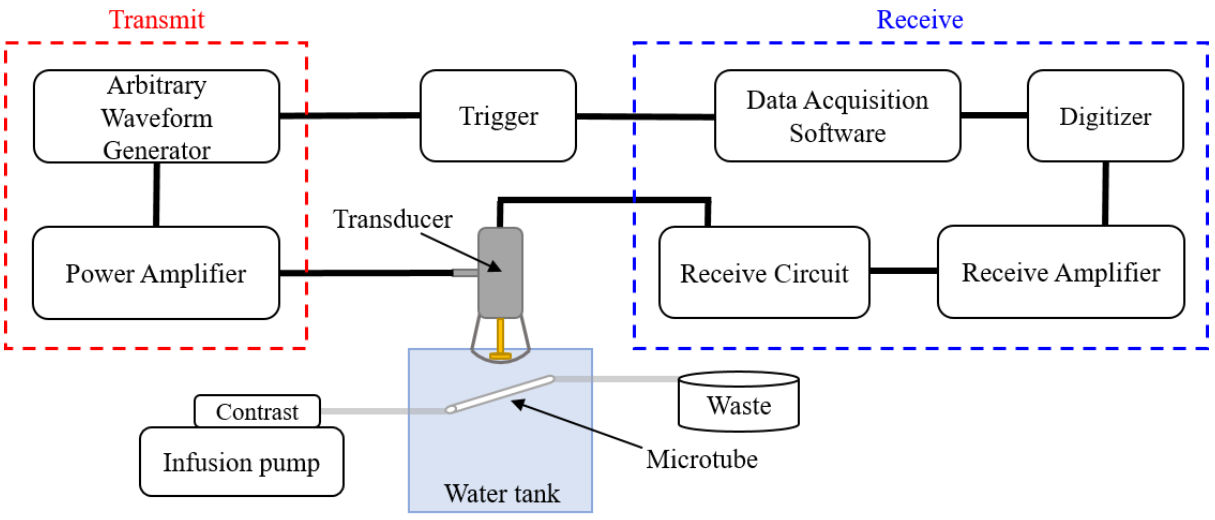

Figure 2.1 Schematic diagram illustrating the experimental setup used for *in vitro* microbubble contrast agent characterization.

three vials of contrast agent were available. For each trial, a fresh dilution was prepared, the concentration was measured, and 200 lines of RF data were saved for analysis at each pressure. As reference, RF data was also saved at each pressure while the tube was infused with water.

To account for the frequency response of the transducer used for data collection, a proxy for the frequency response of the receive element was measured via pulse-echo test on a linear reflector. A steel ball with a diameter of 6.35 mm (44x larger than the beamwidth of the receive element) was placed at the focus of the transducer to be used as a linearly reflecting target, and a single-cycle 30 MHz pulse was transmitted. The received pulse-echo RF data was sampled, digitized, and recorded as mentioned above. The frequency spectrum was taken as the magnitude of the Fourier transform of the RF data, and the receive frequency response was obtained by taking the square root of the pulse-echo spectrum. The receive bandwidth measured in this way does not provide a full electromechanical and acoustical frequency response, but it is representative of the frequency behavior of the transducer. The measured receive response is depicted in **Figure 2.2**.

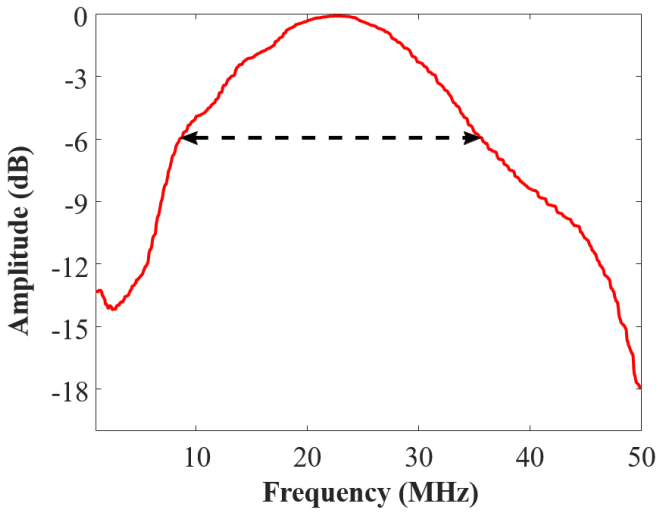

Figure 2.2 Frequency response of the receive element: Receive bandwidth measured from 0 – 50 MHz (red) and the –6 dB bandwidth with cutoffs at 8.5 and 35.7 MHz (black dashed arrow).

All analysis was performed in MATLAB (Mathworks, Inc., Natick, MA, USA). For each line of RF data, the linear frequency spectrum was obtained by taking the magnitude component of the fast Fourier transform. To remove any signal from the tube walls, the average spectrum from water was subtracted from each contrast spectrum. The resulting spectrum was then normalized by the frequency response of the receive element. Superharmonic response was quantified as the area under the curve (AUC) of the normalized, water-subtracted frequency spectrum of the collected data inside the -6 dB bandwidth of the receive element, indicated by the arrow in **Figure 2.2** (8.5 MHz to 35.7 MHz). The AUC metric was calculated by the trapezoidal method and averaged over the 200 lines collected for each agent and pressure. The mean AUC from each trial was then averaged over all trials for the final superharmonic metric, which is presented as mean ± standard error.

2.3 Results and Discussion

The mean diameter and concentration of each sample of contrast agent as measured after dilution for concentration-matching are provided in **Figure 2.3**. The mean diameter of each contrast agent is shown in **Figure 2.3** (A, C, E, G). The target concentration was 10^8 #/mL. To ensure that each dilution was adequately matched to the target concentration, we characterized the variability of our complete experimental setup. Preliminary data (unpublished) found that a 2.3x increase in concentration led to only a 5% increase in superharmonic AUC, while two independent dilutions of the same concentration produced superharmonic AUCs differing by 7%. This data demonstrates that up to twofold changes in concentration result in AUC values within the variability of this experimental measurement. The source of this experimental variability may be a combination of variations in the mixing of individual dilutions, small temperature fluctuations in the water bath and surrounding laboratory, and variations in concentration measurement on the

sizing device used here, among others. As such, the spread of concentrations displayed in **Figure 2.3** (B, D, F, H) was deemed acceptable for this work.

First, the effect of microbubble gas core composition on superharmonic energy production was evaluated. The three gases used here (OFP, DFB, and SF_6) are commonly used in the current generation of ultrasound contrast agents, as their high molecular weights improve stability in circulation *in vivo* (116,117). Our results, as shown in **Figure 2.4A**, indicated greater superharmonic production from either perfluorocarbon-filled agent compared to the SF_6-filled bubbles for MI ≥ 0.6. OFP and DFB bubbles produced superharmonic AUCs of 53.68 ± 4.276 and 46.43 ± 3.805, respectively, at MI = 1.2, while that produced by SF_6 bubbles was 28.56 ± 1.769. SF_6 microbubbles have been shown to exhibit increased resistance to pressure changes, such as those experienced in cardiac flow (118). Due to this increased resistance, a clinically used SF_6-filled MCA has been shown to exhibit longer circulation time compared to Definity and Optison

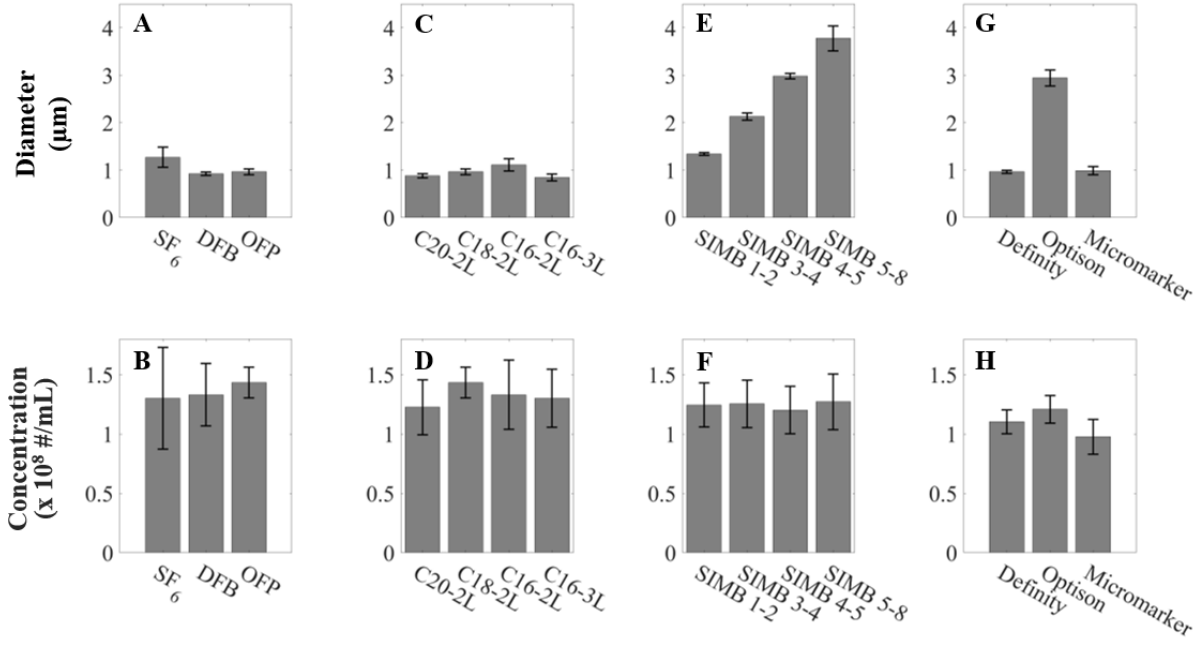

Figure 2.3 Size and concentration measurements for the contrast agents in each group: gas core **(A–B)**, lipid shell **(C–D)**, bubble diameter **(E–F)**, and clinical and preclinical **(G–H)**. Data are presented as mean ± standard deviation for n = 12 trials per contrast agent.

(94). The diffusivity and solubility properties of the gas core may have an effect on certain acoustic responses, in addition to microbubble stability; one study reported that bubbles filled with gases with higher diffusion coefficients, such as SF_6, exhibited less delayed subharmonic emissions compared to perfluorocarbon-filled bubbles (119). As such, it is fathomable that other acoustic responses, such as superharmonic production, could also be influenced by properties of the gas core. In addition, the SF_6-filled microbubbles prepared here had a slightly larger mean diameter (1.23 µm) than either OFP-filled (1.00 µm) or DFB-filled (0.92 µm) bubbles, though all three contrast agents were prepared under the same conditions. Due to the inverse relationship between

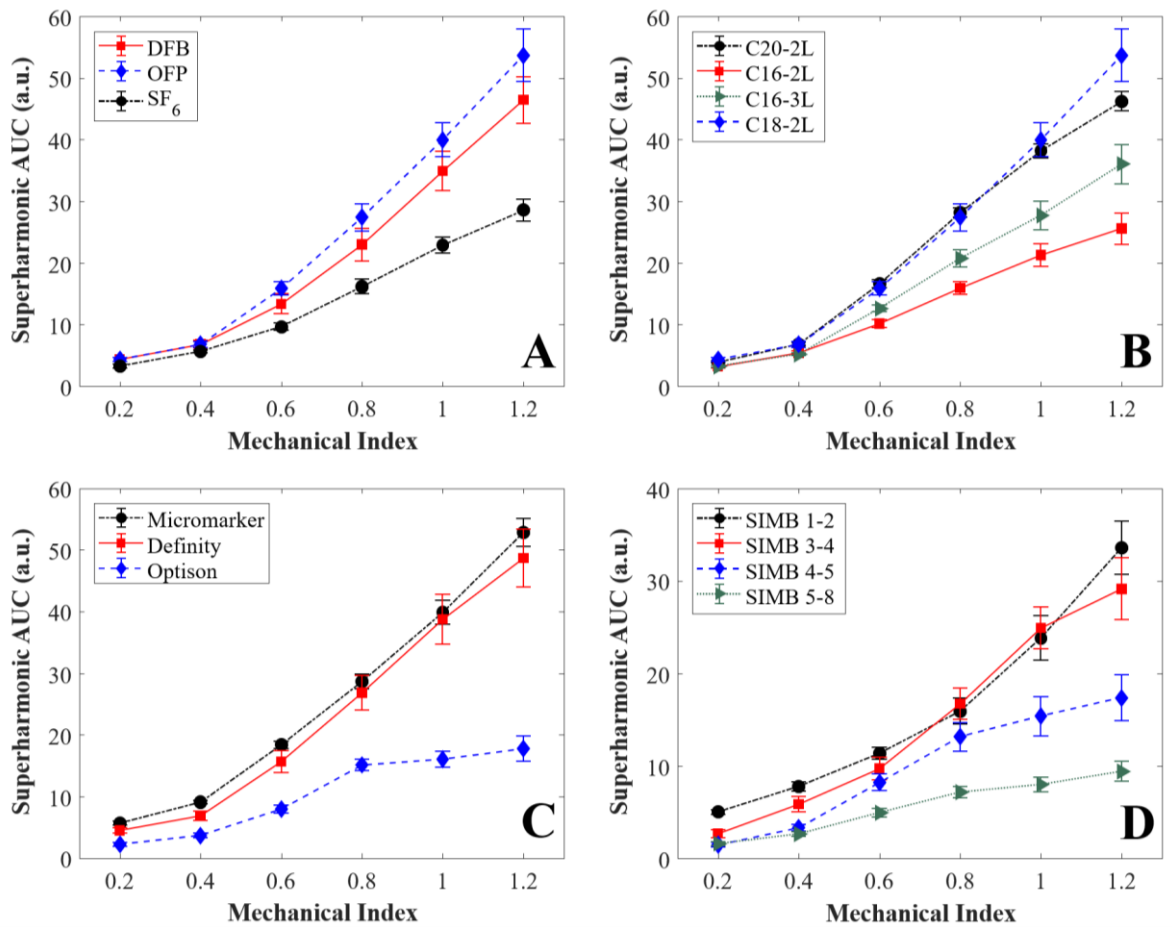

Figure 2.4 Comparison of superharmonic production for different contrast agents: **A)** contrast agents with different gas cores, **B)** contrast agents with different lipid shell compositions, **C)** clinical and preclinical contrast agents, and **D)** contrast agents with different bubble diameters. Data are presented as mean ± standard error for n = 12 trials per contrast agent. AUC = area under the curve, OFP = octafluoropropane, DFB = decafluorobutane, SF_6 = sulfur hexafluoride.

bubble diameter and resonance frequency (108,117), this could have an effect on the resulting acoustic response.

MCAs with different lipid shell compositions were also compared. The results for this group are shown in **Figure 2.4B**. Here, we observed greater superharmonic production from the contrast agents with longer acyl chains, C18-2L and C20-2L. At MI = 1.2, C18-2L produced the most superharmonic energy with an AUC of 53.68 ± 4.276, followed by C20-2L with 46.20 ± 1.565, C16-3L with 36.04 ± 3.182, and C16-2L with 25.55 ± 2.524. These results agree with those of van Rooij *et al.* (112), who reported higher second harmonic responses for bubbles with 18-carbon chains compared to 16-carbon chains. Others have evaluated microbubble stability as a function of acyl chain length and found that as chain length increased from 16 to 22 carbon atoms, stability also increased (111). However, the differences in stability observed by Garg *et al.* (111) in diluted microbubbles were insignificant at short time scales (*i.e.*, less than 20 minutes in dilution). For the current study, each trial was performed in five minutes or less from time of dilution to completion of data acquisition. As such, any effects of stability should be negligible in the current results.

The clinical and preclinical contrast agents compared in this work were Definity, Optison, and Micromarker (**Table 2.1**). Definity and Optison are both approved for clinical use in the United States, while Micromarker is solely a preclinical agent. While Definity and Micromarker have phospholipid shells, Optison is protein-shelled (113,114,120). To reach 10^8 #/mL, Definity required a 0.68% dilution from the measured stock concentration of 1.51 x 10^{10} #/mL, while Optison required a 23.8% dilution from the measured stock concentration of 4.21 x 10^8 #/mL. These values may be of interest to others who use these commercially available, clinical MCAs. The results of the comparison of this group are shown in **Figure 2.4C**. The superharmonic response

of Optison behaved asymptotically above MI = 0.8, while Micromarker and Definity increased relatively linearly throughout the MI range tested. At MI = 1.2, the maximum MI used here, the superharmonic AUC of Optison was 17.79 ± 2.013, nearly three times less than that of Definity (48.67 ± 4.712) or Micromarker (52.84 ± 2.285). At a more intermediate MI = 0.6, Optison produced an AUC of 7.96 ± 0.661, only half that of Definity (15.67 ± 1.75) or Micromarker (18.42 ± 0.584). Similar trends have been observed between Optison and Definity in another comparative study of clinical ultrasound contrast agents (94).

The relatively poor performance of Optison compared to these other agents is likely due to two factors: 1) its albumin shell and 2) larger size distribution. Albumin-shelled microbubbles have been found to be more susceptible to static diffusion and less susceptible to shell fragmentation at acoustic pressures below 800 kPa compared to phospholipid-shelled microbubbles (121). This could have negative implications for superharmonic imaging with albumin-shelled bubbles based on previous work, which demonstrated that superharmonic signals are preferentially generated by microbubbles undergoing substantial oscillations and that these signals are largest when these oscillations lead to fragmentation (31). Furthermore, in this work, Optison had a measured mean diameter of 2.94 μm, compared to 0.96 μm for Definity and 0.99 μm for Micromarker (**Figure 2.3G**). The effect of microbubble diameter on superharmonic signal production will be discussed in the following paragraphs.

Size-isolated microbubbles (SIMBs, Advanced Microbubbles Laboratories, LLC, Boulder, CO, USA) were used to compare the superharmonic response of MCAs with the same shell and gas properties but different diameters (**Table 2.1**). The diameters tested ranged from 1.34 μm to 3.78 μm (**Figure 2.3E**). Results for this group are shown in **Figure 2.4D**. Superharmonic AUC generally decreased as bubble diameter increased, with the smaller SIMBs performing similarly

and producing greater superharmonic signal than the larger SIMBs. For example, at MI = 1.2, AUC values of 33.59 ± 2.881, 29.14 ± 3.331, 17.36 ± 2.455, and 9.40 ± 1.061 were obtained for SIMB 1-2, 3-4, 4-5, and 5-8, respectively. As MI increased, the difference in superharmonic production between the groups (particularly SIMB 1-2 and 3-4 *versus* SIMB 4-5 and 5-8) became more exaggerated. As previously discussed, bubble diameter is inversely related to resonance frequency, which likely contributes to the differences in superharmonic AUC observed among these groups. As bubble diameter increased, resonance frequency decreased, moving the excitation frequency further from resonance. Kaya *et al.* (108) performed a comprehensive study on the acoustic responses of monodisperse microbubbles with different diameters and demonstrated the importance of coupling excitation frequency to microbubble resonance. This study demonstrated via simulation and experiment that larger bubbles (6 – 8 μm diameter) resonate and produce their largest response around 1 MHz, while smaller bubbles (2 – 4 μm diameter) produce greater responses near resonance between 3 – 6 MHz (108).

Previous work by our group has elucidated the origins of superharmonic signal production (31). The authors determined that the strongest superharmonic signals are produced by oscillations resulting in microbubble shell fragmentation, and that such fragmentation occurs preferentially for smaller bubbles (1 μm) on the initial pulse, while larger bubbles (4 μm) are prone to shrinking, which persists over several pulses and produces weaker superharmonic signals (31). Moreover, for stationary bubbles, 1 μm bubbles initially produced greater superharmonic intensity, which decayed quickly to a lower value than that produced by 4 μm bubbles (31). In the current work, all data was acquired while contrast was flowing, so signal decay was not observed, and smaller bubbles consistently produced greater superharmonic signals than larger bubbles.

However, other studies have suggested increases in scattered signal when using larger bubbles (83,103,107,109), due to the dependence of scattering cross section on microbubble radius (122). For example, Streeter *et al.* (123) showed increased molecular targeting signal using 3 μm bubbles over 1 μm bubbles with a 7 MHz harmonic imaging scheme, while Sirsi and colleagues (107) used 6 – 8 μm bubbles to enhance fundamental imaging at 40 MHz. It is obvious that there are many interconnected factors influencing the results of these previous works and the current study, including microbubble composition, size, the frequencies at which bubbles are excited, and the bandwidth at which bubble echoes are received. Future work is needed to continue illuminating these relationships, as the current study is limited to the specific 4 MHz excitation case with a receive bandwidth between 8.5 – 35.7 MHz.

While all contrast agents were tested at a matched concentration in this work, clinical MCAs are not necessarily used at the same concentration or dose in humans. For example, the stock concentration and the clinically recommended doses for Definity and Optison are different. The recommended doses for one bolus of Definity and Optison are 10 μL/kg (114) and 0.5 mL (113), respectively. Assuming an average male patient as described by the US Center for Disease Control and Prevention (124) and using Nadler's formula to calculate blood volume (125), we can estimate a typical clinical concentration for these MCAs. Consider a fictional patient who weighs 88.7 kg and has a blood volume of 5.46 L. Assuming a stock concentration of 1.2×10^{10} #/mL (114), the overall concentration of Definity in circulation after one bolus at the recommended dose would be 1.9×10^{6} #/mL. In the same patient, one bolus of Optison at a stock concentration of 8.0×10^{8} #/mL (113) would result in an overall concentration of 7.3×10^{4} #/mL – two orders of magnitude lower than that of Definity. If the results observed for these two clinical agents in the present study can be extrapolated to lower concentrations, this difference in dose could be

discouraging for clinical superharmonic imaging with Optison. However, concentration is known to play a significant role in microbubble behavior under acoustic stimulation, as discussed in the following section.

2.4 Limitations

A main limitation of the present study is the relatively high concentration used during data collection. While this concentration is relevant for preclinical imaging, it is known that higher microbubble concentrations lead to greater bubble-bubble interactions (126). Specifically, high bubble concentrations result in smaller distances between individual microbubbles in a field, which decrease the overall resonance frequency of the bubble population; this has been shown both theoretically (127–129) and experimentally (130,131). This implies that the results of the present work may not simply extrapolate to lower concentrations, such as those used in the clinic, and further investigation may be necessary to continue improvement of clinical superharmonic contrast imaging.

Another important limitation of this work is the method used for concentration matching. The particle sizing device used here to obtain concentration and size measurements is inherently limited to measure particles between 0.5 and 400 μm (132). As such, the concentration of a polydisperse contrast agent with significant portions of its distribution outside this range will be measured inaccurately by this device. It is unlikely that ultrasound contrast agents contain bubbles larger than 400 μm in diameter, but it is feasible that polydisperse agents with a mean diameter around 1 μm, such as Definity, Micromarker, and our in-house formulations, have populations of bubbles below 0.5 μm in size. If so, the concentrations of these agents would be misrepresented to be lower than they truly are, which could explain the differences, or lack thereof, in superharmonic signal generation we have observed in these agents. This methodology also affects the mean

diameter of different microbubbles measured in this work. The values reported here may appear lower than those reported in other literature, due to the minimum detection threshold of the Accusizer (0.5 μm), compared to other common methodologies, such as a Coulter counter or optical microscopy sizing. Furthermore, the values reported here are number-weighted rather than volume-weighted. The methodology used in measuring and reporting microbubble size is a major confounding variable that should always be considered in the interpretation of experimental results in which bubble size is reported.

This study focused on the effect of different properties of MCAs on superharmonic signal production. Recently, attention has been brought to the importance of properties of the external environment when assessing the acoustic response of microbubbles. Others have reported decreased microbubble oscillation amplitude (133) and fragmentation (134) in fluids with viscosities similar to blood. Helfield *et al.* (134) also observed a decrease in broadband superharmonic emissions, in keeping with the observation by Lindsey *et al.* (31) that substantial broadband superharmonic signals originate from microbubble fragmentation. Because the current work used a less viscous fluid during data collection, the superharmonic content recorded is likely much greater than would be seen *in vivo*. While the absolute values of the superharmonic metric used here would decrease, we believe the trends shown would remain valid in a blood-like fluid.

Many studies have examined the behavior of microbubbles in capillary-sized tubes. It has been reported that bubbles in 12 – 25 μm inner diameter tubes produce smaller oscillation amplitudes (135,136) and exhibit fewer occurrences of microbubble fragmentation (136) than those in 160 – 200 μm tubes. Furthermore, Sassaroli and Hynynen (137) have shown that the acoustic pressure threshold to cause fragmentation increases as tube size decreases. In consequence, the results presented in this work are dependent on the tube used for data collection.

The *in vitro* results shown here for a 200 μm synthetic vessel may not translate directly *in vivo*, where a distribution of vessel diameters is present.

Finally, we reiterate that the data presented herein is specific to superharmonic imaging within the conditions of the custom fabricated dual-frequency transducer used, which has a frequency bandwidth quite different than current clinical transducers. Hence, observations of microbubble performance observed here should not be assumed to exhibit the same trends for pulse inversion, amplitude modulation, subharmonic imaging, or other techniques performed within the bandwidth of commercial clinical transducers and ultrasound systems. Future work will be necessary to evaluate the performance of different contrast agents within clinical imaging parameters. Similarly, additional work will need to be performed to optimize contrast agents for *in vivo* acoustic angiography.

2.5 Conclusion

In this chapter, we have assessed the superharmonic response of several types of contrast agents specific to superharmonic imaging at 4 MHz. We have found that certain microbubbles produce much more superharmonic energy than others when insonified at 4 MHz. In summary, bubbles with perfluorocarbon cores produce more superharmonic content than those with sulfur hexafluoride cores. Microbubbles with longer acyl chains (18 – 20 carbons) in the lipid shell create more superharmonic energy than bubbles with shorter chains (16 carbons). Superharmonic production generally decreases with increasing size between 1 and 4 μm, presumably due to decreasing resonance frequency or susceptibility to fragmentation. Finally, Definity and Micromarker may be better suited for clinical and preclinical superharmonic imaging, respectively, than Optison when transmitting at 4 MHz. These results will be used to optimize future acoustic angiography studies and improve contrast-to-tissue ratio and sensitivity. In the future, continuation

of this work will include evaluation of these results in animal models *in vivo* to predict the optimal microbubble contrast agent for superharmonic imaging with this dual-frequency system.

CHAPTER 3
CHARACTERIZATION OF A DUAL-FREQUENCY ARRAY FOR ACOUSTIC ANGIOGRAPHY[3]

3.1 Introduction

As discussed in the previous chapters, ultrasound is a widely used modality for soft tissue imaging due to its portability, safety, high temporal resolution, and low cost compared to computed tomography and magnetic resonance imaging. With the addition of microbubble contrast agents (MCAs) as a blood pool marker, ultrasound can also be used to image blood flow and perfusion (138). Contrast-specific imaging schemes, such as pulse inversion (19) and amplitude modulation (20), utilize the nonlinear response of MCAs by receiving at the second harmonic frequency and are commonly used to reduce background tissue signal in contrast-enhanced ultrasound imaging. Subharmonic (98,139) and superharmonic (21,22) techniques are also used to enhance nonlinear microbubble signal over background tissue.

Bouakaz and colleagues (21) first introduced superharmonic imaging, in which ultrasound images are formed from higher harmonic echoes (≥3x the fundamental frequency) rather than the fundamental or second harmonic response. The authors used a custom phased array with interleaved transmit and receive elements, centered at 0.9 and 2.8 MHz, respectively, to show that

[3]This chapter previously appeared in an article in IEEE Transactions on Ultrasonics, Ferroelectrics, and Frequency Control. The original citation is as follows: Newsome IG, Kierski TM, Pang G, Yin J, Yang J, Cherin E, Foster FS, Carnevale C, Démoré CEM, Dayton PA. "Implementation of a novel 288-element dual-frequency array for acoustic angiography: *in vitro* & *in vivo* characterization," *IEEE Trans UFFC.* 2021;in press. doi: 10.1109/TUFFC.2021.3074025.

greater contrast-to-tissue ratio (CTR) can be achieved with superharmonic over second harmonic imaging (21). Kruse and Ferrara (22) extended this concept and demonstrated high resolution superharmonic M-mode imaging using 2.25 MHz transmit and 15 MHz receive with two confocal pistons.

Building on these seminal studies, Gessner and colleagues developed acoustic angiography, a three-dimensional (3D) microvascular ultrasound imaging technique, using custom dual-frequency (DF) wobbler transducers with transmit at 2 – 4 MHz and receive at 30 MHz (26,27). The authors used this DF strategy to isolate intravascular microbubble signals from signals of the surrounding tissue with high sensitivity and resolution (26,27). Implementation of the technique in 3D produces volumetric maps of the microvasculature, which can be quantitatively analyzed for characteristics of vessel morphology, coining the term “acoustic angiography” (26,27). Quantitative analysis of tortuosity and vascular density on acoustic angiography images has been used to differentiate tumors from healthy tissue (34–36), monitor response to therapy (38–41), and assess vascular development (44,45) in various preclinical models.

However, previous acoustic angiography studies were necessarily focused on the preclinical development of the technique. The DF wobblers were designed specifically for small animal imaging in rodents, with shallow focal depth and depth of penetration limited by the high receive frequency (27). While preclinical use of acoustic angiography has proven highly useful for tumor differentiation and monitoring treatment, the first clinical application of acoustic angiography in human breast found the technique lacking in several aspects. Most notably, the limited imaging depth excluded many patients from the study, the sensitivity of the transducer was limited at a clinical MCA dose, and respiratory motion significantly degraded image quality during

data acquisition (48). For the progression of this microvascular imaging technique toward clinical translation, improvements in DF transducer technology are required to overcome these issues.

Most clinical ultrasound imaging is performed with array transducers, which have been called "the most important advance in transducer technology" for the benefits they provide in terms of beam focusing, steering, and rapid acquisition sequences (11). For dual-frequency imaging and therapeutic applications, including acoustic angiography, it follows that the next generation of transducers must be DF arrays (140). In this chapter, we present the latest developments in acoustic angiography through the implementation of a coaxially stacked DF array (DFA) transducer, which has been developed by our group and collaborators (141). We begin by characterizing this new acoustic angiography system *in vitro* and go on to demonstrate its *in vivo* imaging capabilities.

3.2 Materials and Methods

3.2.1 Ultrasound System Description

Figure 3.1 provides a schematic of the acoustic system used in this work. The transducer used here was a vertically stacked DF array, as described in (141). It consisted of a 32-element low-frequency (LF) linear array stacked behind a 256-element high-frequency (HF) linear array for LF transmit and HF receive. The nominal center frequencies of the LF and HF stacks are 2 MHz and 18 MHz, respectively. The design of this DFA allows for confocal imaging through electronic focusing in the lateral (azimuthal) and axial directions. The DFA is operated by two programmable ultrasound machines that share a system clock for phase-accurate synchronization during imaging (Vantage 256, Vantage 256 high-frequency configuration, and Multi-System Synchronization Module, Verasonics, Kirkland, WA, USA). The system is programmed for focused line-by-line imaging with 128 ray lines with 2 MHz transmit on the LF array and receive with 62.5 MHz sampling rate and a 10 – 30 MHz bandpass filter on the HF array. Hereafter, this

form of imaging will be referred to as “dual-frequency mode” or “DF-mode.” Conventional high-frequency tissue imaging (transmit and receive at 15.625 MHz) will be referred to as “B-mode.”

For imaging in DF-mode, the transmit aperture consisted of all 32 elements of the LF array, and all 256 elements of the HF array were used on receive. For all transmissions, the full LF aperture was excited with a single-cycle pulse with a frequency of 2 MHz. Each DF-mode frame consisted of 128 ray lines with their origins located at the center of every other HF element. Data were beamformed with dynamic receive beamforming on the native Verasonics beamformer after tuning to account for the unique geometry of the DFA, including offsets in the delay profiles for azimuthal focusing on both the LF and HF stacks. These offsets were empirically determined using a needle hydrophone (HNA-0400, Onda Corporation, Sunnyvale, CA, USA). For B-mode, 200 focused ray lines and F-number of 1.5 were used. In both modes, uncompressed, envelope-detected, beamformed radiofrequency data were saved for offline analysis. In all experiments, frame rate was selected to allow comparison between the DFA system and the DF wobbler systems described previously (26,35).

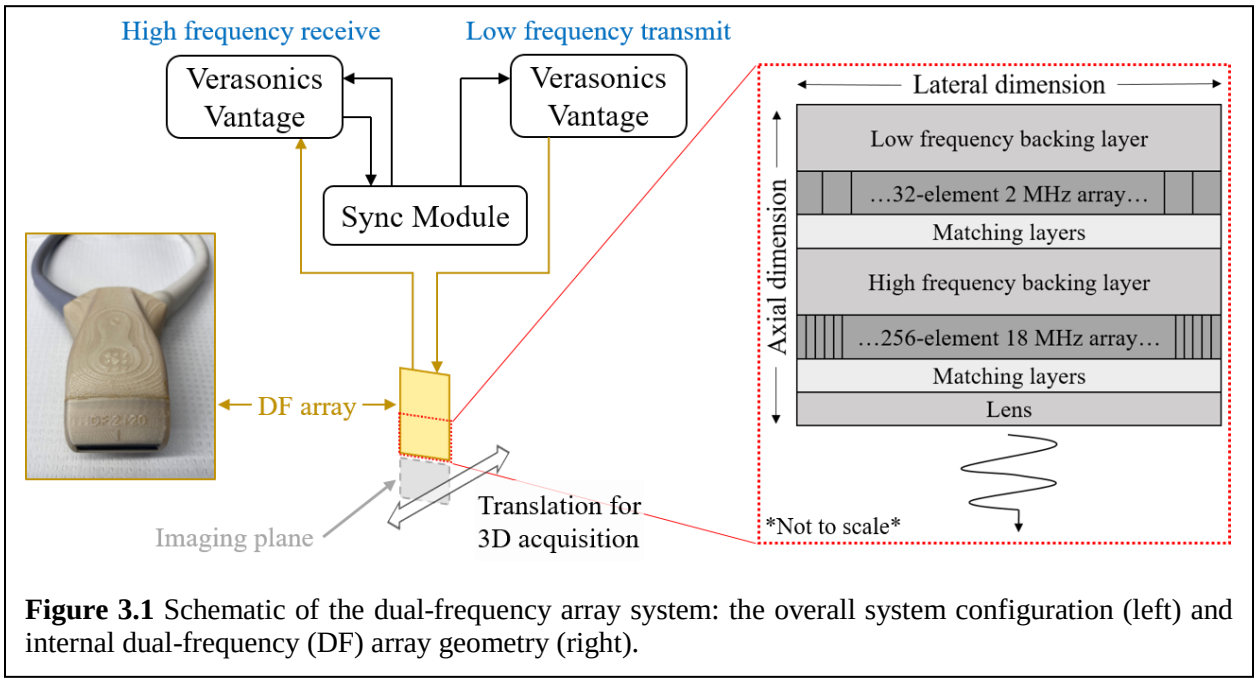

Figure 3.1 Schematic of the dual-frequency array system: the overall system configuration (left) and internal dual-frequency (DF) array geometry (right).

To acquire 3D image stacks, the DFA was attached to a linear translation stage (Velmex, Inc., Bloomfield, NY, USA) controlled by a custom program (LabVIEW, National Instruments, Austin, TX, USA). Translation of the stage was triggered by the imaging system, and image stacks were collected with 0.1 mm between slices. The number of slices per scan was determined by tumor size and ranged from 50 to 200 slices, corresponding to elevation distances of 5 to 20 mm.

3.2.2 Acoustic Characterization

The beam alignment and pressure output of the DFA were measured in degassed water with a calibrated needle hydrophone (HNA-0400, Onda Corporation, Sunnyvale, CA, USA) and a digital three-axis motion stage (Newport Corporation, Irvine, CA, USA). Acoustic signals were digitized (CSE1222, DynamicSignals LLC, Lockport, IL, USA) and recorded with a custom acquisition program (LabVIEW, National Instruments, Austin, TX, USA). Pressure maps in the elevational-axial dimension were collected with plane wave transmissions to demonstrate the effect of the elevation lens on the array. Pressure maps were acquired with 250-μm axial and 100-μm lateral or elevational grid spacing and linearly interpolated to a 50-μm grid for display.

For frequency bandwidth measurements, a calibrated high-frequency needle hydrophone (NH0040, Precision Acoustics, Dorchester, UK) was used to acquire single-cycle transmit waveforms from both LF and HF stacks. For each stack, a single transmit beam axially focused at 10 mm and laterally centered was generated, and 150 waveforms were recorded at a pulse repetition frequency of 10 Hz. Waveforms were recorded and digitized as described above. All data analysis presented in this work was performed in MATLAB (Mathworks, Natick, MA, USA). To obtain the frequency responses, the 150 signals from each stack were averaged, and a fast Fourier transform was performed. The center frequency of each stack was measured as the

maximum of the magnitude of the Fourier transform, and the -6 dB cutoff frequencies were measured relative to the center frequency.

3.2.3 Contrast Agent Formulation

The contrast agent used in this work was an in-house formulation of lipid-shelled, perfluorocarbon-filled microbubbles, as previously described (35,142). Briefly, a 9:1 molar mixture of distearoylphosphatidyl-choline (18:0 PC, Avanti Polar Lipids, Alabaster, AL, USA) and PEGylated dipalmitoylphosphatidyl-ethanolamine (16:0 PEG2000 PE, Avanti Polar Lipids, Alabaster, AL, USA) was prepared in phosphate buffered saline (PBS) containing 15% (v/v) propylene glycol and 5% (v/v) glycerol. After preparation, the lipid solution was aliquoted into cleaned 3 mL vials, and the air headspace in each vial was replaced with decafluorobutane gas (Fluoromed, Round Rock, TX, USA). Contrast was activated with a mechanical agitator (Vialmix, Lantheus Medical Imaging, North Billerica, MA, USA) to form polydisperse microbubbles. The average size and undiluted concentration of these MCAs as measured by single particle optical sizing (Accusizer 780A, Particle Sizing Systems, Santa Barbara, CA, USA) were 0.96 μm and $3.1x10^{10}$ microbubbles/mL, respectively.

3.2.4 In Vitro *Resolution*

To assess the resolution of the imaging system, an *in vitro* experiment was performed. A beaker containing 575 mL of distilled water was placed on a stir plate (Thermolyne Cimarec, Barnstead International, Dubuque, IO, USA) and constantly mixed with a magnetic stir bar on the lowest setting to prevent contrast microbubbles from floating during data acquisition. A solution containing approximately $1.87x10^5$ microbubbles was injected into the bath to create a suspension of spatially separated bubbles. The bubble solution was imaged in DF-mode with a frame rate of 4 fps and focal depth between 5 – 30 mm in 5 mm increments. The maximum driving voltage (28

V) was applied at all depths to maximize pressure and signal-to-noise ratio. At each depth, 100 frames were collected.

In vitro resolution was analyzed as follows. For each focal depth, each frame was cropped to 1 mm on either side of the focal depth (*e.g.*, for 5 mm focal depth, images were cropped to 4 – 6 mm axial range). For any single bubbles in this region, lateral and axial profiles were extracted using the "improfile" function in MATLAB. The profiles were normalized, and the resolution was computed as the full width at half-maximum (FWHM) for each profile. The final resolution metrics were the average FWHMs in each direction. At least 100 bubbles were measured for each focal depth.

3.2.5 In Vitro *Sensitivity*

To measure the sensitivity of the imaging system to contrast, a regenerated cellulose tube with 200 µm inner diameter (Spectrum Laboratories, Rancho Dominguez, CA, USA) was suspended in a water bath orthogonal to the axis of propagation, such that the length of the tube was in the imaging plane. The depth of the tube from the transducer surface was varied with the focal depth of the imaging scheme from 7.5 – 27 mm, and alignment was confirmed with B-mode imaging. The peak rarefactional pressure was held constant at 490 kPa for all depths (MI = 0.35), and a frame rate of 4 fps was employed to allow the tube to fully perfuse between frames. MCAs were diluted in PBS to $1x10^7$ microbubbles/mL and infused through the microtube at a volume flow rate of 60 µL/min (31.8 mm/s) with a syringe pump (Pump 11 Elite, Harvard Apparatus, Holliston, MA, USA). Three trials were performed for each depth with a fresh MCA dilution prepared for each trial, and 50 frames were collected while contrast was flowing. For comparison, data was also collected with a DF wobbler probe as previously described (26,27). Briefly, a single-cycle cosine-windowed sine wave was transmitted at 4 MHz and MI = 0.35 with the LF element

of the wobbler, while a preclinical HF scanner controlled receive at 30 MHz center frequency with a 15 MHz high-pass filter on the receive line (Vevo 770, FUJIFILM VisualSonics, Inc., Toronto, ON, Canada). Compressed image data were saved for analysis.

In vitro sensitivity was quantified by contrast-to-noise ratio (CNR) as defined below. For each depth, a maximum intensity projection (MIP) was created from the image stack. Each MIP was used to draw regions of interest (ROIs) for "contrast" within the tube and "noise" in the surrounding water. Next, the mean envelope amplitude inside each ROI was computed for each frame. CNR was defined as:

$$CNR = 20\log_{10}\left(\frac{E_{contrast}}{E_{noise}}\right), \quad \textbf{Eq. 3.1}$$

where $E_{contrast}$ and E_{noise} were the mean envelope amplitudes inside the contrast and noise ROIs, respectively. To obtain the final CNR metric, the CNR values were averaged over the 150 frames collected over three trials for each depth.

3.2.6 In Vivo *Imaging*

All animal studies performed in this work were approved by the University of North Carolina Institutional Animal Care and Use Committee. Subcutaneous fibrosarcoma tumors in female rats (Fischer 344, Charles River Laboratories, Wilmington, MA, USA) were imaged. This tumor model has been described previously (143) and was chosen for its well-vascularized tumors characterized by increased vascular density and tortuosity (34,43). Briefly, fibrosarcoma tissue (1 mm^3) from donor rats was implanted subcutaneously in the right flank. Tumor allografts grew for approximately two weeks before imaging, and animals were humanely euthanized when tumors reached 2 cm in the largest dimension.

For imaging, rats were anesthetized with vaporized isoflurane (induced at 5%, maintained at 2 – 2.5%), and the skin surrounding the tumor was shaved. A catheter was inserted in the tail vein for administration of MCAs, which was performed with an infusion pump (Pump 11 Elite, Harvard Apparatus, Holliston, MA, USA) with a 15 µL/min volume flow rate. MCAs were diluted in sterile saline to a concentration of $1.5x10^{10}$ microbubbles/mL before infusion, resulting in an effective circulating concentration in the range of 0.5 – $1.5x10^{8}$ microbubbles/mL. A water bath and ultrasound gel were used to couple the transducer to the animal's skin. For *in vivo* imaging, the focal depth of the DFA was set equal to the center of the tumor, frame rate was set to 4 fps, and MI = 0.48 was used. Tumors were imaged with both the DFA and a DF wobbler for comparison, as described in the previous section. On the DFA system, four frames were averaged at each position, compared to five frames on the wobbler system. DFA images collected on the Verasonics Vantage were formed by log-compressing envelope-detected data and were displayed with 44 dB dynamic range. However, the Vevo770 used in this work could not provide uncompressed data; instead, it exported 8-bit images with unknown compression. Therefore, the dynamic range for display of DF wobbler images was chosen such that image contrast was comparable to the corresponding DFA image when displayed at 44 dB. Images are displayed as MIPs unless otherwise specified. Because the wobbler and array had to be physically moved to acquire images of the same tumor, a true slice-by-slice comparison could not be achieved. MIPs were therefore used to compare approximately the same volume with each device.

3.3 Results

3.3.1 Acoustic Characterization

The results of hydrophone measurements are shown in **Figure 3.2**. **Figure 3.2A** provides the frequency bandwidths measured on transmit for the LF and HF stacks. The center frequency

of the LF array was measured at 1.95 MHz with -6 dB cutoffs at 1.32 and 2.55 MHz. For the HF array, a center frequency of 17.1 MHz was measured, and the -6 dB bandwidth reached from 13.4 to 22.6 MHz. The -20 dB lower and upper cutoffs of the main lobe of the HF bandwidth were 10.8 and 28.3 MHz, respectively.

Maximum rarefactional pressure output was generated by the LF stack for a focal depth of 10 mm, producing 674 kPa and corresponding to MI = 0.48 (**Figure 3.2B**). Based on these

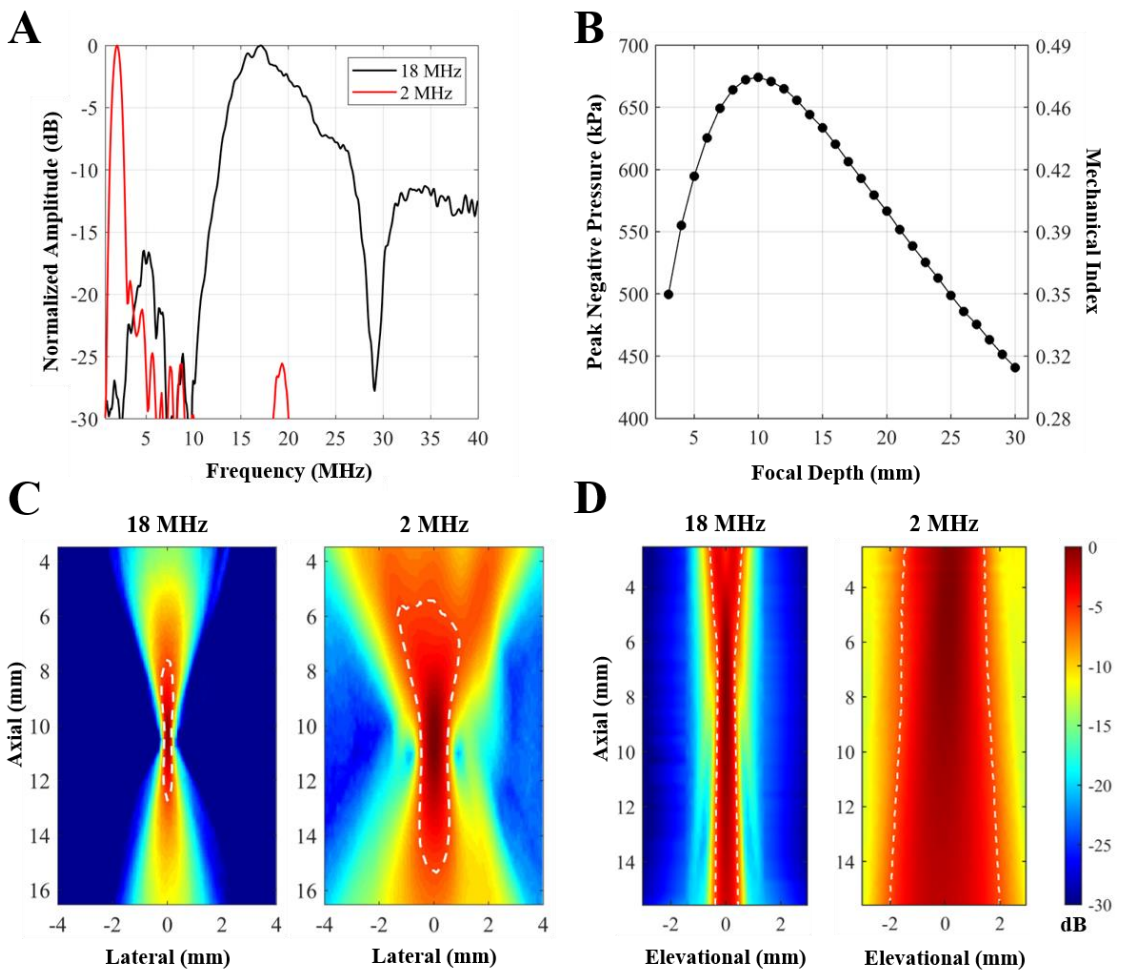

Figure 3.2 Acoustic characterization of the dual-frequency array: **A)** transmit frequency bandwidths of the 2 MHz (red) and 18 MHz (black) stacks; **B)** maximum peak rarefactional pressure vs. focal depth for constant applied voltage (28 V) on the 2 MHz stack; **C)** lateral-axial pressure maps demonstrating effective electronic focusing in azimuth and alignment of both beams at 10 mm focal depth; and **D)** elevational-axial pressure maps showing the beam thickness in elevation. On all pressure maps, the -6 dB beamwidth is denoted by the white contour.

measurements, imaging in DF-mode can be performed in the range of MI = 0.3 – 0.5 for depths up to 3 cm. The LF and HF beams produced by electronic focusing at 10 mm depth are shown in **Figure 3.2C**. Here, the white contour denotes the -6 dB beamwidth for each array, confirming alignment of the beams for coaxial dual-frequency imaging. Furthermore, the LF and HF beams are shown in elevation in **Figure 3.2D**. The HF beam was narrowest from 6 – 12 mm axially, due to the elevational lens on the DFA; over this range, the average elevational beamwidth was 0.7 mm. At all depths, the LF beamwidth was larger than 3 mm.

3.3.2 In Vitro *Resolution*

Figure 3.3 depicts the axial and lateral resolution of the DFA measured *in vitro*. The theory surrounding superharmonic imaging is complex, but in general, the received pulse is determined by the nonlinear response of the microbubble shell, which is especially high frequency when the shell is disrupted. Here, the system is sensitive to signals up to 30 MHz, based on the transducer bandwidth and receive sampling and filtering used. Measurements show an average axial resolution of 68.4 µm. Near the HF focus of the elevation lens of the array at 10 mm, lateral resolution is measured as 104.6 µm. **Table 3.1** provides all resolution values measured in this experiment.

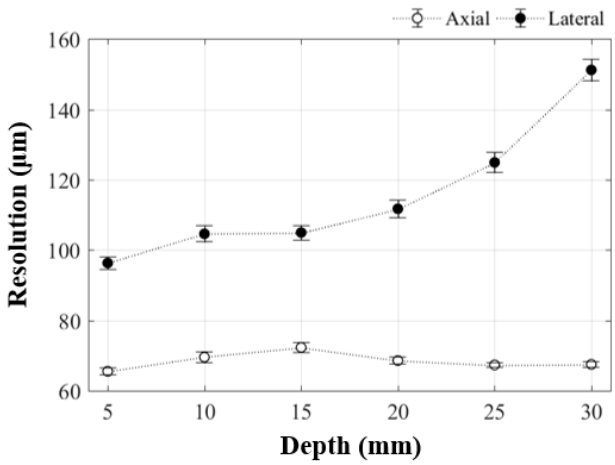

Figure 3.3 *In vitro* measurement of axial and lateral resolution *vs.* focal depth. Data presented as mean full-width at half-maximum ± standard error.

Table 3.1: *In vitro* resolution measurements.

Depth (mm)	Number of Bubbles	Axial Resolution (µm)	Lateral Resolution (µm)
5	160	65.5 ± 1.0	96.3 ± 1.7
10	121	69.5 ± 1.6	104.6 ± 2.3
15	127	72.3 ± 1.3	105.0 ± 2.1
20	117	68.6 ± 0.9	111.7 ± 2.5
25	116	67.3 ± 0.7	124.9 ± 2.9
30	115	67.5 ± 0.8	151.2 ± 3.1

Data presented as mean full-width at half-maximum ± standard error.

Table 3.2: *In vitro* sensitivity measurements.

Depth (mm)	Wobbler CNR (dB)	Array CNR (dB)
7.5	0.4 ± 0.1	33.4 ± 0.5
10	5.2 ± 0.4	38.8 ± 0.4
12	14.2 ± 0.3	37.7 ± 0.8
15	21.7 ± 0.3	34.8 ± 0.6
17	20.9 ± 0.5	35.9 ± 0.9
20	19.7 ± 0.4	35.1 ± 0.9
24	12.5 ± 2.6	33.2 ± 1.0
27	----------	34.6 ± 0.6

Data presented as mean ± standard deviation. CNR = contrast-to-noise ratio.

3.3.3 In Vitro *Sensitivity*

Results of the *in vitro* sensitivity experiment are given in **Figure 3.4**. Example MIPs collected with the DF wobbler system and the DFA system at a focal depth of 20 mm are shown in **Figure 3.4A** and **3.4B**, respectively. The ROIs used for CNR calculation are provided for reference. It should be noted that the post-excitation peaks (86,144), observed as an extension of signal outside the tube in the axial dimension, were not included in the contrast ROI. While these signals are present in this water bath experiment, they are not typically observed in attenuating media, such as tissue. **Figure 3.4C** gives CNR as a function of focal depth for the two devices. Here, we observe roughly constant CNR for all depths with the DFA, illustrating the benefit of using electronic focusing to match target depth and maintain constant pressure. The DFA exhibits maximum CNR (38.8 dB) at 10 mm, near the elevation focus of the HF array. At 15 mm, we find

that the DFA system achieves 13.1 dB greater CNR compared to the wobbler system at the same MI. As expected, the CNR achieved with the wobbler probe follows a Gaussian shape, with maximum CNR at the focal depth of 15 mm. The limited field of view of the DF wobbler did not allow calculation of CNR at a depth of 27 mm. All measured CNR values are listed in **Table 3.2**.

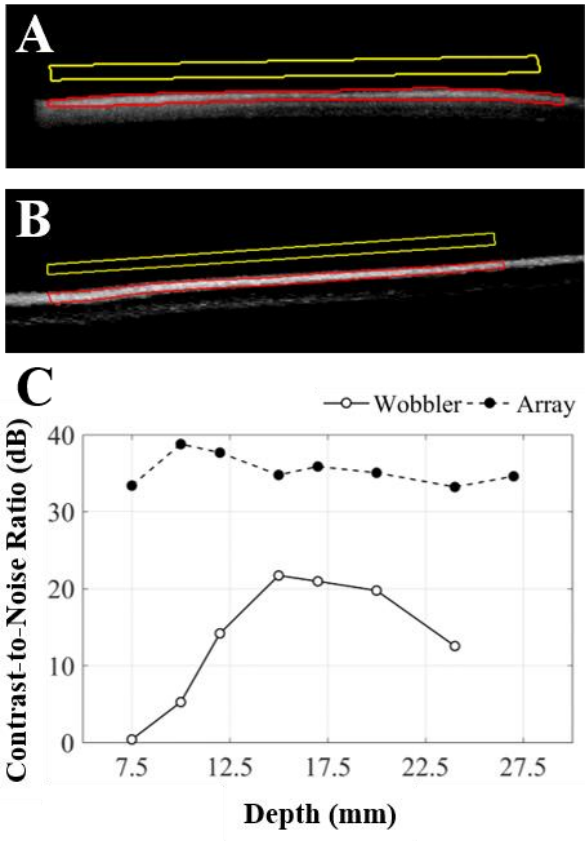

Figure 3.4 *In vitro* contrast-to-noise ratio measurement: example maximum intensity projections at 20 mm depth for the dual-frequency **A)** wobbler and **B)** array systems with contrast (red) and noise (yellow) regions of interest and **C)** mean contrast-to-noise ratio for increasing focal depth.

3.3.4 In Vivo *Imaging*

Figure 3.5 provides B-mode slices (**A – B**) and DF-mode MIPs (**C – D**) of a large rat fibrosarcoma tumor, demonstrating the ability of the DFA to perform high-contrast acoustic angiography *in vivo*. This dataset consisted of 220 slices and was acquired in less than 5 minutes. In comparison to the DF wobbler system, the DFA system exhibits comparable resolution with

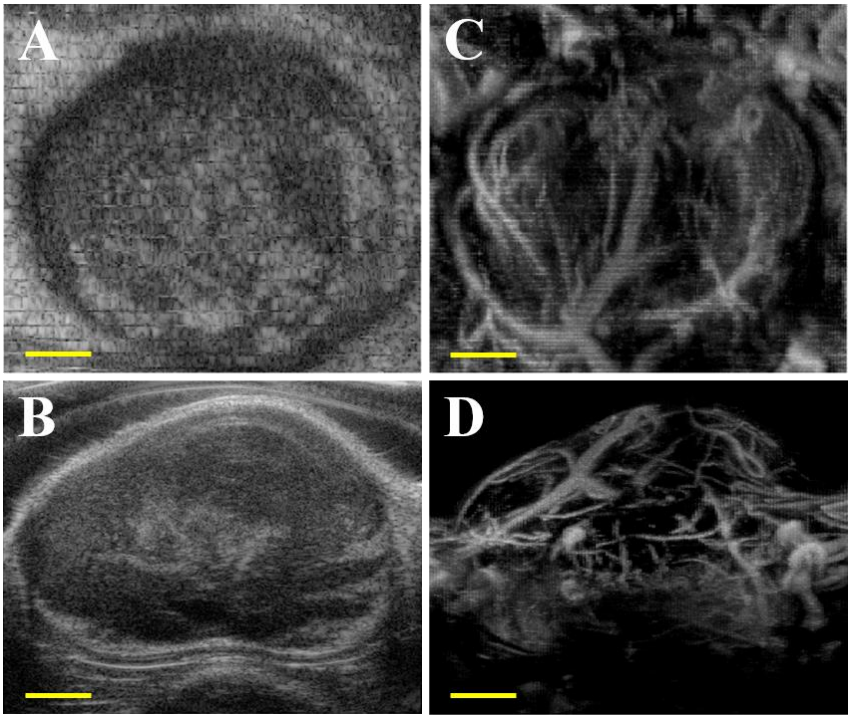

Figure 3.5 *In vivo* images of a 20 mm rat fibrosarcoma tumor acquired with the dual-frequency array system: **A – B)** high-frequency B-mode, **C – D)** dual-frequency acoustic angiography. B-mode images are single slices from the 3D dataset, while dual-frequency images are presented as maximum intensity projections in either the sagittal **(C)** or transverse **(D)** plane. Scale bar = 4 mm.

higher sensitivity, shown by greater MCA signal and reduced contamination from artifact (**Figure 3.6**). In **Figure 3.6 (B – C)**, when imaging with the wobbler, we observe bright artifacts from the animal's skin (indicated by arrows) that do not appear when imaging with the DFA, as shown in **Figure 3.6 (E – F)**. The DFA also exhibits 4 – 5 mm greater depth of field (*i.e.*, the axial range over which the transducer is sensitive to microbubble signals) than the DF wobbler (**Figure 3.6C** & **3.6F**) using a single-focal-zone imaging scheme. Finally, the DFA system is able to resolve vessels *in vivo* on the order of 100 – 200 μm, as illustrated in **Figure 3.7**.

3.4 Discussion

In this chapter, we have presented a novel imaging system consisting of a coaxially stacked dual-frequency array and programmable research scanners for performing acoustic angiography.

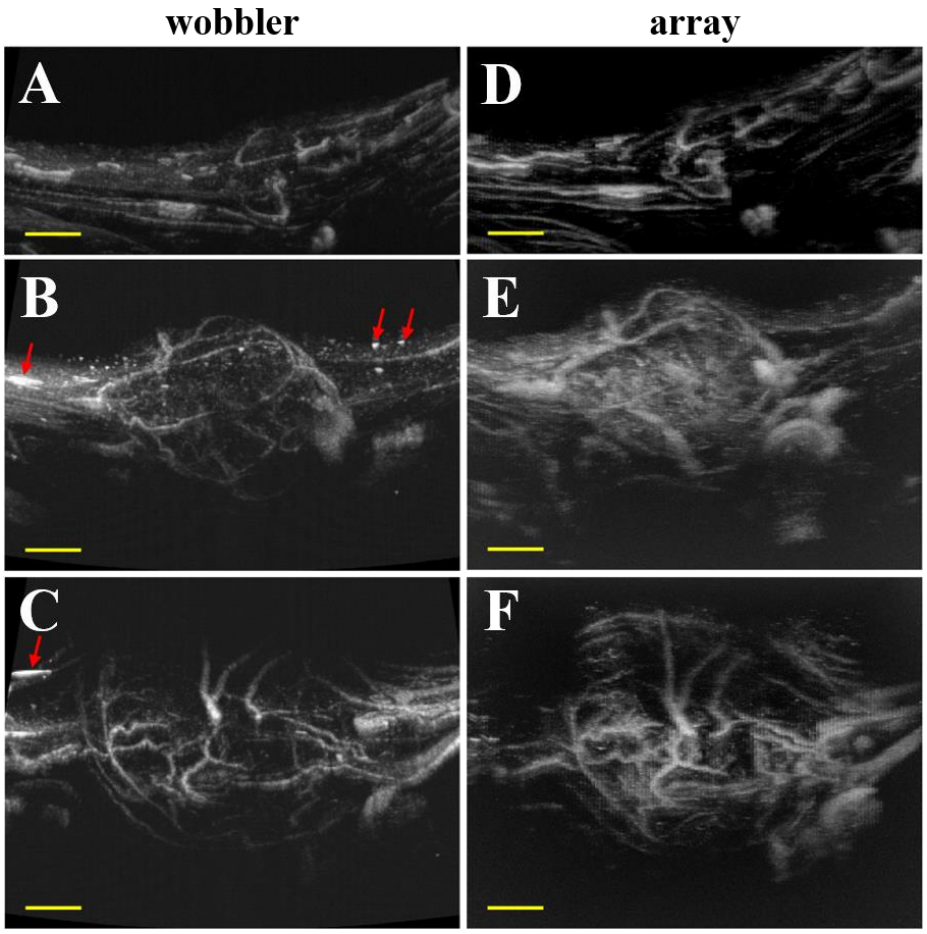

Figure 3.6 Comparison of *in vivo* images of three different tumors imaged with the dual-frequency wobbler or array systems: wobbler **(A – C)** or array **(D – F)**. Images are presented as maximum intensity projections in the transverse plane. Red arrows indicate skin artifacts. Scale bar = 3 mm.

Overall, the results demonstrate that this system can be used for high-sensitivity, high-resolution DF-mode imaging up to 27 mm in depth. The device described in this work differs significantly from the interleaved or co-linear dual-frequency array transducers implemented in previous works (21,145,146). Here, the integrated stacked design of the DFA allows for truly coaxial imaging. Conversely, co-linear array designs have a fixed elevation focus dependent on the intersection of the outer beams (145,146). While interleaved arrays can have more ergonomic designs than co-linear probes, they can suffer from the presence of grating lobes (21). The DFA used here does not suffer from these limitations, but the design of appropriate stacking layers and aperture sizes for

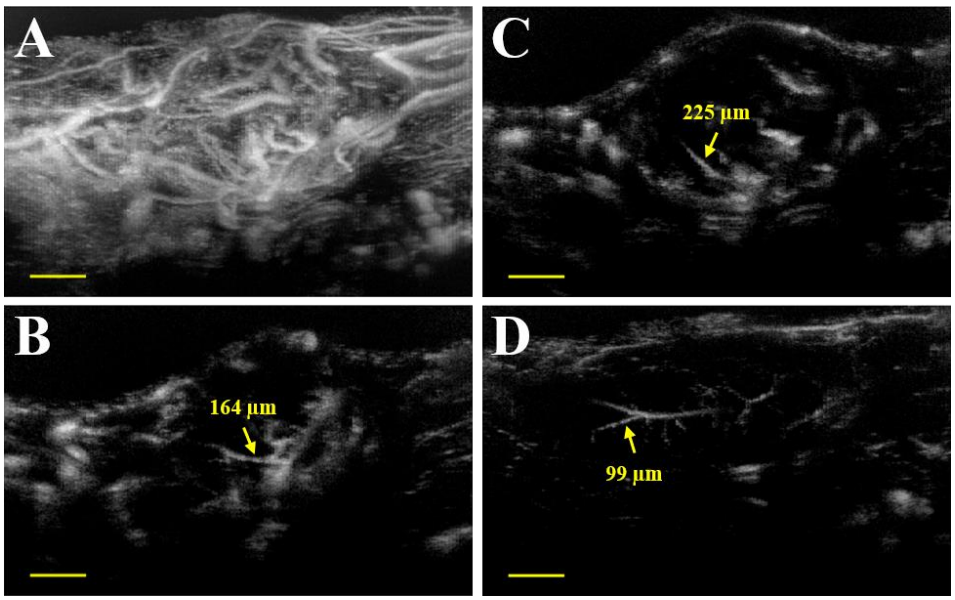

Figure 3.7 *In vivo* images of an 11 mm rat fibrosarcoma tumor acquired with the dual-frequency array system: **A)** Maximum intensity projection through a 15 mm scan of the tumor and **B – D)** single slices taken from positions 3.5 mm **(B)**, 6.9 mm **(C)**, and 14.6 mm **(D)** in the dataset, illustrating resolution of 100 – 200 µm vessels. Images are displayed in the transverse plane. Scale bar = 3 mm.

such a device can be technically challenging. While other coaxial DF transducer designs have been reported for intravascular and intracavitary applications of superharmonic imaging (147–149), the transducer implemented in this study represents the first coaxially integrated transcutaneous DF array used for acoustic angiography. Detailed reviews on dual-frequency transducer technology for superharmonic imaging can be found elsewhere (140,150).

The beamwidth of the DFA in elevation is 0.7 mm for the HF stack and >3 mm for the LF stack. In comparison, the elevation beamwidth of the wobbler probe used in this work is 0.36 mm for the HF element and 0.46 mm for the LF element (similar to the device described in (27)). Conventionally, the acoustic point spread function (PSF) is equal to the convolution of the transmit and receive PSFs. For dual-frequency imaging, however, the system PSF is more complex and is affected by the highly nonlinear bubble response, in addition to the transmit and receive beams. While the HF receive PSF contributes to the resolution of superharmonic imaging, other factors,

including the transmit beam shape and amplitude and the microbubble response, also affect the overall system PSF. In this work, the wobbler probe likely has a smaller overall PSF in elevation and therefore better resolution in this dimension compared to the array. These effects must be considered in the design of future DF arrays.

While an improvement in sensitivity was expected when transitioning to the DFA system, the difference in superharmonic artifacts within the *in vivo* images (usually from skin or bone) was unexpected. It should be noted that the positioning of the coupling gel and water bath was not altered when switching between the DF array and wobbler devices. There are two central differences between the array and wobbler systems that may be responsible for this phenomenon. First, there is a great difference in the frequencies used for acoustic angiography with a wobbler compared to the array. With the DF wobbler transducers described in the past, the fundamental (*i.e.*, transmit) frequency was 4 MHz, while the center frequency of the receive bandwidth was the 6^{th} – 7^{th} harmonic (25 – 30 MHz) (27,34,35). On the contrary, with the DFA presented here, the fundamental frequency was 2 MHz, and the center frequency of the receive bandwidth was the 8^{th} – 9^{th} harmonic. Second, on receive, the wobbler is a single-element system, while the DFA system receives with 256 elements. The beamforming used on each system is therefore very different, and the high number of elements on the DFA may make this system less susceptible to clutter. Taken together, these two disparities may be responsible for the higher prevalence of artifacts within wobbler images.

The system described in this work can resolve vessels on the order of 100 μm in diameter at depths less than 3 cm. While this array represents a step toward the clinical translation of acoustic angiography, DF transducers that can image at more clinically relevant depths will be necessary. The development of such devices will likely require reducing the transmit and receive

frequencies further to accommodate the greater attenuation of high frequency signals that will be encountered when imaging at depth, in addition to improving the design of the transducer geometry for deeper imaging. Further work is needed to elucidate the best frequency combinations for performing acoustic angiography in relevant clinical scenarios, such as the evaluation of suspicious breast lesions. Translation to clinical applications warrants further investigation to optimize DF transducer designs, including finite-element modeling and experimental validation.

The potential impact of microvascular ultrasound imaging, initially enabled by techniques like acoustic angiography, likely motivated the development of ultrasound localization microscopy (ULM), a super-resolution ultrasound technique inspired by optical photo-activation localization microscopy (51,77,151). With ULM, vessels can be resolved well below the diffraction limit, on the order of 10 μm (77,78). However, the time required for image acquisition and processing can be quite lengthy for 3D applications when compared to acoustic angiography, in which volumes containing vessels on the order of 100 μm can be reconstructed in less than 5 minutes.

Our group has previously demonstrated that superharmonic imaging with a DF transducer can be used for high-sensitivity bubble detection for ULM (86). Using a prototype co-linear DF probe, the authors were able to image 20 μm vessels in a rodent kidney (86,145). While we have previously shown that acoustic angiography can be used to differentiate tumors from healthy tissue, this analysis was based on vessels with diameters greater than approximately 150 μm (34,35). The diagnostic power of this technique may be improved with the ability to analyze even smaller vessels for characteristics of malignancy. In the future, this combination of superharmonic imaging and ULM will be implemented on a DFA, such as the one described herein, for tumor imaging. This will allow real-time visualization of larger microvasculature with acoustic angiography, followed by detailed analysis of high-resolution vascular features with ULM.

However, for mechanically scanned techniques like superharmonic ULM and acoustic angiography, tissue motion between elevation slices can lead to errors in microvascular reconstruction. We have previously demonstrated that B-mode images interleaved with DF images can be used for speckle tracking and motion compensation (86). In future work, this approach can be implemented on the DFA system described in this work to improve visualization of microvasculature in high-motion targets, such as the human breast (48).

3.5 Conclusion

In this study, we have presented the first use of a novel system for acoustic angiography using a coaxially stacked dual-frequency array. This system allows acoustic angiography to be performed at depths up to 3 cm, an improvement of 1 cm over previous dual-frequency wobblers. Additionally, a reduction in transmit and receive frequencies allows an improvement in sensitivity of at least 13.1 dB *in vitro*, and we have shown that the DFA can resolve vessels as small as 100 μm *in vivo*. Overall, the integrated array and system presented herein represents the next step in dual-frequency technology to facilitate the clinical translation of acoustic angiography. Future work will focus on further improvements in imaging depth and sensitivity with dual-frequency transducers specifically designed for imaging in clinical applications.

CHAPTER 4
CLINICAL ACOUSTIC ANGIOGRAPHY WITH A DUAL-FREQUENCY ARRAY

4.1 Introduction

Currently, one in eight women will be diagnosed with breast cancer over the course of her lifetime (152). Annually in the United States, more than 250,000 women are diagnosed with breast cancer, and over 40,000 women die from the disease (152). To avoid breast cancer-related mortality, early detection is crucial. The leading method of breast cancer detection is screening mammography, which has been shown to decrease the incidence of mortality by as much as 20% (153,154). Lesions identified via mammography are typically subjected to follow up imaging, such as diagnostic mammography, tomosynthesis, magnetic resonance imaging, or ultrasound, and after this secondary imaging, each lesion is assigned a score of 1 – 6 in the Breast Imaging Reporting and Data System (BIRADS) (155). Lesions with scores of 4 – 5 are considered suspicious and will likely be recommended for biopsy (155). Based on this evaluation, up to 2% of screening mammograms lead to biopsy, of which more than 65% obtain benign results (153,156). This indicates that most of these biopsies are performed unnecessarily, causing needless physical and emotional trauma for patients and an estimated annual cost of more than $2 billion in the United States (157).

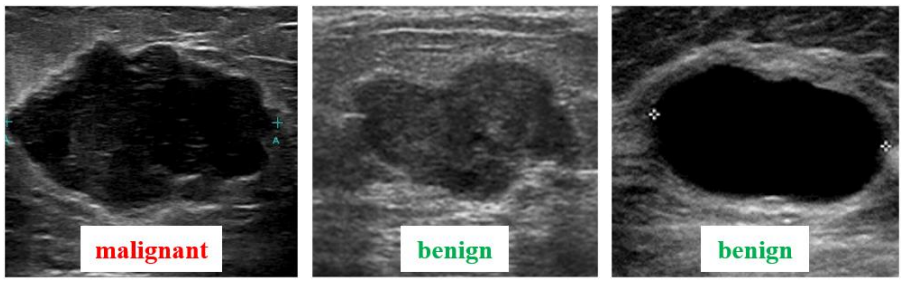

Figure 4.1 Example ultrasound images of suspicious breast lesions: malignant infiltrating ductal carcinoma (left), benign papilloma (center), and benign cyst (right).

As a breast cancer imaging tool, ultrasound suffers from poor specificity and increased false-positive rates compared to other modalities (158). An illustrative breast ultrasound example is provided in **Figure 4.1**. In this example, three lesions exhibit similar features when examined with ultrasound, though only one lesion is malignant. Because it is a safe, affordable, and widely available imaging modality, ultrasound is an excellent candidate for secondary breast imaging, but specificity must be improved.

Acoustic angiography, a superharmonic contrast-enhanced ultrasound approach, is uniquely poised to improve the specificity of breast ultrasound by evaluating the microvascular features in addition to the tumor tissue (150). The vascular characteristics of tumor growth, including increased tortuosity and vascular density, are important biomarkers of malignancy and may provide an opportunity to improve tumor identification and diagnosis (159). To date, acoustic angiography in humans has exhibited limited success, largely determined by the capabilities of the dual-frequency transducers used for imaging. While the high resolution of acoustic angiography was maintained in human patients, Shelton *et al.* (48) demonstrated that both the depth and sensitivity of the technique must be improved in order for clinical translation to be successful. **Figure 4.2** provides example images from a healthy breast volume from this pilot study. These data show that only sparse vasculature within 16 mm of the transducer surface was observed, and the wobbler transducer was only sensitive in a narrow region above this depth (9 – 16 mm).

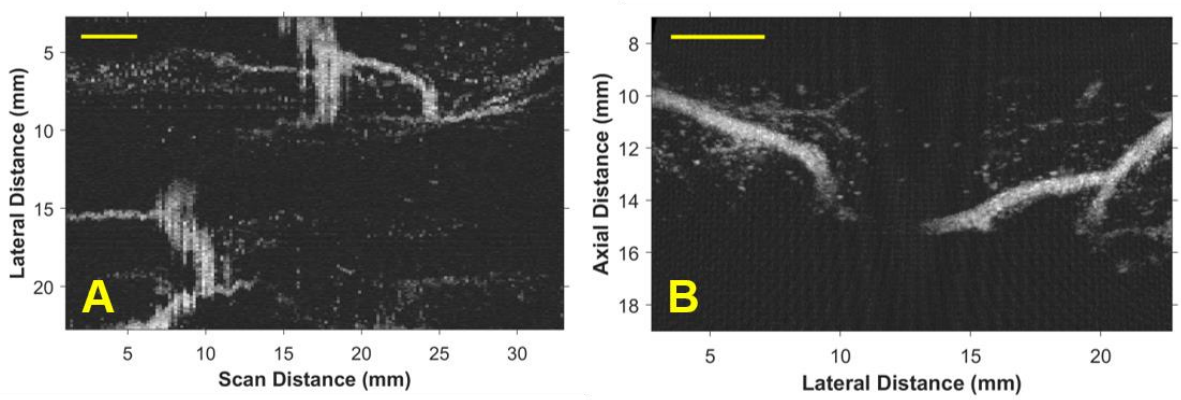

Figure 4.2 Example images of healthy breast collected with a wobbler probe: **A)** maximum intensity projection through depth, showing sparse vasculature throughout the volume; **B)** maximum intensity projection through elevation, showing limited imaging depth. In both images, scale bar = 4 mm.

The next-generation dual-frequency array (DFA) described in Chapter 3 has demonstrated the potential to improve image sensitivity by up to 13 dB and depth-of-field by up to 5 mm in a preclinical study (160). In this chapter, this DFA is used to perform acoustic angiography in a clinical study, and the results are compared to previous in-human acoustic angiography data collected with "wobbler" probes.

4.2 Materials and Methods

4.2.1 Study Design

To investigate the DFA's potential capability to perform acoustic angiography imaging in humans, a pilot clinical study was performed. All clinical work was approved by the University of North Carolina at Chapel Hill Institutional Review Board, and all study subjects provided informed consent. The study protocol is outlined in **Figure 4.3**. The study included two subject cohorts – healthy volunteers and patients with breast lesions.

In healthy volunteers, peripheral vasculature was imaged in the limbs or neck, and these data were used to validate and optimize the DFA imaging system for clinical use. For the patient cohort, subjects who had suspicious breast lesions identified via standard-of-care screening and

required biopsy were enrolled. At the time of this dissertation, fifteen volunteers and three patients had been imaged.

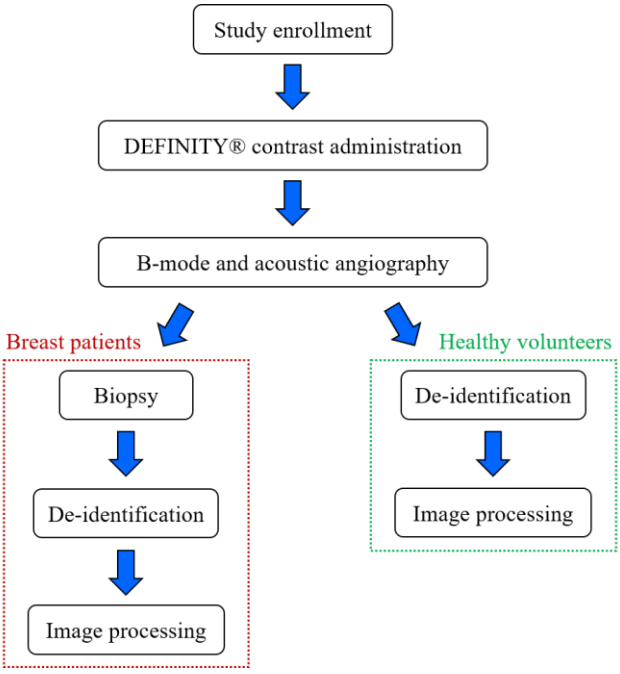

Figure 4.3 Diagram outlining protocol for clinical study. All data were de-identified upon acquisition.

4.2.2 Image Acquisition and Processing

The dual-frequency array imaging system, as described in Chapter 3 and documented in Appendix A, was used for all clinical data acquisition (160). B-mode volumes were collected with the high-frequency stack at 15.625 MHz, 8 fps, and MI < 0.8 before contrast administration to locate lesions and provide baseline anatomical information. An example B-mode slice shows two small lesions in the breast (**Figure 4.4**). For DF imaging, frame rate was set to 4 – 6 fps, and the maximum imaging pressure was used (0.30 < MI < 0.48) for 2 MHz transmit on the low-frequency stack. **Table 4.1** lists relevant parameters for the DFA imaging system implemented in this work and the previously used wobbler system for comparison. For volumetric acquisition, 3D stacks

were collected with 0.15 – 0.25 mm steps between slices, and 2 – 4 frames were averaged for each slice. DEFINITY contrast agent was administered at the recommended dose, 10 µL/kg, (114) by trained medical personnel via intravenous injection followed by a saline flush, and the 3D acquisition was initiated as soon as contrast was visible in DF-mode. Data acquisition was completed in no more than fifteen minutes per subject. After collection, all data were de-identified for patient protection. Data were log-compressed and displayed in MATLAB (Mathworks, Inc., Natick, MA, USA) as maximum intensity projections (MIPs) or in the open-source 3D Slicer software (161) as 3D renderings.

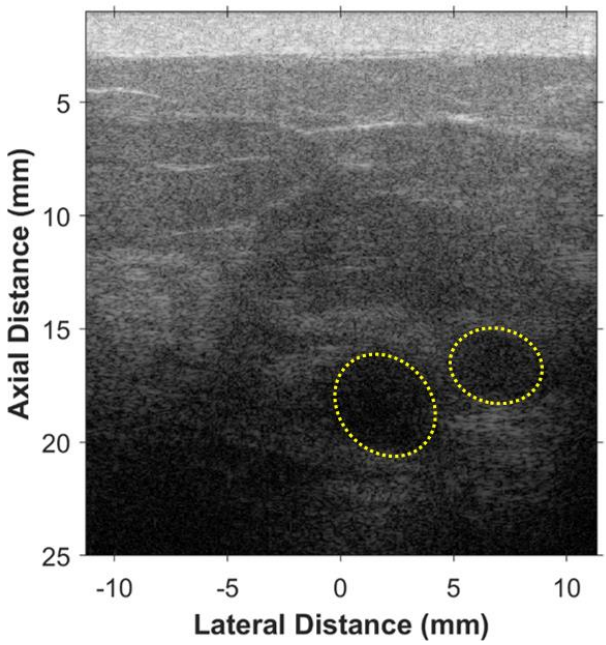

Figure 4.4 Example high-frequency B-mode image of suspicious breast lesions collected with the dual-frequency array. Yellow contours denote lesion locations.

Table 4.1: Comparison of acoustic angiography systems.

	DF array	DF wobbler
Transmit frequency	2 MHz	4 MHz
Receive frequency	18 MHz	30 MHz
Maximum imaging depth	30 mm	20 mm
Maximum MI	0.48	0.80

DF = dual-frequency. MI = mechanical index.

4.3 Results

4.3.1 Peripheral Vasculature in the Limbs

For initial characterization of the DFA imaging system in humans, peripheral vasculature in the hand and wrist was imaged in healthy volunteers. These targets provided an opportunity to assess the sensitivity and resolution of the system in shallow vasculature with little physiological motion. In the wrist, the radial artery was easily detected (**Figure 4.5A**). Compared to the same anatomy imaged with a wobbler transducer in the previous study (48), the DFA achieved a 3 dB increase in contrast-to-tissue ratio (CTR) at a lower MI (CTR = 9.3 dB at MI = 0.48 with the DFA *vs.* CTR = 6.1 dB at MI = 0.60 with the wobbler). In the palm, the DFA captured the structure of the palmar arterial branch with CTR up to 21 dB, as well as a nearby vessel measuring 225 μm in diameter (**Figure 4.5B**). These data serve to demonstrate the high resolution and sensitivity of acoustic angiography with the DFA.

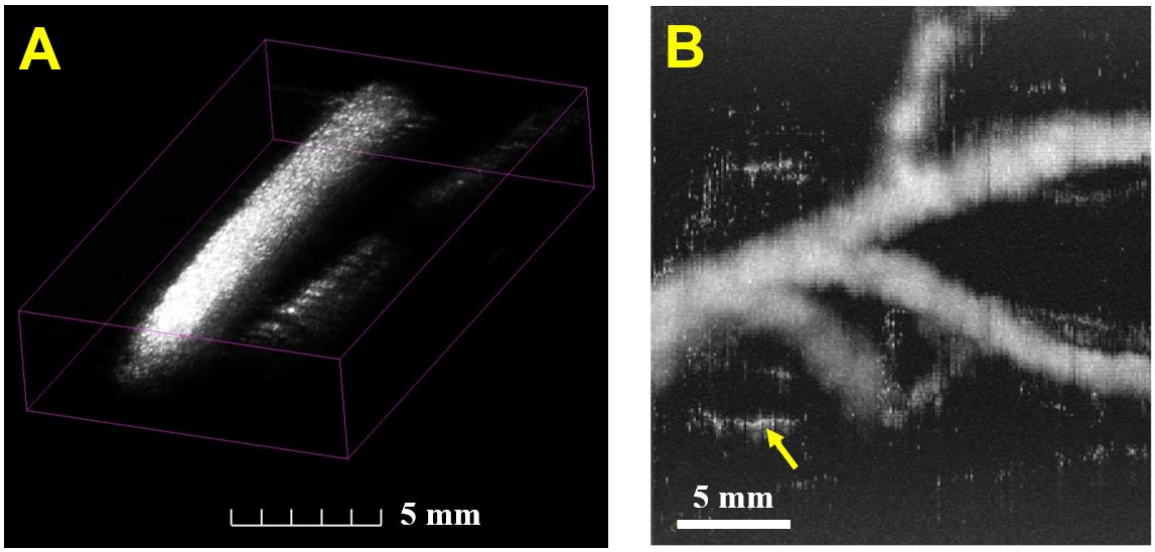

Figure 4.5 Images of peripheral vasculature in the limbs collected with the dual-frequency array: **A)** 3D rendering of the radial artery and **B)** maximum intensity projection through depth of arterial branching in the palm. Vessel indicated by yellow arrow is 225 μm in diameter.

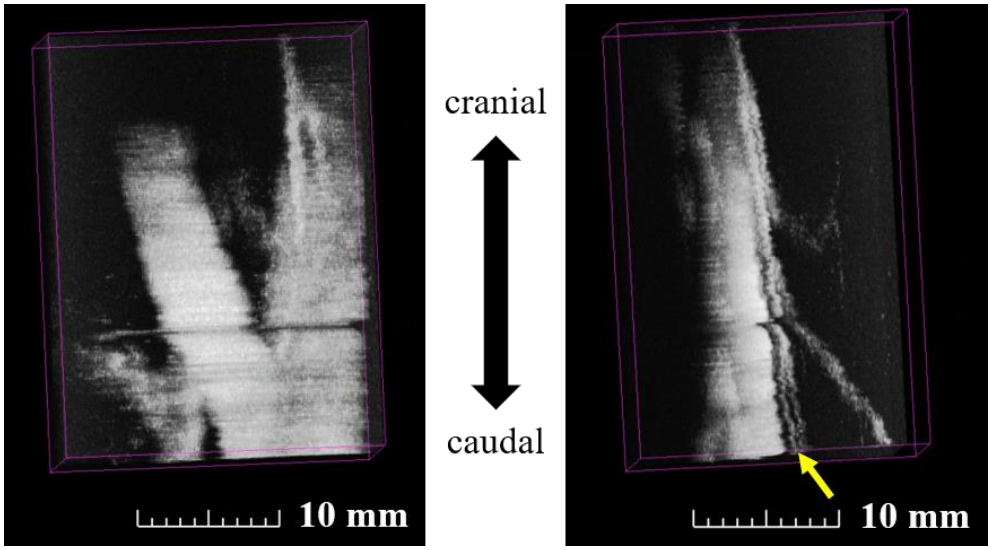

Figure 4.6 Two orthogonal views of the carotid artery bifurcation imaged with the dual-frequency array and rendered in 3D. Vessel indicated by yellow arrow is 600 μm in diameter.

4.3.2 Vasculature in the Neck

To evaluate the performance of the DFA in high-motion targets, the carotid artery and thyroid were imaged. These anatomies present interesting vascular structures in the presence of significant physiological motion, including motion caused by the heartbeat, respiration, and swallowing. The bifurcation of the carotid artery can be visualized with the DFA, and a nearby 600 μm vessel can be resolved despite the pulsation of the larger arteries (**Figure 4.6**). Similarly, the vasculature in and surrounding the thyroid, including sub-millimeter vessels, can be imaged with the DFA (**Figure 4.7**). Notably, the DFA is able to detect intravascular microbubble signals up to 30 mm in depth, an improvement of more than 10 mm compared to previous wobblers.

4.3.3 Vasculature in the Breast

After evaluating and optimizing imaging performance in other anatomies, the DFA system was applied for acoustic angiography imaging of the breast. Two example images of suspicious

breast lesions are provided in **Figure 4.8**. While larger vasculature is detected in the area surrounding these lesions with high CTR (15 – 18 dB), the DFA struggles to resolve the morphology of sub-millimeter vessels. Some breast lesions are relatively avascular (**Figure 4.8A** & **4.8C**), while others exhibit greater vasculature but suffer from respiratory motion (**Figure 4.8B**). **Figure 4.8D** shows a 3D rendering of the vasculature captured around the lesions shown in **Figure 4.4** and **4.8C**. In this case, no vasculature was resolved within the lesions, which agreed with the patient's standard-of-care imaging tests.

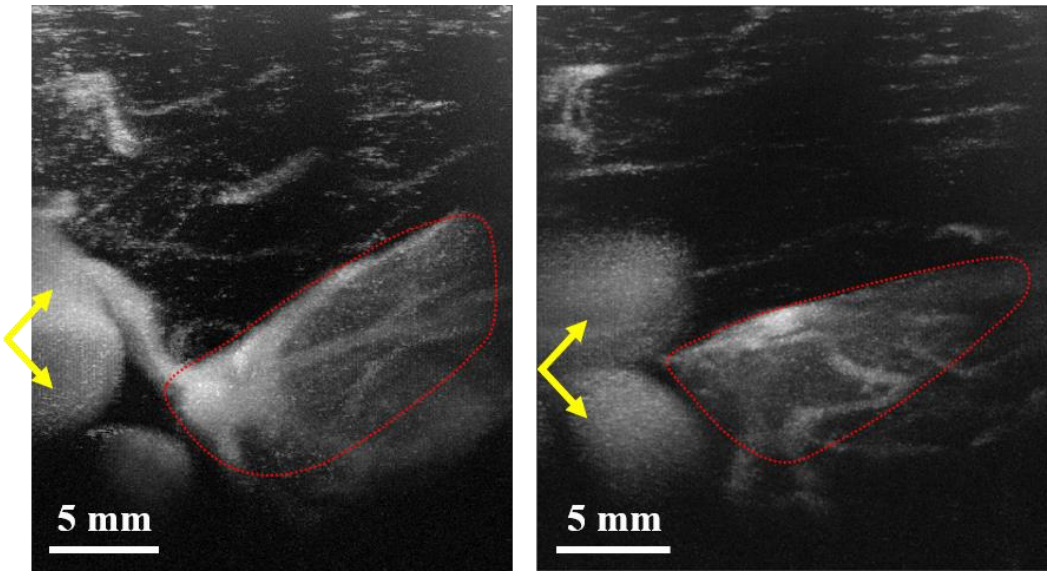

Figure 4.7 Representative maximum intensity projections of thyroids collected with the dual-frequency array in two healthy volunteers. In each image, the thyroid is outlined by the red contour, while the carotid artery and jugular vein are indicated by the yellow arrows.

4.4 Challenges Facing Clinical Acoustic Angiography

The clinical data presented in this chapter serve to illustrate the obstacles that are yet to be overcome for the successful clinical translation of acoustic angiography. While the DFA imaging system has increased imaging depth by 10 mm, the maximum depth of acoustic angiography with this device remains only 30 mm. In B-mode (transmit and receive at the same frequency), imaging

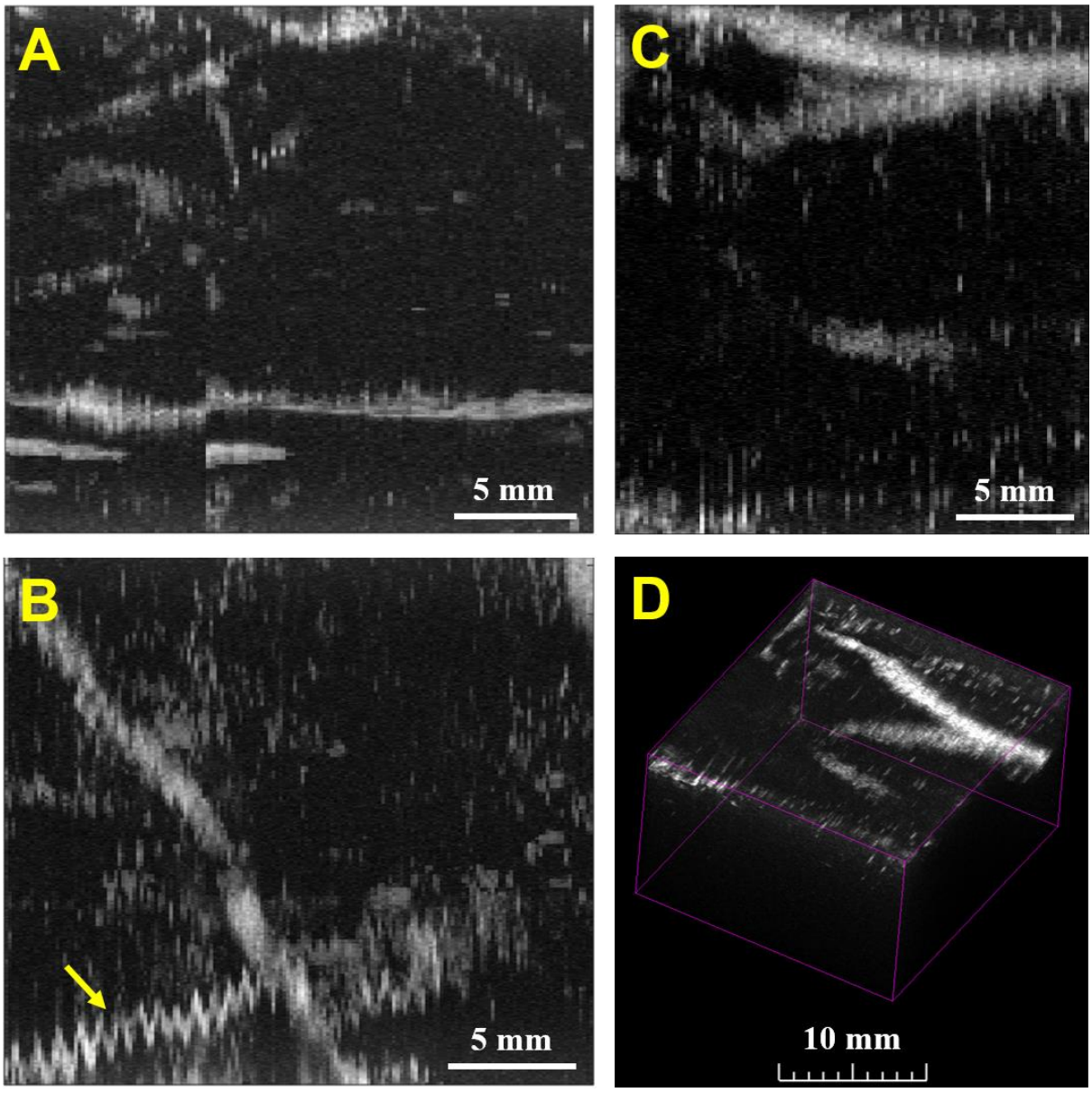

Figure 4.8 Images of vasculature around suspicious breast lesions in three patients: **A)** maximum intensity projection showing sparse, disjointed vasculature in the first patient; **B)** maximum intensity projection showing vasculature contaminated by respiratory motion (yellow arrow) in second patient; and **C)** maximum intensity projection and **D)** 3D rendering of sparse vasculature in third patient.

depth of the DFA is shallower still, due to the frequency-limited penetration of ultrasound. This effect can be seen in **Figure 4.4**, where tissue speckle is degraded at depths greater than 20 mm. Furthermore, breast composition and density can vary greatly between different women, causing the quality of high-frequency B-mode images to be reduced in some patients and leading to increased difficulty in locating the lesion for acoustic angiography. In this study, the high-

frequency stack used for B-mode imaging within the DFA had a center frequency of 18 MHz, a significantly higher frequency than those typically used for clinical imaging (1 – 10 MHz). For the future translation of acoustic angiography, lower frequencies should be explored to improve imaging depth in both DF- and B-mode.

While this may sound like a trivial solution, reducing the frequencies used for acoustic angiography will require simulations and experiments to determine optimal frequency combinations and the development of new DF transducers. In addition, the resolution of acoustic angiography is determined in part by receive frequency (29). A lower frequency will therefore lead to worse resolution, which is detrimental for the morphological analysis of vascular features in acoustic angiography images. Recently, techniques for achieving resolution beyond the acoustic diffraction limit have been published (51), including a dual-frequency, superharmonic approach, similar to acoustic angiography (86). Superharmonic ultrasound localization microscopy (ULM) uses DF imaging to isolate contrast signals, which can then be localized, tracked, and accumulated onto a super-resolution grid with advanced processing methods to form images with resolution of 20 μm (86). To date, this method has utilized a prototype DF transducer, but in the future, it can be applied on the next-generation DFA to recover resolution lost by reducing frequencies. Combining acoustic angiography with these novel post-processing methods will allow tumor vasculature to be evaluated in real-time for initial assessment (<5 minutes for an acoustic angiography volume), followed by detailed analysis of microvascular images with superior resolution from ULM.

As demonstrated in the previous clinical study using DF wobbler probes (48), respiratory motion in the breast is significantly detrimental to image quality. In particular, uncorrected motion such as that captured in **Figure 4.8B** will contaminate any attempt to quantify vessel tortuosity

and reduce the potential diagnostic power of acoustic angiography. To avoid respiratory motion, volumetric scans could be performed during a breath-hold. This approach would require a significant decrease in acquisition time – each image presented in this chapter required 1 – 3 minutes for collection, whereas a routine breath-hold is 10 – 20 seconds (71). Acquisition time with the current DFA system is limited by 1) the mechanical scanning required for volumetric images, 2) the memory and transfer speed of the system, and 3) the possible imaging frame rate (limited by microbubble circulation, acoustic time of flight, and imaging parameters). More work is needed to determine if these limitations can be addressed to perform acoustic angiography in a single breath-hold.

An alternative strategy to address motion was presented by Kierski *et al.* (86). The authors interleaved B-mode images into the DF acquisition and then employed a correlation-based speckle tracking approach to identify tissue motion and compensate in the associated DF frames (86). This method could be employed on the DFA by acquiring an additional interleaved B-mode frame for each DF frame collected using the high-frequency stack within the DFA. While this technique is computationally intensive, it has been shown to improve image quality and resolution (86). It is important to note, however, that this method is only able to correct in-plane motion; out-of-plane motion can be identified, but those frames must be discarded. Thus, a motion-corrected image can be achieved, but acquisition and processing time must be increased.

Yet another solution to the motion problem would be to use 2D DF transducers. While this strategy is the most complex and difficult to implement, it is likely the most advantageous. To date, all acoustic angiography studies have used 1D DF transducers – either a single-element wobbler probe (27,150) or a stacked linear array (141,160), such as the one used in this study. These transducers required mechanical translation to create a pseudo-3D volume comprised of a

stack of 2D images. Advances in transducer technology have led to 2D transducers, such as matrix arrays (90,162) and row-column arrays (163,164), which can acquire true volumetric images without mechanical scanning. A 2D array for acoustic angiography would allow for faster acquisition time and improved motion correction in two image planes. However, DF transducers are technically challenging to manufacture, and the development of a novel 2D DF array will require substantial simulation and experimental work to optimize for acoustic angiography. Future work will likely focus on the design and implementation of such a device.

4.5 Conclusion

In this chapter, we have presented pilot clinical data collected with a novel, stacked DFA transducer. Optimization in healthy volunteers has demonstrated that this DF system can maintain high resolution (>200 μm) and CTR (>15 dB) for acoustic angiography in humans. Early results from patients with suspicious breast lesions illuminate the remaining challenges on the path to clinical translation, including the need for even greater imaging depth, as well as methods to address physiological motion. Future studies must focus on addressing these issues and developing improved DF transducer technology for clinical acoustic angiography.

CHAPTER 5
SUPERHARMONIC BUBBLE AND TISSUE SIMULATIONS FOR DEEP DUAL-FREQUENCY IMAGING

5.1 Introduction

As discussed in the previous chapters, acoustic angiography is a contrast-enhanced ultrasound technique that allows the creation of high-resolution microvascular images in 3D (26,27,150). This technique utilizes superharmonic imaging, a method of enhancing the signal from microbubble contrast over background tissue (21,22). To do so, a low-frequency (LF) transmission is used to excite intravascular microbubbles (MBs) at the "fundamental" frequency, generating a broadband, nonlinear acoustic response that can be selectively detected with high-frequency (HF) reception (21,22). This HF receive captures the "superharmonic" frequency response of the MBs at frequencies above the 3rd harmonic, or 3rd multiple of the fundamental frequency (21,22). While MBs create a strong response at superharmonic frequencies, the signal generated by tissue at these frequencies is typically quite weak; this leads to extremely high contrast-to-tissue ratio (CTR) (21,22,24). Additionally, the high receiving frequency improves image resolution over conventional ultrasound methods (26,27).

Acoustic angiography extends superharmonic imaging into 3D by incorporating a translational motion stage to acquire volumetric image stacks (26,27,150). In this way, microvasculature can be imaged throughout a volume with little contaminating signal from the surrounding tissue. This creates an avenue for the evaluation of microvascular architecture in diseases where vascular structure is altered, such as cancer (3,165). Preclinical studies have established that acoustic angiography is a notable tool for assessing microvascular characteristics as a means of detecting malignancy (34,35,37) and monitoring treatment (38–40).

However, all superharmonic imaging techniques, including acoustic angiography, require transducers that can operate at >100% bandwidth. Due to the inherent frequency limitations of piezoelectric technology, transducers containing independent transmit and receive elements are commonly used to accomplish the necessary bandwidth. Many different transducer designs have been proposed and implemented to that end, including dual-frequency (DF) stacked arrays (141,160), interleaved arrays (21,23,24), co-linear arrays (86,145,146), and confocal single elements (26,27,166).

Most of the preclinical acoustic angiography works published to date have used a DF transducer comprised of two individual elements that were confocally aligned on a mechanical arm, or "wobbler" (26,27,34,35,37). The central element, centered at 25 – 30 MHz, was outfitted with a 2 – 4 MHz annular element (26,27). This configuration enabled coaxial superharmonic imaging in 2D with mechanical steering of the wobbler. Based on the promising preclinical results obtained with such wobbler devices, acoustic angiography was used in a pilot clinical study to image vasculature in breast tumors (48). The study revealed that the DF wobblers could resolve 200 μm vessels in humans, but they suffered from low sensitivity to contrast at clinical doses and limited depth (<2 cm) due to the focused single elements and high receive frequency (48).

Recently, a first-of-its-kind, coaxially stacked DF array has been developed for acoustic angiography (141,160), as described in Chapter 3. This novel transducer contained a 32-element LF linear array stacked behind a 256-element HF array for coaxial superharmonic imaging with 2 MHz transmit and 18 MHz receive. With this device, high resolution was maintained, while depth-of-field and sensitivity were enhanced by the array design (160). However, imaging depth was still limited (<3 cm) due to the array geometry and lensing (160), and early results from a pilot study using this device (Chapter 4) show that acoustic angiography is not yet optimized for clinical translation, largely due to the limitations of existing DF transducer technology.

The greatest limiting factor for the DF transducers described above was that their designs were determined by existing transducer technology that could be feasibly modified to perform superharmonic imaging. Because these devices originated from preclinical HF technology, it is understandable that they struggled to maintain image quality in clinically relevant scenarios. This raises the question: how can DF transducer design be informed for improved clinical acoustic angiography? More insight is necessary into how acoustic parameters affect superharmonic imaging.

Our group has studied many of the parameters pertinent to acoustic angiography in prior studies, including pulse shape (30), microbubble composition (167), and transmit and receive frequency combinations (29). In (29), the authors used single-element pistons to test which frequency combinations provided maximum CTR, finding that a 1.5 MHz transmit at MI = 1.0 paired with a 10 MHz receive gave the highest CTR. While this work provides some guidance on choosing frequencies for acoustic angiography, it did not consider imaging depth as a variable. For clinical applications in the breast, kidney, and liver, imaging depth must reach up to 8 cm. At such depth, tissue can begin to exhibit nonlinear behavior due to nonlinear propagation (17), which can

lead to contamination of superharmonic bubble signals and thus reduced CTR. In addition, this effect is amplitude dependent (168). Hence, imaging depth and excitation pressure must be included in any evaluation of acoustic parameters for superharmonic imaging at clinically relevant depths.

Because DF transducer technology is limited in availability, these parameters cannot be readily evaluated through *in vitro* or *in vivo* experiments. Instead, in this chapter, we present a set of custom simulations for assessing superharmonic image quality (in terms of CTR) as a function of transmit frequency, excitation pressure, receive bandwidth, and imaging depth. Simulated transmit pressure fields are propagated with a custom angular spectrum method with a flux-conservative Rusanov scheme to solve the nonlinearity, while microbubble dynamics are simulated with the Marmottant model. An *in silico* CTR metric is computed for each parameter set based on the simulated tissue and microbubble responses, and an optimal parameter combination is identified for each imaging depth. **Figure 5.1** provides a simplified overview of the simulations developed in this work.

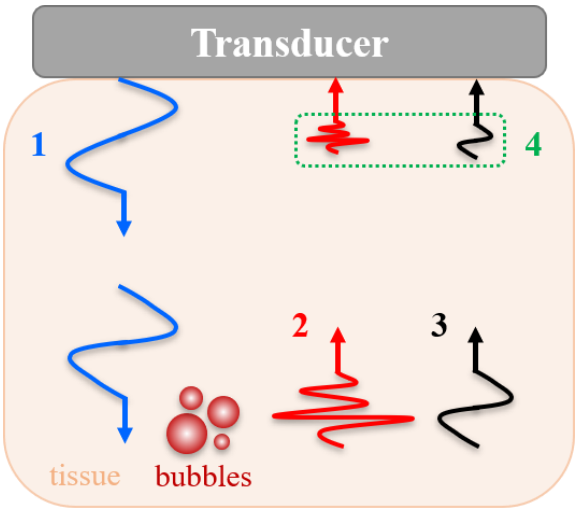

Figure 5.1 Schematic depiction of the generalized simulation procedure: 1) Transmit waveform propagates forward in angular spectrum until reaching focal depth. 2) Response scattered from polydisperse bubbles is computed using the Marmottant model with a size integration technique and propagates back to transducer. 3) Tissue response is generated and propagates back to transducer. 4) Attenuation is applied, and CTR is computed inside the receive bandwidth.

5.2 Materials and Methods

5.2.1 Custom Angular Spectrum Method

Acoustic propagation was described in 3D and included the effects of nonlinearity and attenuation. The propagation equations were solved numerically using the angular spectrum approach in combination with a Rusanov method for flux-conservative shock propagation. The acoustic pressure can be defined by a pseudo-potential, ϕ, which has advantages for the continuity through shocks (169,170):

$$p(\vec{x}) = \frac{\partial \phi}{\partial t}(\vec{x}), \qquad \textbf{Eq. 5.1}$$

where p is the acoustic pressure. Wave propagation is described in retarded time, $\tau = t - x/\overline{c_0}$, which represents a time frame moving with the mean sound speed, $\overline{c_0}$, in the x-direction. The wave propagation equation can then be written as

$$\frac{\partial \phi}{\partial x}(\vec{x}, \tau) = D\phi(\vec{x}, \tau) + N\phi(\vec{x}, \tau) + A\phi(\vec{x}, \tau). \qquad \textbf{Eq. 5.2}$$

The operator, *D*, describes diffraction:

$$D\phi(\vec{x}, \tau) = \frac{\overline{c_0}}{2} \int_{-\infty}^{\tau} \left(\frac{\partial^2 \phi}{\partial x^2} + \frac{\partial^2 \phi}{\partial y^2} + \frac{\partial^2 \phi}{\partial z^2} \right) dt \, . \qquad \textbf{Eq. 5.3}$$

Thus, the equation $\frac{\partial \phi}{\partial x}(\vec{x}, \tau) = D\phi(\vec{x}, \tau)$ is the 3D wave equation in a constant speed of sound medium with no attenuation in a reference frame that moves with the wave in the x-direction. The nonlinear operator, *N*, describes quadratic nonlinearity:

$$N\phi(\vec{x}, \tau) = \frac{\beta}{2\overline{\rho c_0}^3} \left(\frac{\partial \phi}{\partial t} \right)^2. \qquad \textbf{Eq. 5.4}$$

The attenuation operator, *A*, describes empirical attenuation and dispersion laws in the frequency domain that follow the Kramers-Kronig causality relations (171), which allows for a more flexible and accurate representation of the various power law attenuations that are observed in different

soft tissues. The implementation of this attenuation and dispersion is performed numerically in the Fourier domain using a filtering approach (172).

The numerical solutions of these equations are based on a second order Strang splitting (173), as shown below:

$$\phi(x+\Delta x,y,z,\tau)=\phi^{N}_{\frac{\Delta x}{2}}\circ\phi^{D}_{\frac{\Delta x}{2}}\circ\phi^{A}_{\Delta x}\circ\phi^{D}_{\frac{\Delta x}{2}}\circ\phi^{N}_{\frac{\Delta x}{2}}\circ(x,y,z,\tau)+\mathcal{O}(\Delta x^{2}), \qquad \textbf{Eq. 5.5}$$

which allows each term to be solved using largely independent numerical methods. The diffraction term is solved using the angular spectrum, the nonlinear term is solved using a flux-conservative Rusanov approach (174), and the attenuation and dispersion is solved empirically as a Fourier domain filter (172). For convenience, this is referred to as the "ASR" simulation from this point forward.

The transmit parameters tested included: transmit frequencies of 0.5, 1, 2, 3, and 4 MHz; transmit pressures between 125 – 1000 kPa in 125 kPa increments; and depths of 2 – 8 cm in 2 cm increments. **Figure 5.2** shows an example from the ASR simulation for a 1 MHz, 750 kPa transmission that was propagated with ASR to a focal depth of 4 cm.

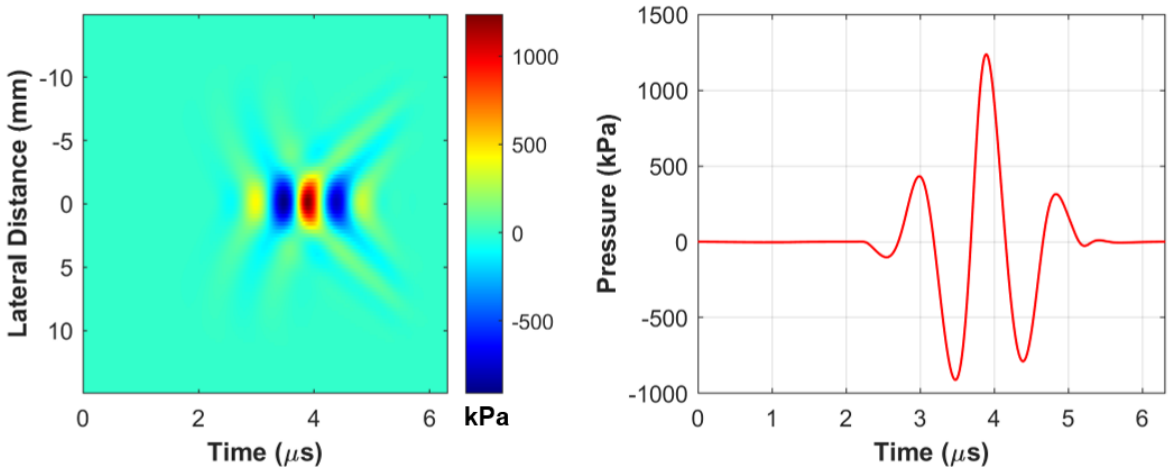

Figure 5.2 Example transmit simulation generated with angular spectrum: transmit plane after focusing (left) and focal pressure from the transmit plane (right) used as driving pressure for the Marmottant model. This example is a 1 MHz waveform propagated to 4 cm depth.

5.2.2 Marmottant Model for Microbubble Simulation

The Marmottant model of lipid-encapsulated bubble dynamics was implemented in MATLAB (Mathworks, Inc., Natick, MA, USA) (175). This is one of several models proposed for microbubble modeling, and prior publications have demonstrated that it is fairly accurate for large-amplitude oscillations of lipid microbubbles (144,175,176). This model was designed to simulate nonlinear microbubble behaviors, such as compression-only oscillations and subharmonic emissions (175,177), making it a good candidate for superharmonic simulations. The Marmottant equation is given by (1) below:

$$R\ddot{R} + \frac{3}{2}\dot{R}^2 = \frac{1}{\rho}\left[\left(P_0 + \frac{2\sigma(R_0)}{R_0}\right)\left(\frac{R_0}{R}\right)^{3\gamma}\left(1 - \frac{3\gamma\dot{R}}{c}\right) - \frac{2\sigma(R)}{R} - \frac{4\mu\dot{R}}{R} - \frac{4\kappa_s\dot{R}}{R^2} - P_0 - P_{ac}(t)\right] \quad \textbf{Eq. 5.6}$$

Here, R, $\dot{R}$, and $\ddot{R}$ are the radius, wall velocity, and wall acceleration, respectively. **Table 5.1** defines all other variables in equation **5.6**. Bubble parameters were chosen to represent the commercial contrast agent, DEFINITY (Lantheus Medical Imaging, N. Billerica, MA, USA) (114), based on previously published works (178,179). In equation **5.6**, *σ(R)* is defined by

$$\sigma(R) = \begin{cases} 0, \ if\ R < R_{buckling} \\ \chi\left(\frac{R^2}{{R_{buckling}}^2} - 1\right), \ if\ R_{buckling} \le R \le R_{break-up}. \\ \sigma_w, \ if\ ruptured\ \&\ R > R_{ruptured} \end{cases} \quad \textbf{Eq. 5.7}$$

Below a certain radius, the shell buckles, and surface tension falls to zero. Conversely, the shell can rupture, creating gaps in the lipid monolayer and leading to surface tension equal to the surrounding medium (*e.g.*, water). In a small range of radii near the initial radius of the bubble, however, the shell behaves in an elastic manner. The three regimes created by this definition — buckled, elastic, and ruptured — allow simulation of the dynamic nonlinear behavior of a lipid-shelled bubble with this model (175). To define *σ(R)*, we must first define the critical radii of the bubble.

The buckling radius is defined by

$$R_{buckling} = R_0\sqrt{\frac{\sigma(R_0)}{\chi} + 1}. \quad \textbf{Eq. 5.8}$$

In this work, this definition leads to $R_{buckling} \approx 0.98R_0$. The ruptured radius is then given by

$$R_{ruptured} = R_{buckling}\sqrt{\frac{\sigma_w}{\chi} + 1}, \quad \textbf{Eq. 5.9}$$

which gives $R_{ruptured} \approx 1.02R_0$. Perhaps the most important definition in this model is that of $R_{break\text{-}up}$, which determines the extent of the elastic regime. This parameter is defined by:

$$R_{break-up} = R_{buckling}\sqrt{\frac{\sigma_{break-up}}{\chi} + 1}. \quad \textbf{Eq. 5.10}$$

Importantly, $\sigma_{break\text{-}up}$, the critical tension at which the shell breaks, is unknown. For lipid-shelled microbubbles, previous studies have used $R_{break\text{-}up}$ values ranging from $R_{ruptured}$ to $1.5R_0$ (144,175–177). In this work, we chose a conservative definition of $R_{break\text{-}up} = R_{ruptured}$.

To confirm that this implementation of the Marmottant model is accurate and that the parameters are appropriately defined, relative expansion was measured for a subset of simulations. Relative expansion is equal to the measured maximum bubble radius divided by the initial radius (R_{max}/R_0) and is commonly used to evaluate the oscillatory behavior of microbubbles (134,176,180). **Figure 5.3** shows relative expansion measured for two excitation frequencies (2 and 4 MHz) for a range of bubble radii and excitation pressures. Comparing these measurements to the results from King and O'Brien (176), we find excellent agreement with our implementation of the Marmottant model in the corresponding range of pressure and radii (denoted by the cyan boxes).

For each transmit frequency and pressure, the driving pressure, $P_{ac}(t)$, was defined as the A-line from the focus of the ASR simulation. A built-in variable-step ordinary differential equation solver (ode45, MATLAB, Mathworks, Inc., Natick, MA, USA) was used to obtain solutions for

the bubble radius, wall velocity, and wall acceleration. The scattered pressure, called P_{bubble}, was calculated with the following equation,

$$P_{bubble}(t) = \frac{\rho}{r}\left(R^2\ddot{R} + 2R\dot{R}^2\right), \qquad \textbf{Eq. 5.11}$$

where r is the distance from the bubble at which the pressure is scattered (144,177,181). After calculation, the scattered pressure was interpolated to a uniform sampling frequency of 200 MHz to match the transmit simulations.

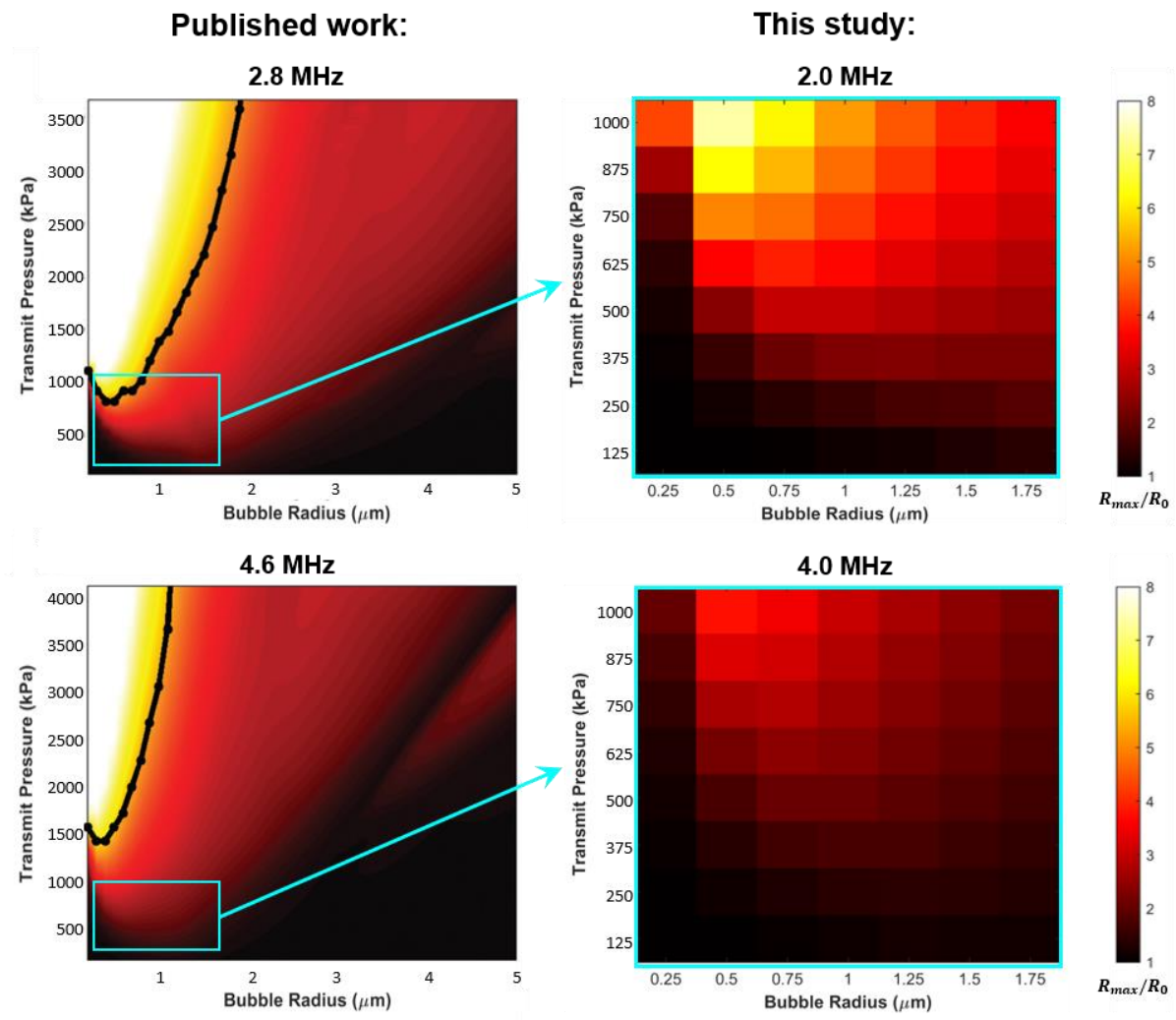

Figure 5.3 Relative expansion computed with the Marmottant model from King and O'Brien compared to the present study. The cyan boxes represent the approximate range of pressure and bubble radii simulated in this chapter. All images are displayed on the same scale. Left panels: © 2011 Acoustical Society of America. Reprinted, with permission, from King and O'Brien, "Comparison between maximum radial expansion of ultrasound contrast agents and experimental postexcitation signal results," *JASA*, 2011.

Table 5.1: Marmottant model parameters.

Symbol	Quantity	Value
ρ	medium density	1000 kg/m^3
P_0	ambient pressure in Chapel Hill, NC	99562 Pa
R_0	initial bubble radius	0.3 – 1.5 μm
$\sigma(R_0)$	initial shell surface tension	0.04 N/m
γ	adiabatic polytropic gas exponent	1.06
c	speed of sound	1540 m/s
μ	dynamic medium viscosity	0.001 Pa·s
κ_s	shell surface viscosity	6×10^{-9} kg/s
χ	shell surface elasticity	0.81 N/m
σ_w	medium surface tension	0.073 N/m
$\sigma_{break\text{-}up}$	shell break-up surface tension	0.074 N/m
$R_{break\text{-}up}$	shell break-up radius	$1.02R_0$

5.2.3 Contrast-to-Tissue Ratio Calculation

Because tissue scattering is predominantly linear compared to microbubble scattering, the pressure scattered from tissue was defined as

$$P_{tissue}(t) = P_{ac}(t)/2000. \quad \textbf{Eq. 5.12}$$

This definition assumes that the tissue linearly scatters the incident wave with a relative brightness of -66 dB. With this assumption, computationally intensive backpropagation can be avoided, while nonlinearities arising from nonlinear propagation of the transmit wave in the forward direction are maintained in the tissue response. It should also be noted that this assumption allows these simulations to be tuned to represent more or less echogenic tissues (*e.g.*, fat *vs.* muscle) for specific applications (182). The frequency spectrum, A_{tissue}, was obtained via fast Fourier transform of P_{tissue}.

To account for a polydisperse MB distribution, which would be used for clinical contrast-enhanced ultrasound imaging, MBs were simulated with radii between 0.3 – 1.5 μm, and the resulting scattered pressures were combined with a size integration technique (144,183) based on the size distribution of DEFINITY, as measured by a single particle optical sizing device

(Accusizer, 780A, Particle Sizing Systems, Santa Barbara, CA, USA). Briefly, the size integration technique (183) operates in the frequency domain to combine the pressures scattered by single bubbles into the total pressure scattered by a population of polydisperse MBs:

$$A_{total}(f) = \sum_{n=i}^{j} A_{bubble}(R_{0,n}, f)\, W_n. \quad \textbf{Eq. 5.13}$$

Here, $A_{bubble}(R_{0,n},f)$ is the frequency spectrum of the scattered pressure for a MB with initial radius R_0 as defined by equation **5.11**, W_n is the percentage weight of MBs of size n in the distribution, and $A_{total}(f)$ is the representative frequency spectrum of the MB population. A histogram of the DEFINITY distribution used for size integration is shown in **Figure 5.4**. The radii simulated here (0.3 – 1.5 μm) accounted for 99% of MBs in the native DEFINITY distribution.

Once A_{total} and A_{tissue} were obtained, a frequency domain attenuation filter was applied to account for attenuation in the backward direction. A value of 0.3 dB/cm/MHz was used to represent average soft tissue attenuation. The attenuated frequency spectra were then converted back to the time domain and filtered by a digital Kaiser window for a given receive bandwidth. Random, normally distributed white noise ($0.05 < \sigma < 2$) was then added to both bubble and tissue responses before envelope-detection with the Hilbert transform. The final contrast-to-tissue ratio (*CTR*) metric was defined as

$$CTR = 20 \log_{10}\left(\frac{E_{total,max}}{E_{tissue,max}}\right), \quad \textbf{Eq. 5.14}$$

where $E_{total,max}$ and $E_{tissue,max}$ represent the maxima of the envelope-detected, receive-filtered scattered pressures for the polydisperse bubbles and tissue, respectively. For each set of transmit parameters, the CTR calculation was repeated and averaged over 500 independent noise realizations. Receive center frequencies were defined between 5 and 30 MHz in increments of 5 MHz, and the receive bandwidth was held constant at 10 MHz wide for all center frequencies.

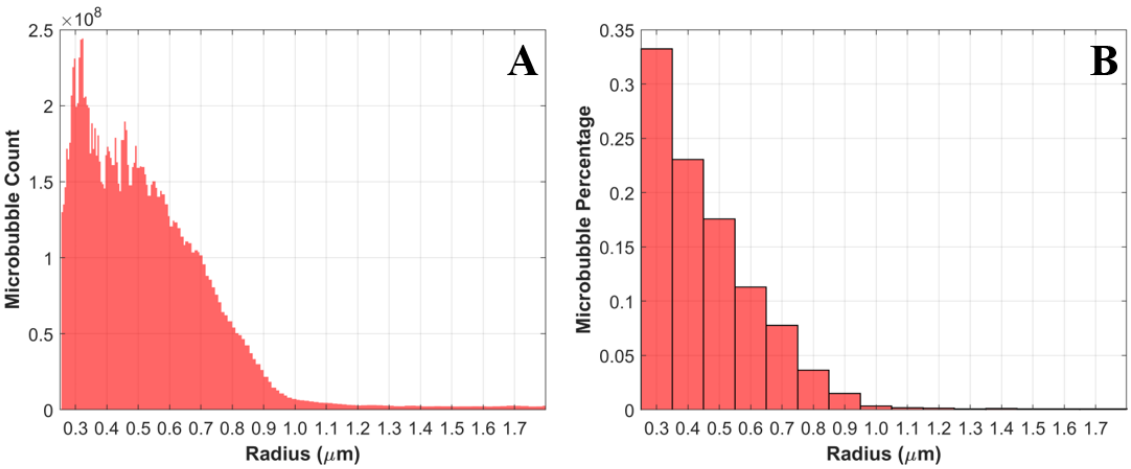

Figure 5.4 Histogram of the native DEFINITY microbubble distribution: **A)** measured count and **B)** percentage calculated for 0.1 μm bins.

5.2.4 Experimental Validation

To validate the simulation framework, an *in vitro* experiment was performed. First, a synthetic cellulose microvessel (200 μm inner diameter, Spectrum Laboratories, Rancho Dominguez, CA, USA) was embedded in a tissue-mimicking graphite-gelatin phantom (attenuation = 0.3 dB/cm/MHz) at a depth of 2 cm. DEFINITY MBs (114) were diluted to a concentration of 1 x 10^6 MBs/mL and infused through the microvessel at a volume flow rate of 30 μL/min using a syringe pump (Pump 11 Elite, Harvard Apparatus, Holliston, MA, USA).

For MB and tissue excitation, annular LF pistons (Olympus Scientific Solutions, Waltham, MA, USA) were used to transmit at 1 – 2 MHz center frequency with an arbitrary waveform generator (AFG3101, Tektronix, Inc., Beaverton, OR, USA) and power amplifier (240L, Electronics & Innovation, Ltd., Rochester, NY, USA). Several confocal HF pistons with center frequencies between 10 – 20 MHz (Olympus Scientific Solutions, Waltham, MA, USA) were paired with the LF pistons for superharmonic reception. For each frequency combination, the HF piston was connected to a receive amplifier (Ritec, Inc., Warwick, RI, USA) and radiofrequency (RF) data was recorded through a 12-bit digitizer (CSE1222, DynamicSignals LLC, Lockport, IL,

USA) controlled by a custom acquisition program (LabVIEW, National Instruments Corp., Austin, TX, USA).

For each frequency combination, RF data were recorded while MBs were flowing in the microvessel to measure the superharmonic bubble response. For the tissue response, RF data were collected from a location 5 mm away from the microvessel at the same depth in the phantom. These data were used to compute an *in vitro* CTR metric using the same methods described for the *in silico* data in Section 5.2.3, with the addition of a bandpass filter with cutoffs at 0.5 and 45 MHz to remove excess noise from the experimental data before CTR calculation. The resulting *in vitro* CTR values were compared to the simulation results from 2 cm depth as validation.

5.3 Results and Discussion

5.3.1 Experimental Validation

First, a subset of the simulation results was compared to *in vitro* experimental data to evaluate the simulation's capability to accurately predict CTR at 2 cm depth. Comparing *in vitro* and *in silico* data for 1 MHz transmit frequency, we find that the simulation accurately predicts the receive frequency that maximizes CTR **(Figure 5.5A)**. In both simulation and experiment, a receive frequency of 10 MHz provided the highest CTR value for 1 MHz transmit; in this case, simulation predicted 34.8 dB, while 25.9 dB was obtained experimentally. For 2 MHz transmit frequency (**Figure 5.5B**), simulation and experiment show good agreement for 15 MHz receive (28.1 dB *vs.* 23.7 dB, respectively). However, the simulated results predict maximum CTR at 20 MHz receive, while the experimental data shows the highest CTR at 15 MHz.

In both cases, as a function of transmit pressure, the experimental data exhibit a smooth increasing trend that appears to reach an asymptote at higher pressures. In comparison, the

simulated results display an unclear "jagged" trend with respect to pressure. There could be many possible factors contributing to this trend. First, this could potentially be an effect of downsampling the solutions of the Marmottant model, which were initially computed with a variable step. In addition, the results of the Marmottant simulation are inherently dependent on both the solver used to obtain the solution (in this case, *ode45* in MATLAB), as well as the bubble shell parameters defined in the model. In particular, the values defined for $\sigma_{break\text{-}up}$ and $R_{break\text{-}up}$ determine the extent of the nonlinear elastic regime in the model and therefore the nonlinear signal produced by the bubble. For the simulation results to recapitulate the exact trends observed *in vitro*, these parameters must be determined by curve fitting bubble behavior from high-speed optical data. As such, from the results of this study, we will identify a pressure threshold above which CTR will be maximized, rather than a single pressure that maximizes CTR.

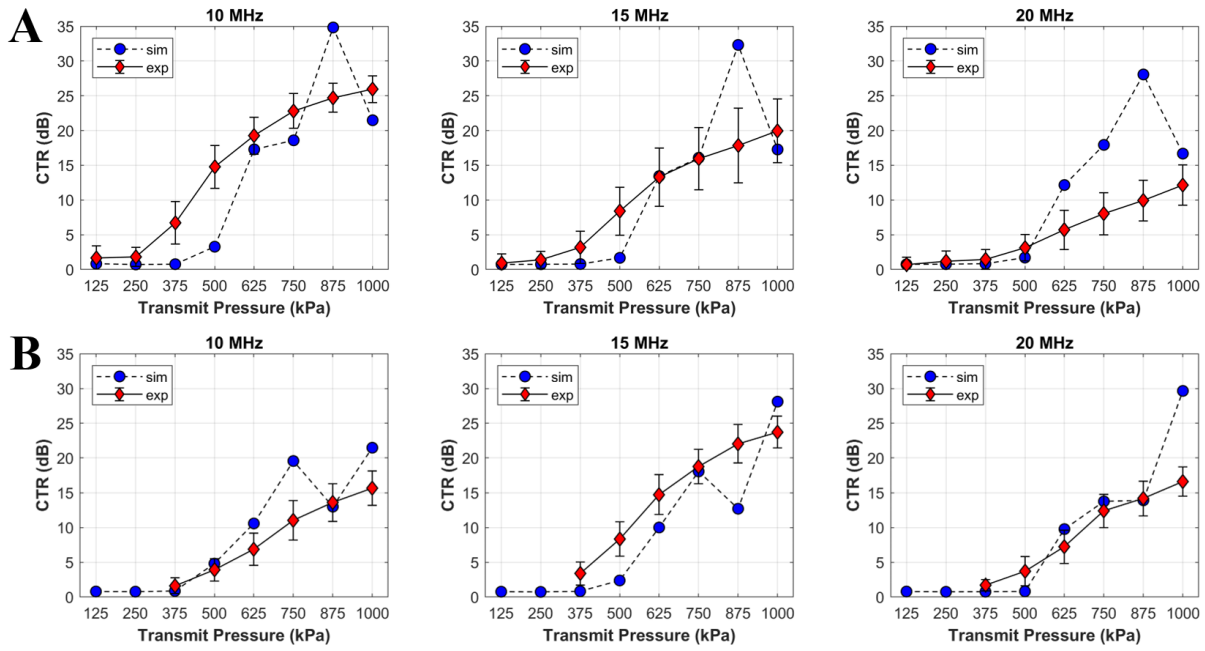

Figure 5.5 Comparison of simulated and experimental results: **A)** transmit at 1 MHz and **B)** 2 MHz with 10 MHz receive (left), 15 MHz receive (center), and 20 MHz receive (right). Experimental data are presented as mean ± standard deviation.

5.3.2 Superharmonic Simulations at 2 – 4 cm

At a depth of 2 cm, CTR increased as transmit frequency decreased, regardless of transmit pressure or receive frequency (**Figure 5.6**). Maximum CTR was obtained for 0.5 MHz transmit paired with a receive frequency of 5 MHz. For all transmit frequencies, the receive frequency that

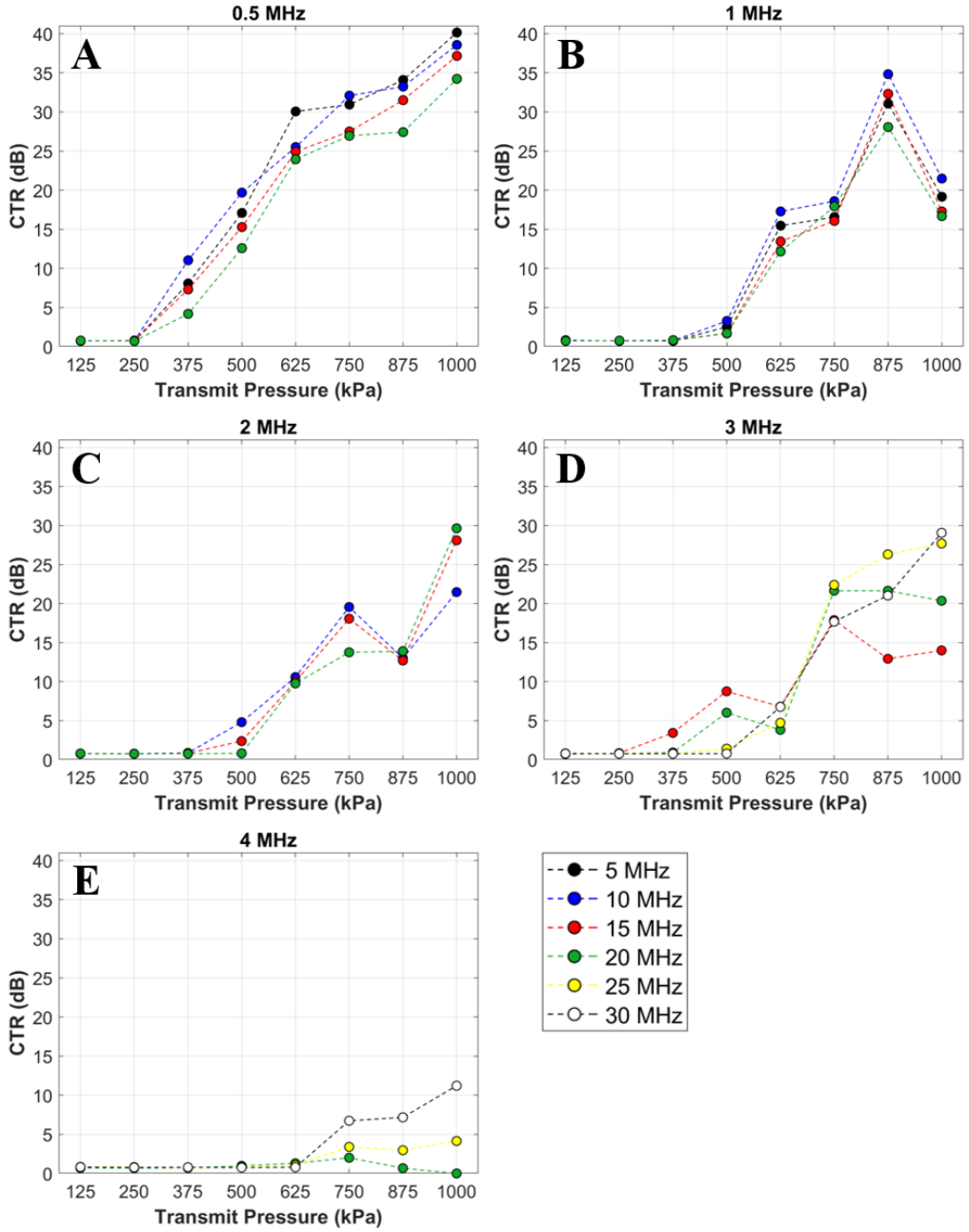

Figure 5.6 Simulation results at 2 cm depth: transmit at **A)** 0.5 MHz, **B)** 1 MHz, **C)** 2 MHz, **D)** 3 MHz, and **E)** 4 MHz.

provided the highest CTR was the 8^{th} – 10^{th} harmonic frequency, and CTR was maximized at a transmit pressure greater than 625 kPa.

Simulation results for an imaging depth of 4 cm show that maximum CTR is obtained with a transmit frequency of 0.5 MHz and a receive frequency of 5 MHz (**Figure 5.7**). For the higher transmit frequencies, CTR decreased steeply compared to the results from 2 cm. At 4 MHz transmit, CTR never surpassed 1 dB at any transmit pressure or receive frequency. As observed at 2 cm depth, optimal receive frequency tended toward the 8^{th} – 10^{th} harmonic, and pressure above 625 kPa led to the greatest CTR.

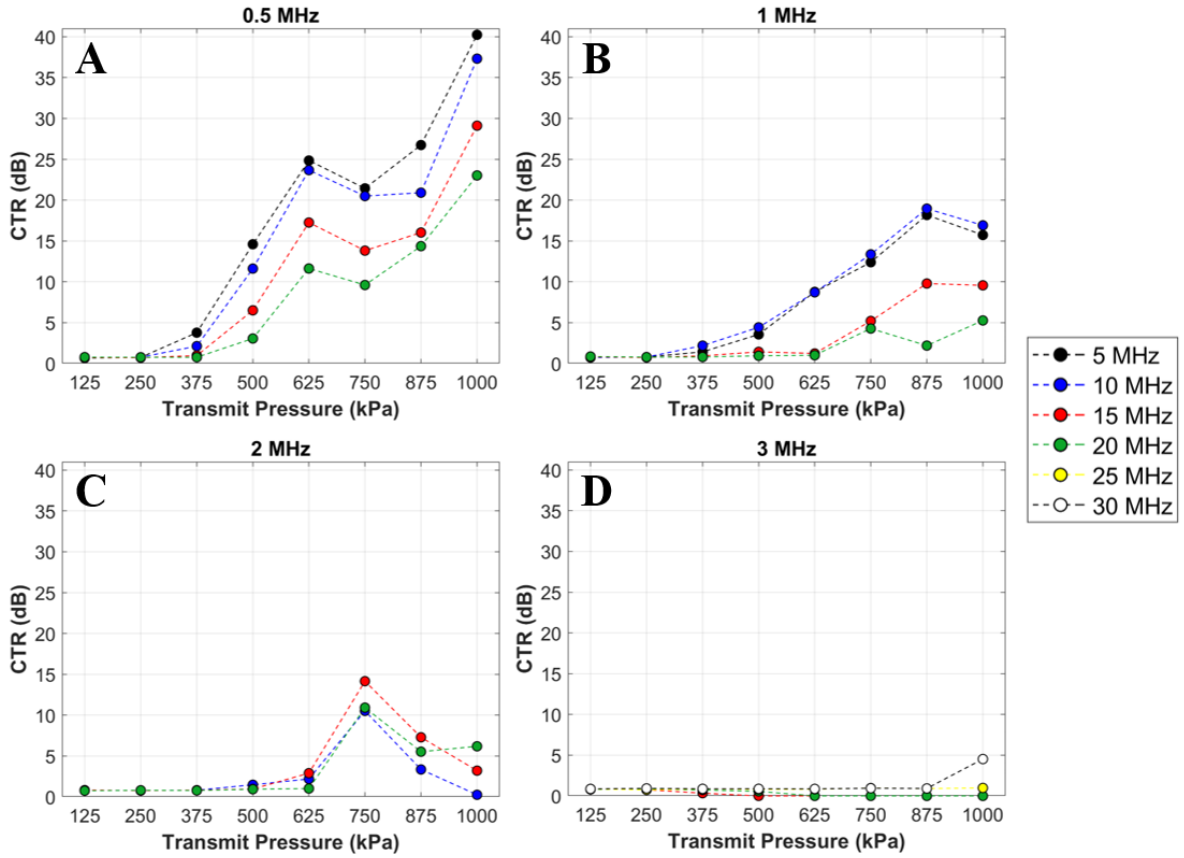

Figure 5.7 Simulation results at 4 cm depth: transmit at **A)** 0.5 MHz, **B)** 1 MHz, **C)** 2 MHz, and **D)** 3 MHz. For higher transmit frequencies, CTR < 1 dB.

5.3.3 Superharmonic Simulations at 6 – 8 cm

The CTR trends observed at shallower imaging depths are also exhibited for 6 – 8 cm depth. At both 6 and 8 cm, the highest CTR is again shown for transmit frequency of 0.5 MHz paired with a receive frequency of 5 MHz (**Figures 5.8** and **5.9**). As expected, due to attenuation, the maximum possible CTR decreases as imaging depth increases (maximum CTR = ~40 dB at 2 cm *vs.* ~20 dB at 8 cm). At these greater depths, the higher transmit frequencies are not able to achieve CTR above 1 dB for any of the pressures or receive frequencies tested. Receiving at the 10^{th} harmonic (5 MHz paired with 0.5 MHz transmit or 10 MHz paired with 1 MHz transmit) produced the greatest CTR.

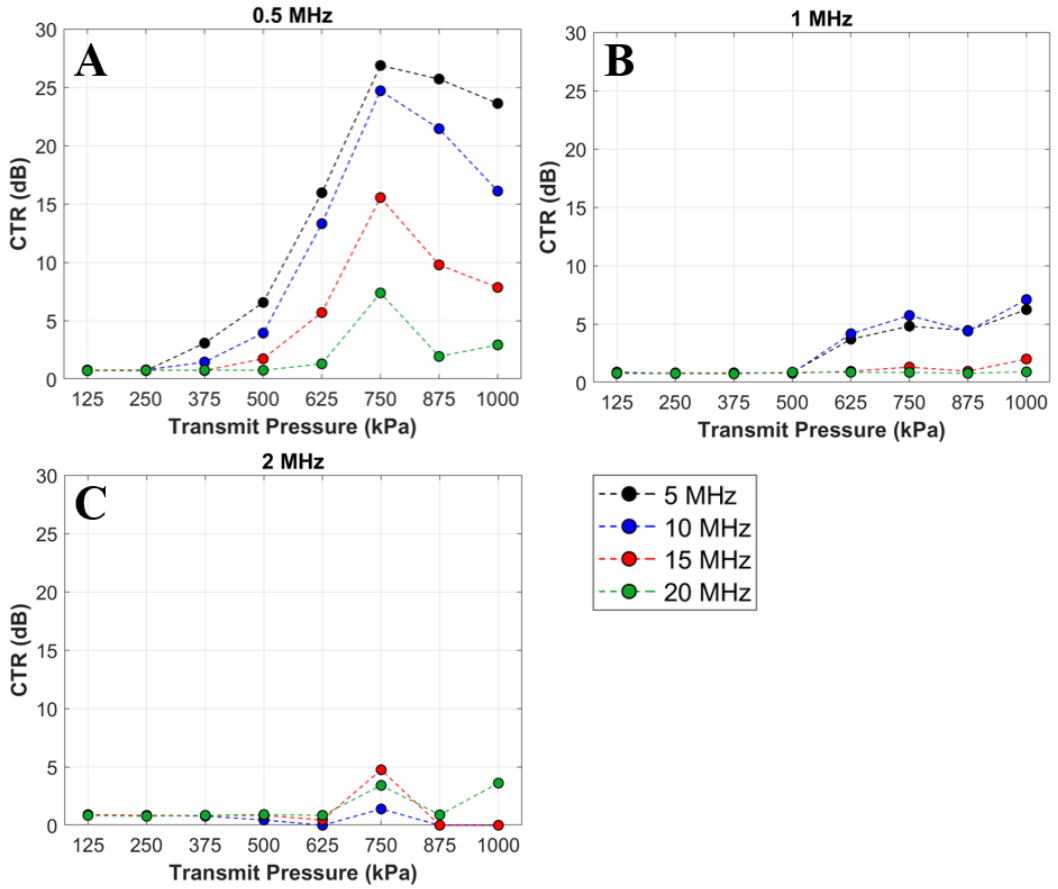

Figure 5.8 Simulation results at 6 cm depth: transmit at **A)** 0.5 MHz, **B)** 1 MHz, and **C)** 2 MHz. For higher transmit frequencies, CTR < 1 dB.

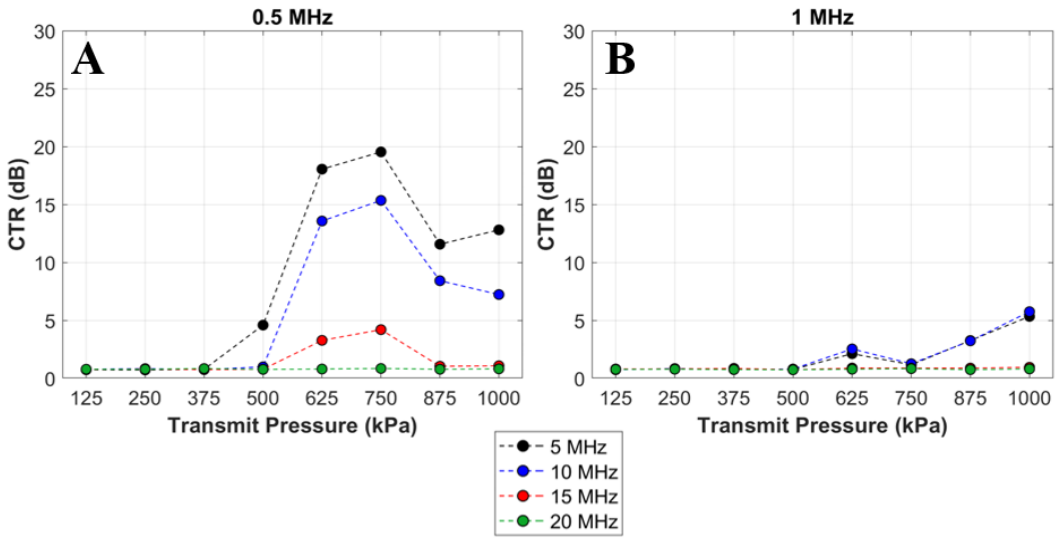

Figure 5.9 Simulation results at 8 cm depth: transmit at **A)** 0.5 MHz and **B)** 1 MHz. For higher transmit frequencies, CTR < 1 dB.

5.3.4 Role of Mechanical Index in Superharmonic Imaging

While the highest CTR was predicted for a transmit frequency of 0.5 MHz, it is important to consider these results in the context of mechanical index (MI), as well as pressure. MI is a metric of acoustic power used to indicate the possibility of mechanical bioeffects (*e.g.*, cavitation) caused by ultrasound (9) and is defined as the peak negative pressure in MPa divided by the excitation frequency in MHz. The United States Food and Drug Administration (FDA) limits MI to 1.9 for diagnostic ultrasound, but many commercial contrast agent manufacturers recommend even lower MI values to reduce the possibility of adverse effects caused by microbubble destruction. The maximum MI recommended for DEFINITY bubbles is 0.8, significantly lower than the FDA guideline (114).

Here, we can examine the simulation results as a function of MI to determine what frequency provides the maximum CTR at a pressure considered safe for superharmonic imaging with DEFINITY contrast. At 2 cm depth, a transmit frequency of 2 MHz or 3 MHz is optimal, providing the highest CTR below MI = 0.8 (**Figure 5.10A**). We can observe that the simulation

result for 2 MHz transmit paired with 20 MHz receive agrees well with existing data from the dual-frequency array (transmit/receive at 2/18 MHz) described in Chapters 3 and 4 (160). When imaging depth increases to 4 or 6 cm, CTR is optimized with transmit at 0.5 MHz, with 1 MHz providing the second highest CTR (**Figure 5.10B-C**). At 8 cm, 0.5 MHz is the only transmit frequency to achieve CTR greater than 5 dB at an MI below 0.8 (**Figure 5.10D**). These results are summarized in **Table 5.2**, which identifies the optimal frequency combination for superharmonic imaging at each depth.

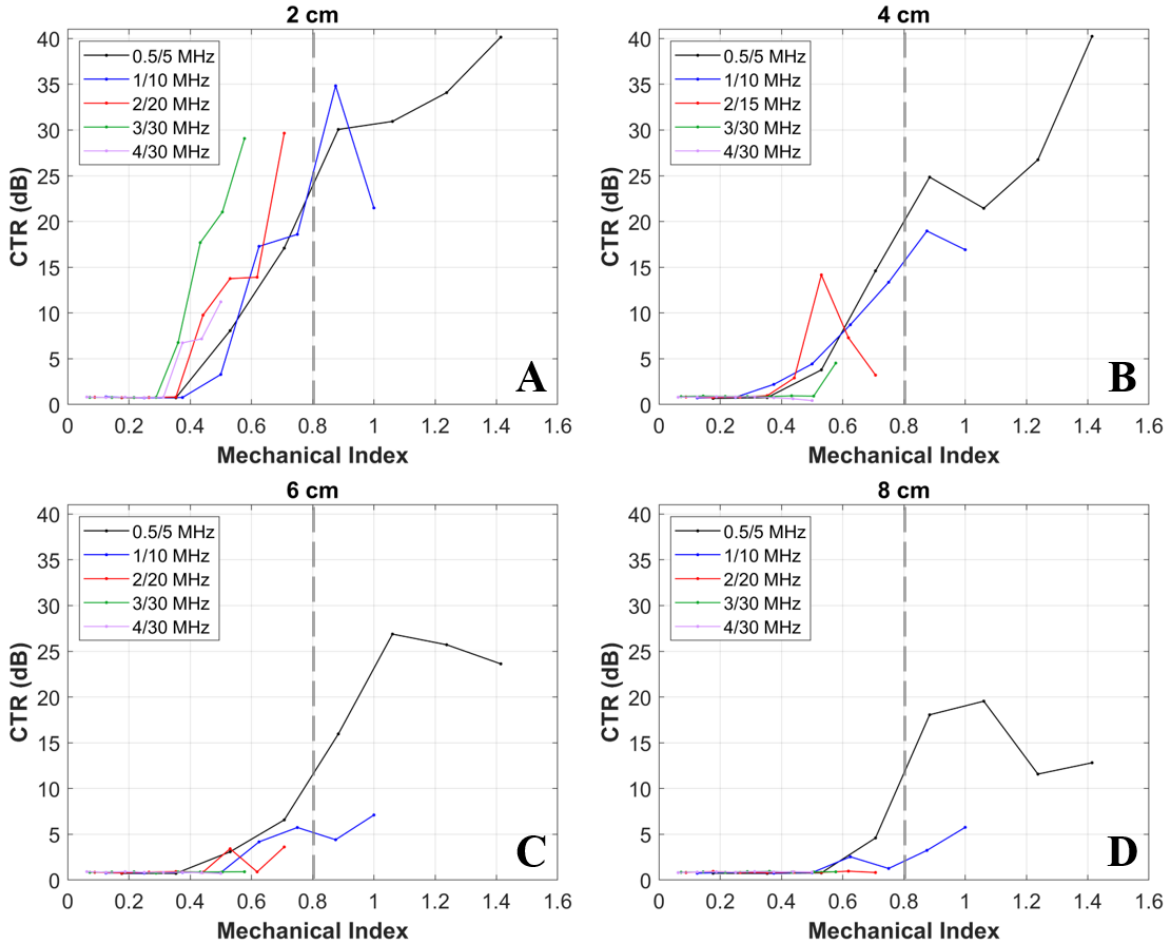

Figure 5.10 Comparison of transmit/receive frequency combinations that provide maximum CTR as a function of mechanical index: **A)** 2 cm, **B)** 4 cm, **C)** 6 cm, and **D)** 8 cm. The dashed line indicates MI = 0.8, the recommended maximum MI for DEFINITY contrast.

Table 5.2: Optimal frequency combinations for superharmonic imaging.

Depth	Transmit Frequency	Receive Frequency
2 cm	2 – 3 MHz	20 – 30 MHz
4 cm	0.5 – 1 MHz	5 – 10 MHz
6 cm	0.5 – 1 MHz	5 – 10 MHz
8 cm	0.5 MHz	5 MHz

5.4 Conclusion

In this study, we have presented a custom simulation tool for evaluating CTR as a function of imaging parameters. These results illustrate three key points for superharmonic imaging. First, lower transmit frequency leads to higher CTR. It is known that lower excitation frequencies lead to greater expansion of the MB shell, and this expansion is associated with increased broadband noise – the signal detected during superharmonic imaging (176). As shown in this chapter, lower transmit frequencies should therefore be beneficial for improved acoustic angiography. Second, higher pressure (>625 kPa) is needed to excite MBs to produce substantial superharmonic signals. This effect has been reported previously; the majority of acoustic angiography studies have been performed with a transmit pressure above 1000 kPa precisely for this reason (29,30,35). Finally, receive frequency should be chosen around the 8^{th} – 10^{th} harmonic frequency for maximum CTR. This indicates that there is an optimal location in the receive frequency range at which superharmonic bubble signals are maximally enhanced over any superharmonic signal generated by nonlinear propagation in tissue. Interestingly, the results presented herein show that this trend holds for any imaging depth between 2 and 8 cm.

From these results, we have identified optimal frequency combinations for superharmonic dual-frequency imaging at depths of 2 – 8 cm. To maintain high sensitivity for deep acoustic angiography, lower transmit frequencies (0.5 – 1 MHz) should be paired with receive frequencies around the 10^{th} harmonic of the excitation. In the future, these data will be used to inform the

design of dual-frequency transducers capable of performing clinical acoustic angiography in targets such as the breast, thyroid, and liver.

CHAPTER 6
CONCLUDING REMARKS

In this dissertation, we have presented a myriad of approaches to improve acoustic angiography as we move toward clinical translation of this microvascular ultrasound imaging technique. We have shown that superharmonic imaging is affected by both microbubble and acoustic parameters and that these parameters can be optimized to improve image sensitivity. By measuring superharmonic output from different microbubble contrast agents, we have found that microbubbles can be tuned for superharmonic imaging – specifically, perfluorocarbon-core, lipid-shelled contrast is optimal for this technique. Based on these results, DEFINITY will be the best choice to maximize sensitivity for acoustic angiography compared to other currently available FDA-approved, commercial contrast agents, such as Optison (113) or Lumason (184).

By implementing a first-of-its-kind stacked dual-frequency array, we have demonstrated that acoustic angiography can be performed up to 3 cm depth with high sensitivity to microbubble contrast at MI < 0.5. In a rodent tumor model, we have shown up to 10 mm improvement in imaging depth compared to previous wobbler transducers. In a pilot study in humans, the DFA is sensitive to sub-millimeter vessels in targets with significant physiological motion, such as the neck and breast. While these data show promising improvement over single-element devices, the clinical study presented in this dissertation serves to illustrate the significant challenges that must still be overcome for effective acoustic angiography in the clinic.

One of the greatest obstacles facing the clinical translation of acoustic angiography is the dearth of dual-frequency transducers capable of imaging at clinically relevant depths. However, dual-frequency probe design is technically challenging, and data is necessary to inform transducer design in order to avoid prohibitively costly and lengthy transducer development. To this end, we have developed a custom simulation tool for evaluating CTR as a metric of superharmonic image quality, allowing any combination of acoustic parameters and imaging depths to be tested without a physical transducer. In this dissertation, we focused on depths that are relevant for breast, thyroid, and liver imaging in the clinic (2 – 8 cm). We have shown that reducing the transmit frequency will maximize CTR for all depths, while receiving around the 8^{th} – 10^{th} harmonic is optimal. These results indicate that a transducer with transmit/receive at 0.5/5 MHz or 1/10 MHz will be optimal for deeper clinical acoustic angiography. Notably, these results can be applied to any transducer design, such as DF matrix arrays, which will open the door for true volumetric superharmonic imaging in the future.

Overall, this dissertation identifies three paths to improve acoustic angiography by tuning 1) microbubble contrast agents, 2) acoustic parameters, and 3) transducer technology. In the future, the results presented herein will be used to inform the design and implementation of clinical acoustic angiography. As superharmonic imaging technology continues to advance, we anticipate that this non-invasive microvascular ultrasound technique will lead to significant improvements in patient care and diagnosis.

APPENDIX A
DUAL-FREQUENCY ARRAY IMAGING SYSTEM

To operate the stacked dual-frequency array (DFA), an imaging system was developed using two synchronized programmable research ultrasound scanners (Vantage 256 standard and high-frequency configurations, Verasonics, Inc., Kirkland, WA, USA). Typically, programmable ultrasound scanners are used independently, but for this work, the scanners were programmed to share one system clock for phase accurate synchronization (Multi-System Synchronization Module, Verasonics, Inc., Kirkland, WA, USA), avoiding potential jitter or error introduced by traditional triggering. The scanners were housed on a portable cart (McMaster-Carr, Aurora, OH, USA) for convenient transportation between the laboratory and hospital for the preclinical and clinical studies presented in this dissertation. For 3D imaging, the DFA was mechanically translated on a linear motion stage (Velmex, Inc., Bloomfield, NY, USA) controlled by a custom program (LabVIEW, National Instruments, Austin, TX, USA) run with an external laptop computer (Dell Technologies, Round Rock, TX, USA). The motion stage was affixed to a stationary surface during imaging using a camera arm with six degrees of freedom. A photo of the system setup for clinical imaging is shown in **Figure A.1**, and a screenshot of the custom LabVIEW program is shown in **Figure A.2**.

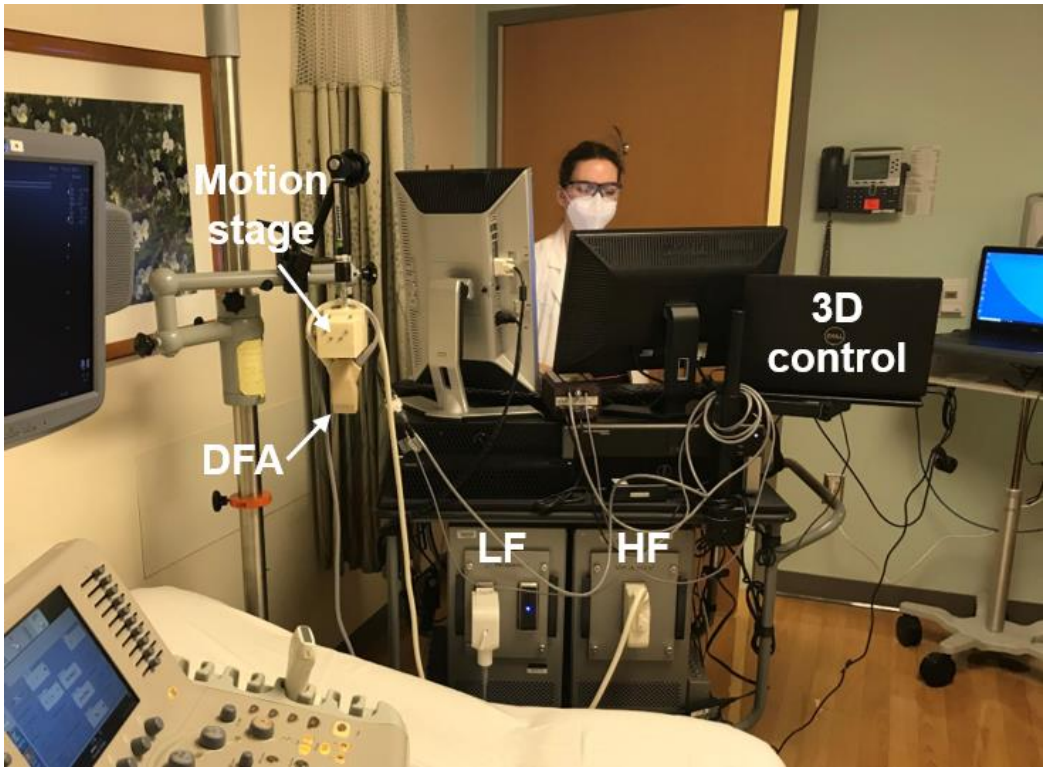

Figure A.1 Photograph of the dual-frequency array system setup for clinical imaging in the hospital. DFA = dual-frequency array, HF = high-frequency, LF = low-frequency.

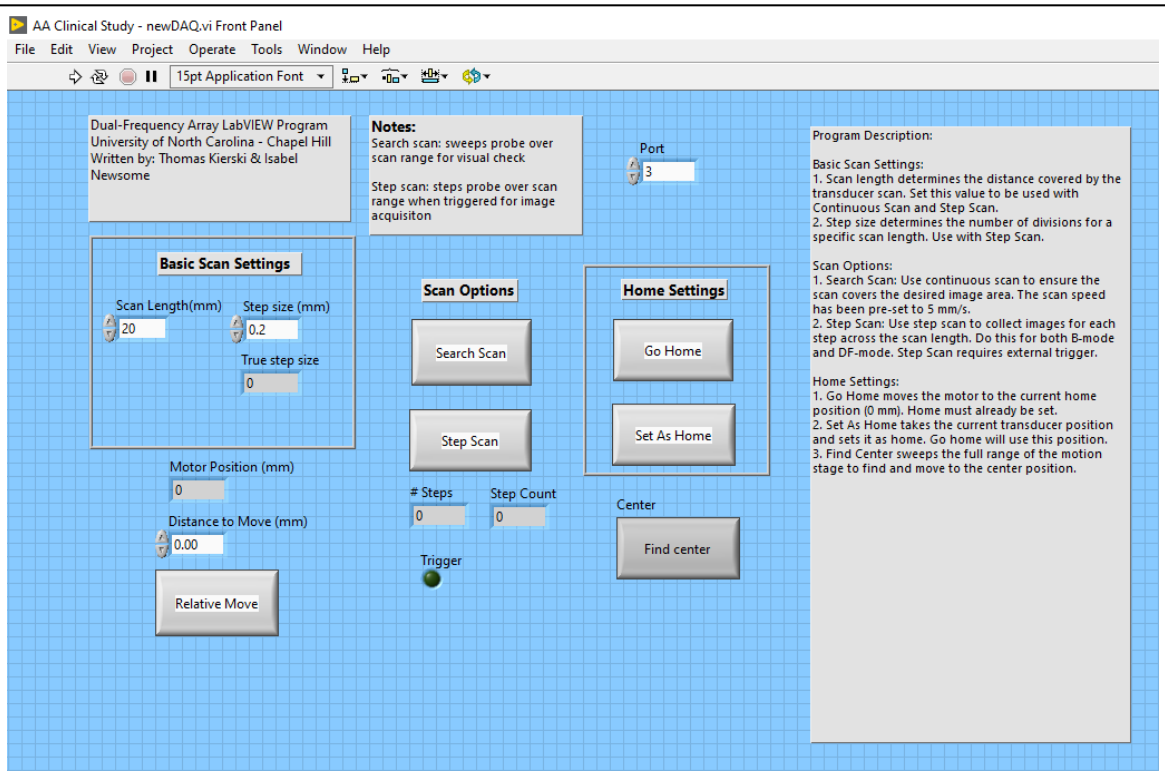

Figure A.2 Screenshot of the program for 3D acquisition with the dual-frequency array system.

APPENDIX B
ALTERNATIVE DUAL-FREQUENCY TRANSDUCERS

B.1 Parallel Transducers for Superharmonic Imaging

Recently, parallel, or co-linear, transducers have been developed for DF applications. Because these devices consist of individual transducers aligned physically to have confocal beams, they can be rapidly prototyped and assembled with fewer complications than integrated DF arrays, such as that described in this dissertation. Our group has characterized a co-linear DF probe that consists of a two-element LF "outrigger" that attaches to a commercial HF array (86,145,185), shown in **Figure B.1**, along with a pressure map of the LF beam created by this device. It has been shown that this device can be used for confocal superharmonic imaging with high signal-to-noise ratio (SNR) (145,185). A comparison of conventional nonlinear contrast imaging on a preclinical scanner (Vevo2100, VisualSonics, Inc., Toronto, ON, Canada) and superharmonic

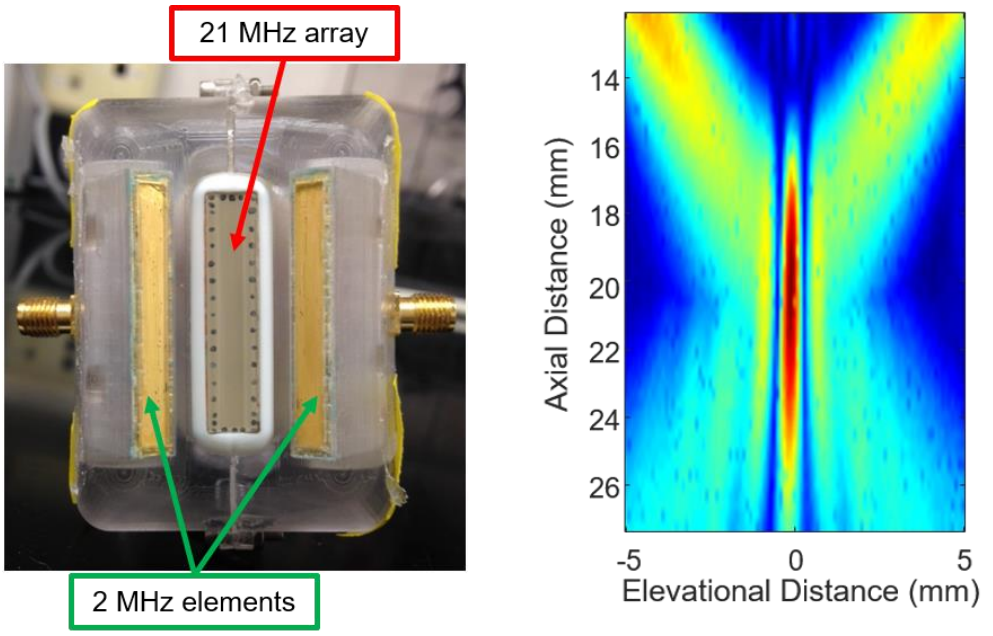

Figure B.1 Co-linear dual-frequency prototype: photograph of the transducer face (left) and pressure map of the low-frequency beam (right), where the red region represents the focal zone.

imaging with this prototype transducer found that superharmonic imaging provides at least 12 dB increase in contrast enhancement, illustrating this technique's ability to detect contrast without contamination from background tissue (**Figure B.2**).

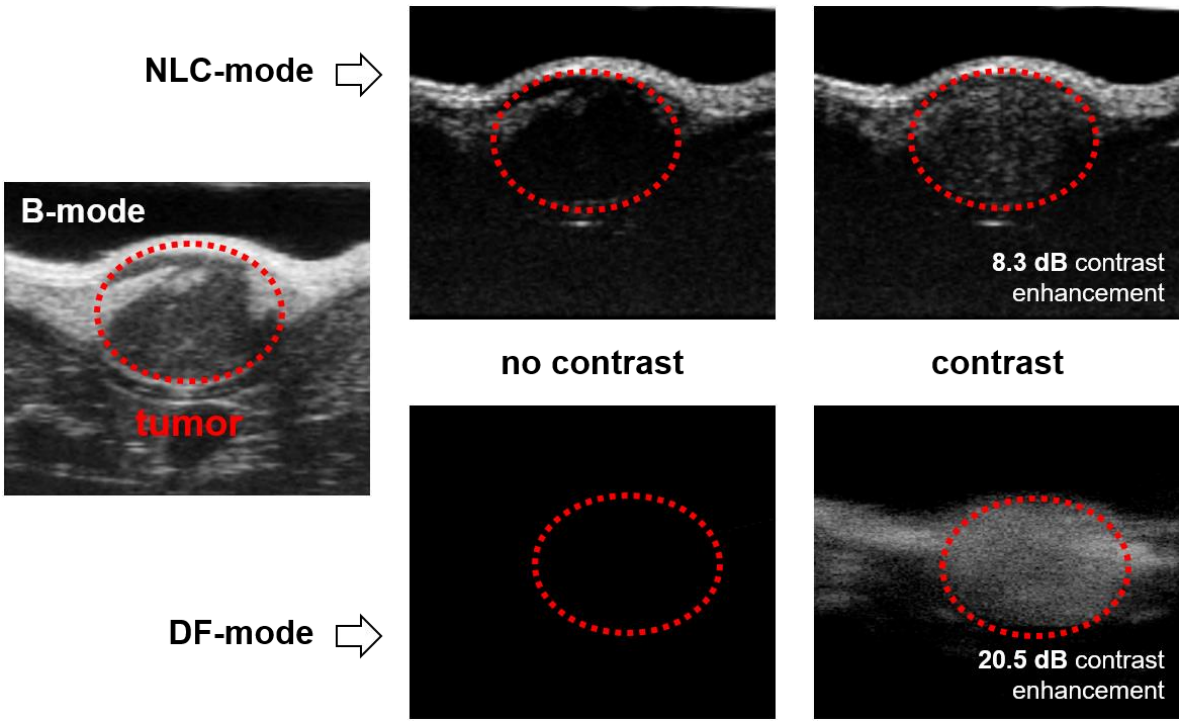

Figure B.2 Comparison of conventional nonlinear contrast (NLC) imaging to superharmonic dual-frequency (DF) imaging using a high-frequency array and the prototype low-frequency outrigger. Images depict a subcutaneous rat fibrosarcoma tumor.

We have since demonstrated that this prototype device can be used for ultrafast superharmonic imaging, which can be followed with localization microscopy processing to create super-resolved images with 20 µm resolution (86). While many ultrasound super-resolution techniques have been published to date (186), superharmonic imaging presents a distinct advantage over traditional spatiotemporal based filtering methods, allowing slow-flowing and even stationary microbubbles to be detected (86). Additionally, the high SNR afforded by dual-frequency imaging improves microbubble detection and localization. Combining super-resolution processing with superharmonic imaging also allows functional information, such as flow velocity, to be quantified

(86). For example, **Figure B.3** shows super-resolved vascular flow and direction in a free-breathing rat kidney, measured with this prototype DF device.

Co-linear transducers provide a bridge to cross the existing gap in dual-frequency transducer technology because of their rapid and affordable prototyping, but they also present limitations that must be considered. Because the transducers are physically arranged in parallel, the intersection of the LF and HF beams – the focal zone – is fixed and cannot be modified after assembly. These devices also tend to have a large footprint, which can be prohibitive in scenarios where space is limited, such as imaging of the mouse brain. Nevertheless, these transducers are a valuable tool for the progression of DF imaging.

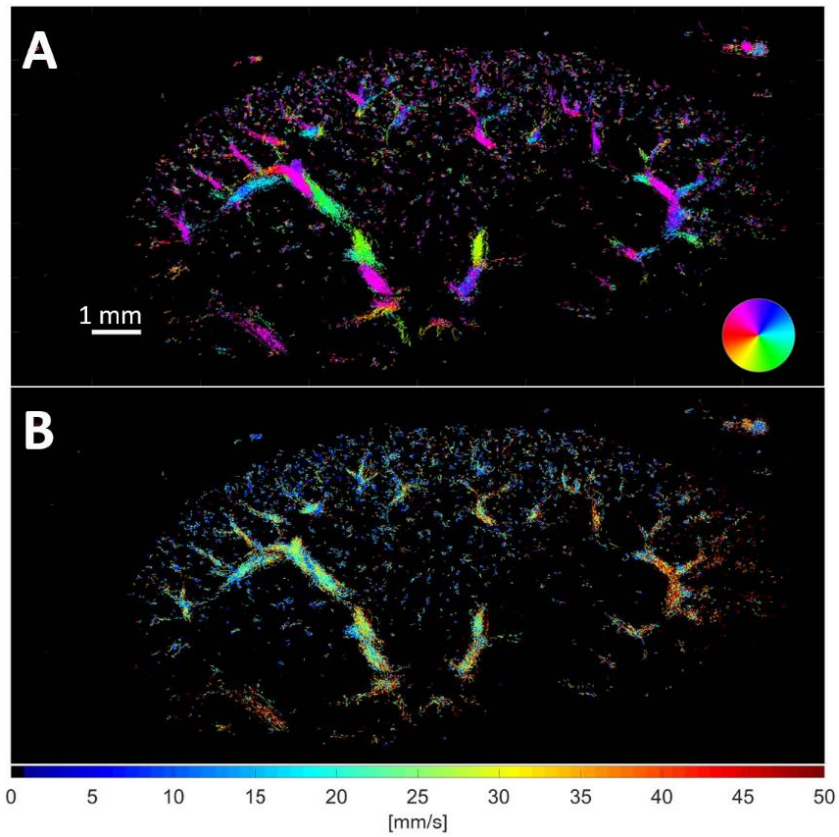

Figure B.3 Super-resolved flow images of a rat kidney created with the prototype dual-frequency transducer: velocity **A)** direction and **B)** magnitude. © 2020 IEEE. Reprinted, with permission, from Kierski *et al.*, "Superharmonic ultrasound for motion-independent localization microscopy: applications to microvascular imaging from low to high flow rates," *Trans UFFC*, 2020.

B.2 Capacitive Micromachined Ultrasonic Transducers

All the transducers discussed in the previous sections of this dissertation have been based on piezoelectric materials, which are typically used for biomedical ultrasound imaging. The capacitive micromachined ultrasonic transducer (CMUT) is an alternative transducer technology. Whereas piezoelectric transducers use piezoelectric crystals to send and receive acoustic waves, CMUTs consist of microscopic capacitor cells that can sense and generate sound (187). These transducers provide some benefits over traditional piezoelectric technology, including the low cost of microfabricated devices, easy integration and miniaturization with electronics, and larger operating bandwidth (187). Because of this latter characteristic, CMUTs offer an attractive solution for superharmonic imaging, which requires transducers with extremely wide operating bandwidth.

Our collaborators have developed and tested two CMUT architectures specifically designed for DF acoustic angiography. The first CMUT utilizes a novel design that includes spacers within the capacitor (**Figure B.4A**) – this allows the device to operate in both "conventional" and "collapse" mode (by resting the top plate on the spacers) simply by switching the applied voltage (188). This CMUT device exhibits greater than 125% bandwidth with transmit at 3 MHz and receive up to 13 MHz (188). The second design, an ultrawide-band CMUT, provides similar performance, with 130% bandwidth and transmit and receive at 3 and 15 MHz, respectively (**Figure B.4B**) (189). These two devices can detect microbubbles *in vitro* with high SNR. In the future, these novel transducers will be tested *in vivo*, and we anticipate that DF CMUTs will create a different path to achieve deeper superharmonic imaging, parallel to the DF stacked array design described in Chapter 3.

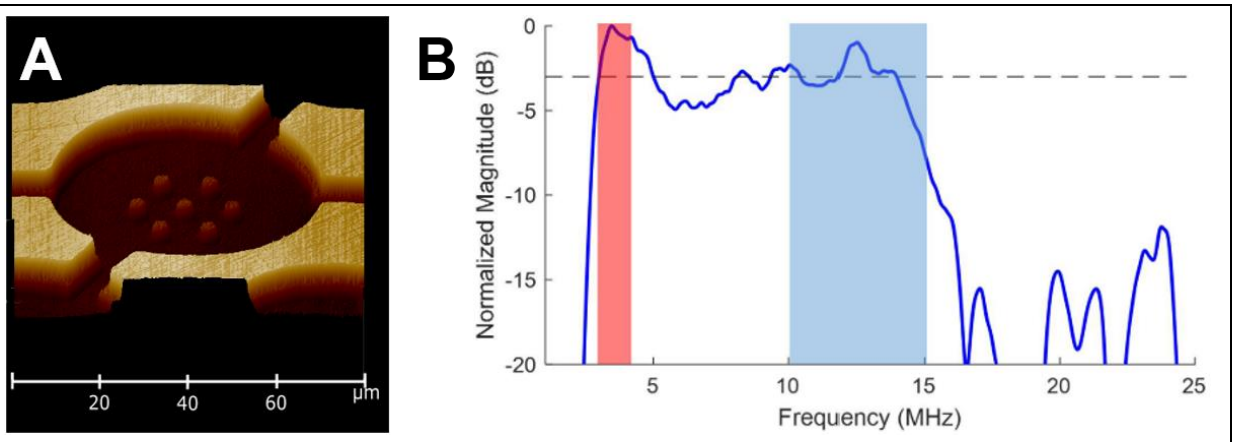

Figure B.4 Dual-frequency capacitive micromachined ultrasonic transducers: **A)** atomic force microscopy image of the novel CMUT design with spacers inside the cavity and **B)** bandwidth measured for the ultrawide-band CMUT with transmit (red) and receive (blue) regions. © 2020 IEEE. Panel A: Reprinted, with permission, from Mahmud *et al.*, "An improved CMUT structure enabling release and collapse of the plate in the same Tx/Rx cycle for dual-frequency acoustic angiography," *Trans UFFC*, 2020. Panel B: Reprinted, with permission, from Sanders *et al.*, "An ultra-wideband capacitive micromachined ultrasonic transducer (CMUT) array for acoustic angiography: preliminary results," *Proc IUS*, 2020.

APPENDIX C
CHARACTERIZING LUNG ORGANOIDS WITH ACOUSTIC ANGIOGRAPHY

Acoustic angiography is often relied on as a technique for imaging tumor-associated angiogenesis; indeed, many of the previous studies using this technique have focused on detecting, evaluating, and quantifying microvasculature in cancerous tumors. However, there is a plethora of other diseases and applications where non-invasive microvascular ultrasound imaging is a valuable tool. For example, as an established preclinical imaging technique, acoustic angiography can be used to characterize and validate other imaging methods or research models (41,44,45,47). This appendix describes how acoustic angiography was used to evaluate one such model.

Research on human pathogens is limited to those that affect hematopoietic cells (*i.e.*, cells in the blood, bone marrow, and spleen), which can be tested in humanized mouse models (45,190). To study pathogens that affect other cell types, more advanced models are needed. Our collaborators developed a novel model of humanized "lung-only" mice by implanting immunodeficient mice with human lung tissue, which developed into ectopic organoids populated with human epithelial, endothelial, and mesenchymal cells, in addition to hematopoietic cells (45). To characterize the development of these implants, we performed high-frequency B-mode and acoustic angiography imaging using the dual-frequency wobbler system described previously (45,150).

Volumetric high-frequency ultrasound imaging was performed to measure organoid growth. To measure implant volume, the diameter of the organoid was measured in each plane of the B-mode images using MATLAB (Mathworks, Inc., Natick, MA, USA), and the ellipsoidal volume was calculated (**Figure C.1**). Then, organoid vascularization was evaluated with acoustic angiography. The microvascular images revealed that the organoids were successfully

vascularized and depicted characteristics reminiscent of those associated with wound healing or tumor growth (35,191) – dense, chaotic, tortuous vascular networks were exposed (**Figure C.2**). This non-invasive imaging data was able to provide greater insight into implant development *in situ* and complement *ex vivo* histological and immunohistochemical methods. Our collaborators went on to demonstrate that the organoid vasculature revealed by acoustic angiography was human in origin and that this model can be used to study a variety of human pathogens, such as Middle East respiratory syndrome coronavirus and Zika virus (45).

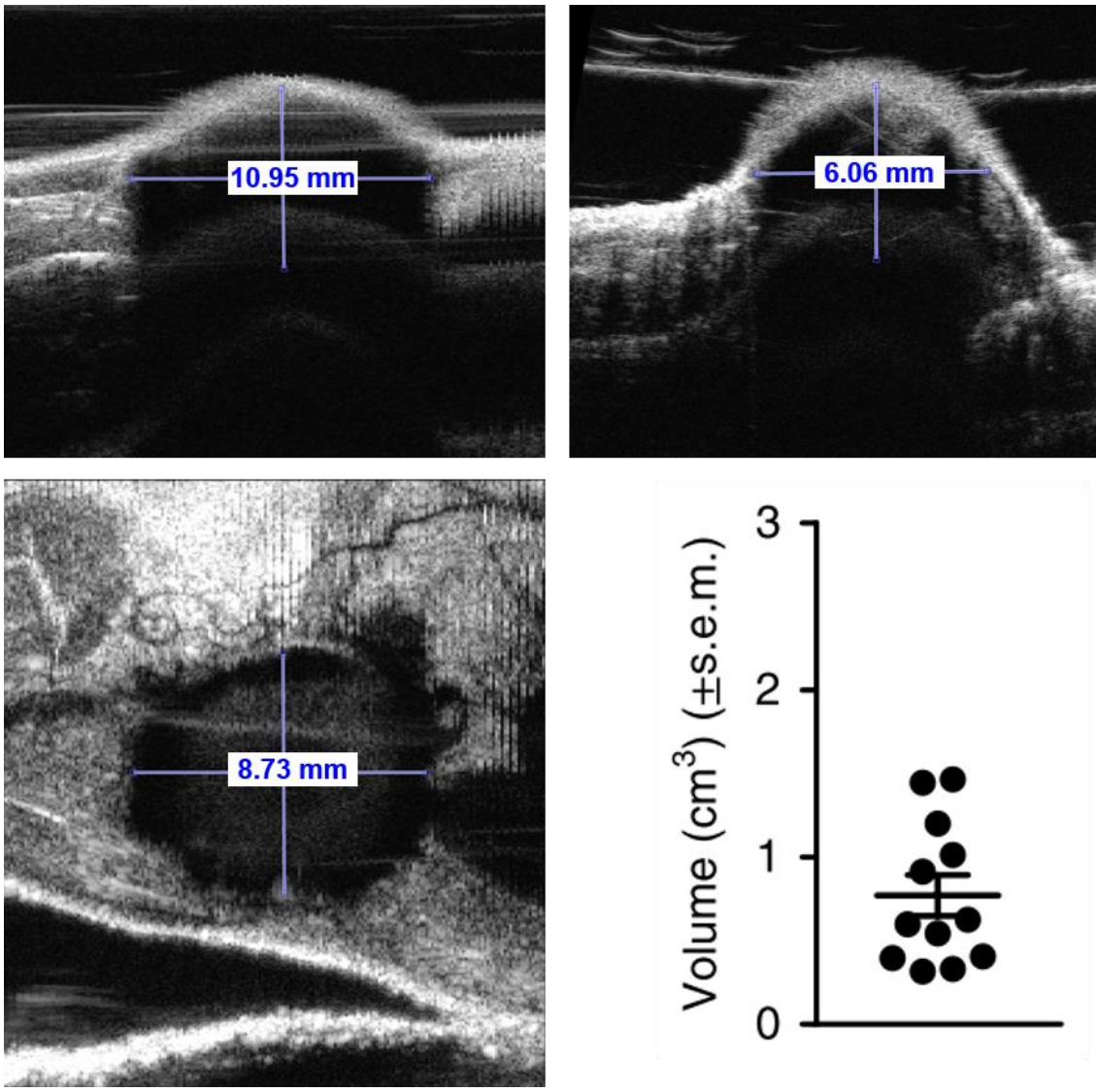

Figure C.1 B-mode measurement of lung organoid volume: example measurements from orthogonal B-mode planes in one implant and volume measured for N = 12 organoids.

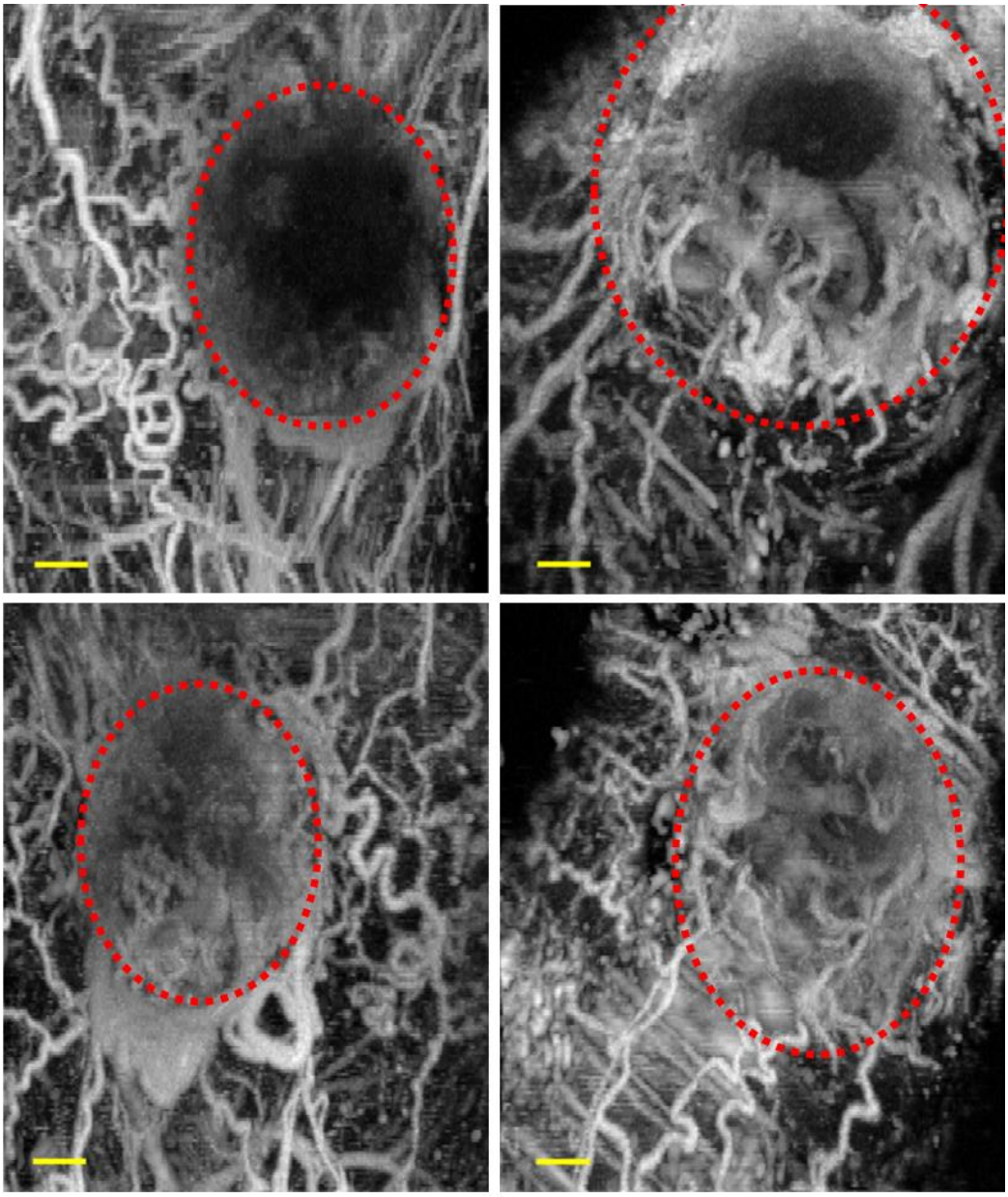

Figure C.2 Maximum intensity projections of acoustic angiography images of lung organoids. Each panel is a different implant (outlined in red), showing varying degrees of growth and vascularization. Top left: organoid depicted in **Figure C.1**. Scale bar = 2 mm.

APPENDIX D
CURATING A LARGE ACOUSTIC ANGIOGRAPHY DATASET

While this dissertation has focused on improving the acoustic angiography imaging technique, it is important to also consider how acoustic angiography images can be used diagnostically. Previously, acoustic angiography images have been analyzed in one of two ways: 1) examined qualitatively by readers or 2) quantitatively analyzed for vessel statistics (37). In order to quantify morphological vessel features, like tortuosity, vessels must be individually segmented from acoustic angiography volumes using a semi-manual segmentation algorithm [cite], which requires active input from an experienced user (33). Combining vessel segmentation on acoustic angiography images with a clustering algorithm, a previous study demonstrated high sensitivity and specificity (87% and 94%, respectively) for tumor detection in a spontaneous breast cancer model in mice (37).

Recently, machine learning approaches for image classification (192) have risen to the forefront of medical imaging research. Machine learning methods may provide the opportunity to achieve rapid and accurate differentiation of tumors from healthy tissue without the need for vessel segmentation. Furthermore, class activation mapping (193) can be used to ascertain which areas in an image contribute to classification, providing an avenue to not only differentiate but also detect and locate tumor-associated features within an image. However, machine learning requires large datasets for network training. To explore machine learning-based methods of classification on acoustic angiography images, a comprehensive dataset of tumor and control images must be generated.

To that end, we have curated a large dataset of acoustic angiography images collected from healthy or tumor-bearing female rats (Fischer 344, Charles River Laboratories, Durham, NC,

USA) using the DF wobbler system described previously (150). Tumor volumes were acquired from subcutaneous fibrosarcoma tumors implanted in the right flank, while control volumes were collected in the right and left flanks of healthy animals. In total, 74 rodents were imaged. In addition, data from previous studies that occurred between 2012 and 2019 were extracted from lab

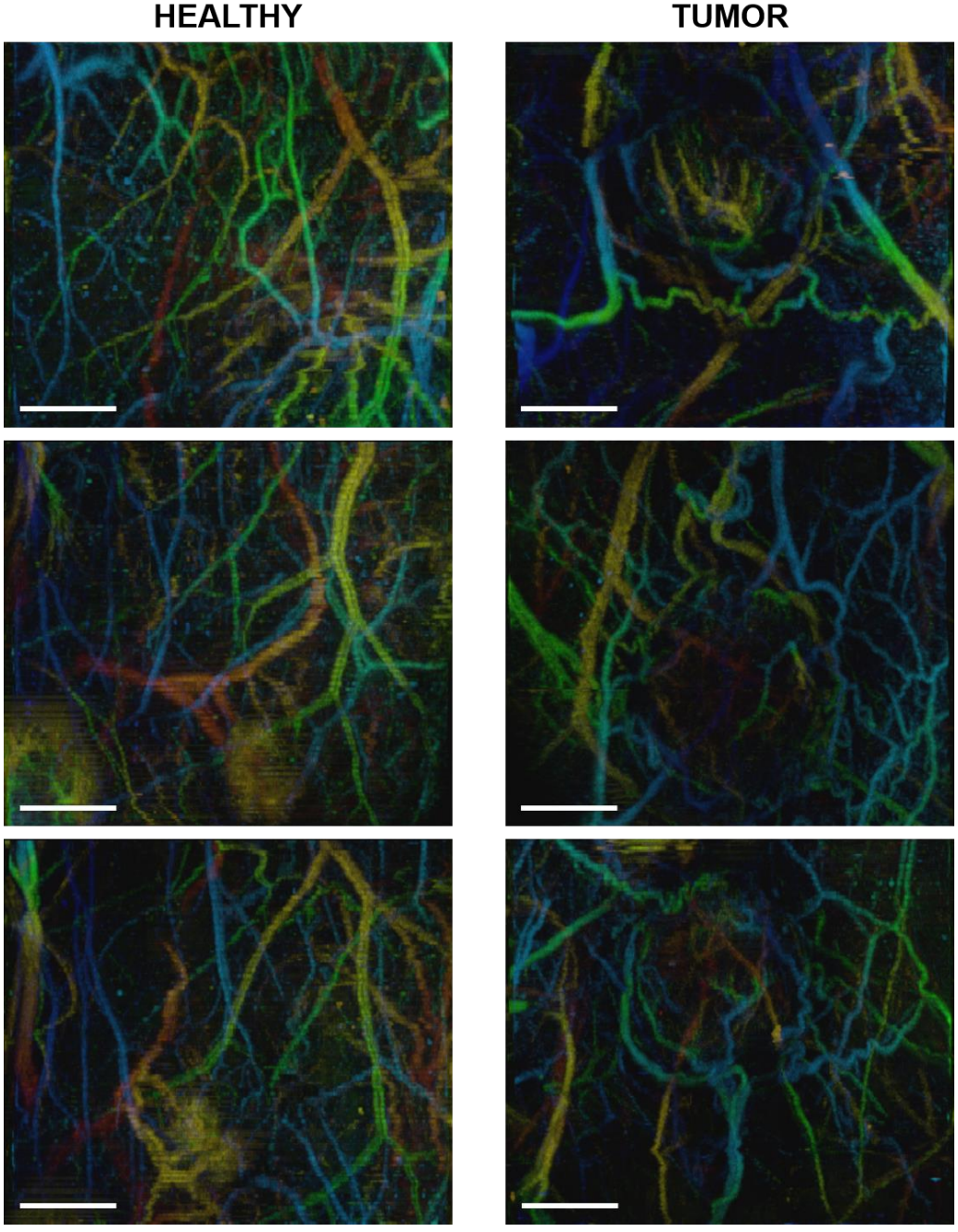

Figure D.1 Example depth-colored maximum intensity projections of acoustic angiography data: healthy (left column) and tumor-bearing (right column) tissue. Scale bar = 5 mm.

archives. All image volumes were processed in MATLAB (Mathworks, Inc., Natick, MA, USA) to remove image artifacts (*e.g.*, from skin or bone) to create clean microvascular images. After processing, the dataset consisted of 118 and 148 control and tumor volumes, respectively. These data can be utilized in a variety of ways, including as 3D volumes, 2D maximum intensity projections, or 2D depth-colored projections (such as those in **Figure D.1**).

In the future, this dataset will be used to train neural networks for tumor detection. In preliminary testing, an algorithm based on the EfficientNetB0 model (194) has achieved 80% accuracy using a subset of 160 images, and the results of class activation mapping are promising, showing that the network will indeed rely on vessel characteristics for classification (**Figure D.2**). As this work continues, the dataset will be expanded, and machine learning models will be tuned to maximize accuracy. Additionally, we intend to make this dataset publicly available to allow testing of new methods for tumor detection, vessel segmentation, and tortuosity quantification as these approaches are developed.

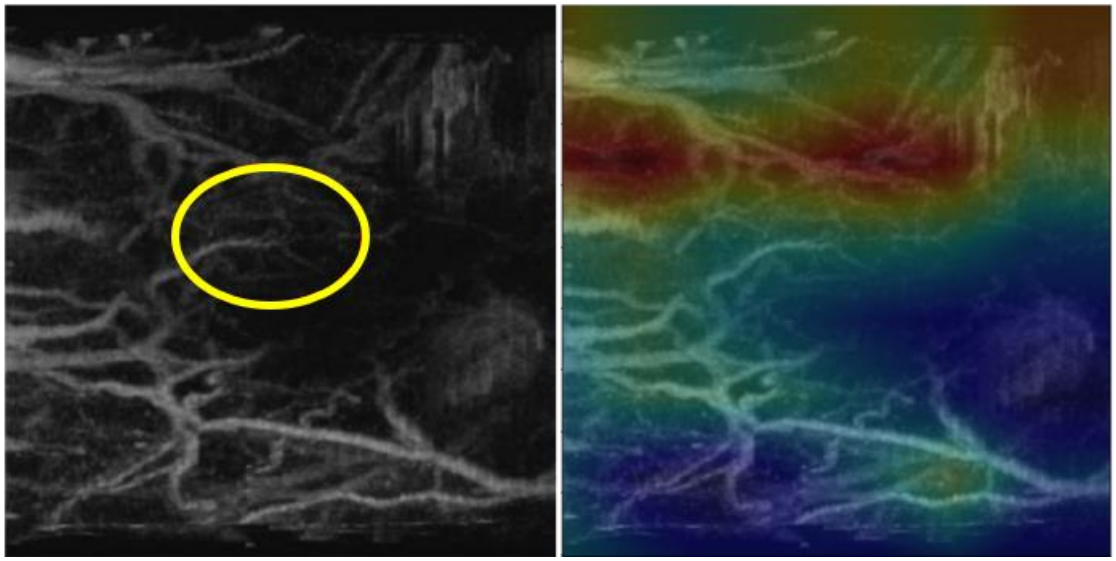

Figure D.2 Preliminary results using machine learning to detect tumors in acoustic angiography images: input maximum intensity projection with tumor location denoted by yellow contour (left) and output class activation map (right), showing higher activation in areas near the tumor with more vasculature (warmer colors).

BIBLIOGRAPHY

1. Jain RK. Normalizing tumor vasculature with anti-angiogenic therapy: A new paradigm for combination therapy. Nat Med. 2001;7:987–9.
2. Folkman J. Tumor Angiogenesis: Therapeutic Implications. N Engl J Med. 1971;285:1182–6.
3. Hanahan D, Weinberg RA. Hallmarks of Cancer: The Next Generation. Cell. 2011;144:646–74.
4. Jain RK. Normalization of tumor vasculature: An emerging concept in angiogenic therapy. Science. 2005;307:58–62.
5. Wu G, Yang J, Zhang T, Morelli JN, Giri S, Li X, et al. The diagnostic value of non-contrast enhanced quiescent interval single shot (QISS) magnetic resonance angiography at 3T for lower extremity peripheral arterial disease, in comparison to CT angiography. J Cardiovasc Magn Reson. 2016;18.
6. Pinker K, Bogner W, Baltzer P, Trattnig S, Gruber S, Abeyakoon O, et al. Clinical application of bilateral high temporal and spatial resolution dynamic contrast-enhanced magnetic resonance imaging of the breast at 7 T. Eur Radiol. 2014;24:913–20.
7. Reiner CS, Roessle M, Thiesler T, Eberli D, Klotz E, Frauenfelder T, et al. Computed Tomography Perfusion Imaging of Renal Cell Carcinoma. Invest Radiol. 2013;48:1.
8. Goldberg BB, Gramiak R, Freimanis AK. Early History of Diagnostic Ultrasound: the Role of American Radiologists. Am J Roentgenol. 1993;160:189–94.
9. Cobbold RSC. Foundations of Biomedical Ultrasound. Oxford University Press; 2007.
10. Noce JP. Fundamentals of diagnostic ultrasonography. Biomed Instrum Technol. 1990;24:456–9.
11. Rizzatto G. Ultrasound Transducers. Eur J Radiol. 1998;27:S188–95.
12. Bercoff J, Montaldo G, Loupas T, Savery D, Mézière F, Fink M, et al. Ultrafast compound doppler imaging: Providing full blood flow characterization. IEEE Trans Ultrason Ferroelectr Freq Control. 2011;58:134–47.
13. Klibanov AL, Hossack JA. Ultrasound in Radiology: from Anatomic, Functional, Molecular Imaging to Drug Delivery and Image-Guided Therapy. Invest Radiol. 2015;50:657–70.
14. Ferrara K, Pollard R, Borden M. Ultrasound Microbubble Contrast Agents: Fundamentals and Application to Gene and Drug Delivery. Annu Rev Biomed Eng. 2007;9:415–47.
15. Kosareva A, Abou-Elkacem L, Chowdhury S, Lindner JR, Kaufmann BA. Seeing the Invisible—Ultrasound Molecular Imaging. Ultrasound Med Biol. 2019;00.
16. De Jong N, Bouakaz A, Frinking P. Basic acoustic properties of microbubbles. Echocardiography. 2002;19:229–40.

17. Tranquart F, Grenier N, Eder V, Pourcelot L. Clinical Use of Ultrasound Tissue Harmonic Imaging. Ultrasound Med Biol. 1999;25:889–94.

18. Kim AHY, Choi BIHN, Kim KWON, Lee JAEY, Han JKOO. Comparison of Contrast-Enhanced Fundamental Imaging, Second-Harmonic Imaging, and Pulse-Inversion Harmonic Imaging. Invest Radiol. 2001;36:582–8.

19. Shen C-C, Chou Y-H, Li P-C. Pulse Inversion Techniques in Ultrasonic Nonlinear Imaging. J Med Ultrasound. 2005;13:3–17.

20. Eckersley RJ, Chin CT, Burns PN. Optimising phase and amplitude modulation schemes for imaging microbubble contrast agents at low acoustic power. Ultrasound Med Biol. 2005;31:213–9.

21. Bouakaz A, Frigstad S, Ten Cate FJ, Jong N DE. Super Harmonic Imaging: A New Imaging Technique For Improved Contrast Detection. Ultrasound Med Biol. 2002;28:59–68.

22. Kruse DE, Ferrara KW. A new imaging strategy using wideband transient response of ultrasound contrast agents. IEEE Trans Ultrason Ferroelectr Freq Control. 2005;52:1320–9.

23. van Neer PLMJ, Matte G, Danilouchkine MG, de Jong N, Prins C, van den Adel F. Super-Harmonic Imaging: Development of an Interleaved Phased-Array Transducer. IEEE Trans Ultrason Ferroelectr Freq Control. 2010;57:455–68.

24. Bouakaz A, Krenning BJ, Vletter WB, Ten Cate FJ, De Jong N. Contrast superharmonic imaging: A feasibility study. Ultrasound Med Biol. 2003;29:547–53.

25. Guiroy A, Novell A, Ringgaard E, Lou-Moeller R, Grégoire JM, Abellard AP, et al. Dual-frequency transducer for nonlinear contrast agent imaging. IEEE Trans Ultrason Ferroelectr Freq Control. 2013;60:2634–44.

26. Gessner R, Lukacs M, Lee M, Cherin E, Foster FS, Dayton PA. High-Resolution, High-Contrast Ultrasound Imaging Using a Prototype Dual-Frequency Transducer : In Vitro and In Vivo Studies. IEEE Trans Ultrason Ferroelectr Freq Control. 2010;57:1772–81.

27. Gessner RC, Frederick CB, Foster FS, Dayton PA. Acoustic Angiography: A New Imaging Modality for Assessing Microvasculature Architecture. Int J Biomed Imaging. 2013;936593.

28. Foster FS, Pavlin CJ, Harasiewicz KA, Christopher DA, Turnbull DH. Advances in ultrasound biomicroscopy. Ultrasound Med Biol. 2000;26:1–27.

29. Lindsey BD, Rojas JD, Martin KH, Shelton SE, Dayton PA. Acoustic characterization of contrast-to-tissue ratio and axial resolution dual-frequency contrast-specific acoustic angiography imaging. IEEE Trans Ultrason Ferroelec, Freq Contr. 2014;61:1668–87.

30. Lindsey BD, Shelton SE, Dayton PA. OPTIMIZATION OF CONTRAST-TO-TISSUE RATIO THROUGH PULSE WINDOWING IN DUAL-FREQUENCY “‘ACOUSTIC ANGIOGRAPHY’” IMAGING. Ultrasound Med Biol. 2015;41:1884–95.

31. Lindsey BD, Rojas JD, Dayton PA. On the Relationship Between Microbubble Fragmentation, Deflation and Broadband Superharmonic Signal Production. Ultrasound Med Biol. 2015;41:1711–25.

32. Bullitt E, Gerig G, Pizer SM, Lin W, Aylward SR. Measuring Tortuosity of the Intracerebral Vasculature from MRA Images. IEEE Trans Med Imaging. 2003;22:1163–71.

33. Aylward SR, Bullitt E. Initialization, noise, singularities, and scale in height ridge traversal for tubular object centerline extraction. IEEE Trans Med Imaging. 2002;21:61–75.

34. Gessner RC, Aylward SR, Dayton PA. Mapping Microvasculature with Acoustic Angiography Yields Quantifiable Differences between Healthy and Tumor-bearing Tissue Volumes in a Rodent Model. Radiology. 2012;264:733–40.

35. Shelton SE, Lee YZ, Lee M, Cherin E, Foster FS, Aylward SR, et al. Quantification of microvascular tortuosity during tumor evolution using acoustic angiography. Ultrasound Med Biol. 2015;41:1896–904.

36. Rao SR, Shelton SE, Dayton PA. The "Fingerprint" of Cancer Extends Beyond Solid Tumor Boundaries: Assessment With a Novel Ultrasound Imaging Approach. IEEE Trans Biomed Eng. 2016;63:1082–6.

37. Shelton SE, Stone J, Gao F, Zeng D, Dayton PA. Microvascular Ultrasonic Imaging of Angiogenesis Identifies Tumors in a Murine Spontaneous Breast Cancer Model. Int J Biomed Imaging. 2020;7862089.

38. Rojas JD, Papadopoulou V, Czernuszewicz T, Rajamahendiran R, Chytil A, Chiang Y-C, et al. Ultrasound Measurement of Vascular Density to Evaluate Response to Anti-angiogenic Therapy in Renal Cell Carcinoma. IEEE Trans Biomed Eng. 2019;66:873–80.

39. Kasoji SK, Rivera JN, Gessner RC, Chang SX, Dayton PA. Early Assessment of Tumor Response to Radiation Therapy using High-Resolution Quantitative Microvascular Ultrasound Imaging. Theranostics. 2018;8:156–68.

40. Kasoji SK, Rivera JN, Gessner RC, Chang SX, Dayton PA. Early Assessment of Tumor Response to Radiation Therapy using High-Resolution Quantitative Microvascular Ultrasound Imaging: Erratum. Theranostics. 2018;8:4601–3.

41. Marvin CM, Ding S, White RE, Orlova N, Wang Q, Zywot EM, et al. On Command Drug Delivery via Cell-Conveyed Phototherapeutics. Small. 2019;15:1901442.

42. Shelton SE, Lindsey BD, Tsuruta JK, Foster FS, Dayton PA. MOLECULAR ACOUSTIC ANGIOGRAPHY: A NEW TECHNIQUE FOR HIGH-RESOLUTION SUPERHARMONIC ULTRASOUND MOLECULAR IMAGING. Ultrasound Med Biol. 2016;42:769–81.

43. Lindsey BD, Shelton SE, Foster FS, Dayton PA. Assessment of Molecular Acoustic Angiography for Combined Microvascular and Molecular Imaging in Preclinical Tumor Models. Mol Imaging Biol. 2017;19:194–202.

44. Dunleavey JM, Xiao L, Thompson J, Kim MM, Shields JM, Shelton SE, et al. Vascular channels formed by subpopulations of PECAM1 þ melanoma cells. Nat Commun. 2014;5.

45. Wahl A, De C, Abad Fernandez M, Lenarcic EM, Xu Y, Cockrell AS, et al. Precision mouse models with expanded tropism for human pathogens. Nat Biotechnol. 2019;37:1163–73.

46. Mohanty K, Papadopoulou V, Newsome IG, Shelton S, Dayton PA, Muller M. Ultrasound multiple scattering with microbubbles can differentiate between tumor and healthy tissue in vivo. Phys Med Biol. 2019;64.

47. Panfilova A, Shelton SE, Caresio C, van Sloun RJG, Molinari F, Wijkstra H, et al. On the Relationship between Dynamic Contrast-Enhanced Ultrasound Parameters and the Underlying Vascular Architecture Extracted from Acoustic Angiography. Ultrasound Med Biol. 2019;45:539–48.

48. Shelton SE, Lindsey BD, Dayton PA, Lee YZ. First-in-Human Study of Acoustic Angiography in the Breast and Peripheral Vasculature. Ultrasound Med Biol. 2017;43:2939–46.

49. Hu S, Wang L V. Photoacoustic imaging and characterization of the microvasculature. J Biomed Opt. 2010;15:011101.

50. Demené C, Mairesse J, Baranger J, Tanter M, Baud O. Ultrafast Doppler for neonatal brain imaging. Neuroimage. 2019;185:851–6.

51. Christensen-Jeffries K, Couture O, Dayton PA, Eldar YC, Hynynen K, Kiessling F, et al. Super-resolution Ultrasound Imaging. Ultrasound Med Biol. 2020;46:865–91.

52. Jiang Z zhen, Huang Y hua, Shen H liang, Liu X tian. Clinical Applications of Superb Microvascular Imaging in the Liver, Breast, Thyroid, Skeletal Muscle, and Carotid Plaques. J Ultrasound Med. 2019;38:2811–20.

53. Park AY, Seo BK, Cha SH, Yeom SK, Lee SW, Chung HH. An innovative ultrasound technique for evaluation of tumor vascularity in breast cancers: Superb micro-vascular imaging. J Breast Cancer. 2016;19:210–3.

54. Zhan J, Diao XH, Jin JM, Chen L, Chen Y. Superb Microvascular Imaging - A new vascular detecting ultrasonographic technique for avascular breast masses: A preliminary study. Eur J Radiol. 2016;85:915–21.

55. Lee DH, Lee JY, Han JK. Superb microvascular imaging technology for ultrasound examinations: Initial experiences for hepatic tumors. Eur J Radiol. Elsevier Ireland Ltd; 2016;85:2090–5.

56. Ryoo I, Suh S, You SH, Seol HY. Usefulness of Microvascular Ultrasonography in Differentiating Metastatic Lymphadenopathy from Tuberculous Lymphadenitis. Ultrasound Med Biol. 2016;42:2189–95.

57. Ishikawa M, Ota Y, Nagai M, Kusaka G, Tanaka Y, Naritaka H. Ultrasonography Monitoring with Superb Microvascular Imaging Technique in Brain Tumor Surgery. World Neurosurg. 2017;97:749.e11-749.e20.

58. Mace E, Montaldo G, Cohen I, Baulac M, Fink M, Tanter M. Functional ultrasound imaging of the brain. Nat Methods. 2011;8:662–4.

59. Mace E, Montaldo G, Osmanski B, Cohen I, Fink M, Tanter M. Functional ultrasound imaging of the brain: theory and basic principles. IEEE Trans Ultrason Ferroelectr Freq Control. 2013;60:492–506.

60. Stanziola A, Leow CH, Bazigou E, Weinberg PD, Tang MX. ASAP: Super-Contrast Vasculature Imaging using Coherence Analysis and High Frame-Rate Contrast Enhanced Ultrasound. IEEE Trans Med Imaging. 2018;37:1847–56.

61. Leow CH, Bush NL, Stanziola A, Braga M, Shah A, Hernandez-Gil J, et al. 3D microvascular imaging using high frame rate ultrasound and ASAP without contrast agents: development and initial in vivo evaluation on non-tumour and tumour models. IEEE Trans Ultrason Ferroelectr Freq Control. 2019;66:939–48.

62. Yao J, Wang L V. Photoacoustic Microscopy. Laser Photon Rev. 2013;7.

63. Yang Z, Chen J, Yao J, Lin R, Meng J, Liu C, et al. Multi-parametric quantitative microvascular imaging with optical-resolution photoacoustic microscopy in vivo. Opt Express. 2014;22:1500–11.

64. Yeh C, Soetikno B, Hu S, Maslov KI, Wang L V. Microvascular quantification based on contour-scanning photoacoustic microscopy. J Biomed Opt. 2014;19:96011.

65. Laufer J, Johnson P, Zhang E, Treeby B, Cox B, Pedley B, et al. In vivo preclinical photoacoustic imaging of tumor vasculature development and therapy. J Biomed Opt. 2012;17:056016.

66. Qin W, Jin T, Guo H, Xi L. Large-field-of-view optical resolution photoacoustic microscopy. Opt Express. 2018;26:4271–8.

67. Kruger RA, Lam RB, Reinecke DR, Del Rio SP, Doyle RP. Photoacoustic angiography of the breast. Med Phys. 2010;37:6096–100.

68. Kruger RA, Kuzmiak CM, Lam RB, Reinecke DR, Rio SP Del, Steed D. Dedicated 3D photoacoustic breast imaging. Med Phys. 2013;40.

69. Yamaga I, Kawaguchi-Sakita N, Asao Y, Matsumoto Y, Yoshikawa A, Fukui T, et al. Vascular branching point counts using photoacoustic imaging in the superficial layer of the breast: A potential biomarker for breast cancer. Photoacoustics. 2018;11:6–13.

70. Toi M, Asao Y, Matsumoto Y, Sekiguchi H, Yoshikawa A, Takada M, et al. Visualization of tumor-related blood vessels in human breast by photoacoustic imaging system with a hemispherical detector array. Sci Rep. 2017;7:41970.

71. Lin L, Hu P, Shi J, Appleton CM, Maslov K, Li L, et al. Single-breath-hold photoacoustic computed tomography of the breast. Nat Commun. 2018;9.

72. Wray P, Lin L, Hu P. Photoacoustic computed tomography of human extremities. J Biomed Opt. 2019;24:1.

73. Nishiyama M, Namita T, Kondo K, Yamakawa M, Shiina T. Ring-array photoacoustic

tomography for imaging human finger vasculature. J Biomed Opt. 2019;24:096005.

74. Liu M, Chen Z, Zabihian B, Sinz C, Zhang E, Beard PC, et al. Combined multi-modal photoacoustic tomography, optical coherence tomography (OCT) and OCT angiography system with an articulated probe for in vivo human skin structure and vasculature imaging. Biomed Opt Express. 2016;7:3390.

75. Chen Z, Rank E, Meiburger KM, Sinz C, Hodul A, Zhang E, et al. Non-invasive multimodal optical coherence and photoacoustic tomography for human skin imaging. Sci Rep. 2017;7:1–11.

76. Christensen-Jeffries K, Browning RJ, Tang MX, Dunsby C, Eckersley RJ. In vivo acoustic super-resolution and super-resolved velocity mapping using microbubbles. IEEE Trans Med Imaging. 2015;34:433–40.

77. Errico C, Pierre J, Pezet S, Desailly Y, Lenkei Z, Couture O, et al. Ultrafast ultrasound localization microscopy for deep super-resolution vascular imaging. Nature. 2015;527:499–502.

78. Lin F, Shelton SE, Espindola D, Rojas JD, Pinton G, Dayton PA. 3-D ultrasound localization microscopy for identifying microvascular morphology features of tumor angiogenesis at a resolution beyond the diffraction limit of conventional ultrasound. Theranostics. 2017;7:196–204.

79. Opacic T, Dencks S, Theek B, Piepenbrock M, Ackermann D, Rix A, et al. Motion model ultrasound localization microscopy for preclinical and clinical multiparametric tumor characterization. Nat Commun. 2018;9:1–13.

80. Zhu J, Rowland EM, Harput S, Riemer K, Leow CH, Clark B, et al. 3D super-resolution US imaging of rabbit lymph node vasculature in vivo by using microbubbles. Radiology. 2019;291:642–50.

81. Ghosh D, Peng J, Brown K, Sirsi S, Mineo C, Shaul PW, et al. Super-resolution ultrasound imaging of skeletal muscle microvascular dysfunction in an animal model of type 2 diabetes. J Ultrasound Med. 2019;38:2589–99.

82. Hingot V, Errico C, Heiles B, Rahal L, Tanter M, Couture O. Microvascular flow dictates the compromise between spatial resolution and acquisition time in Ultrasound Localization Microscopy. Sci Rep. 2019;9:1–10.

83. Lin F, Tsuruta JK, Rojas JD, Dayton PA. Optimizing Sensitivity of Ultrasound Contrast-Enhanced Super-Resolution Imaging by Tailoring Size Distribution of Microbubble Contrast Agent. Ultrasound Med Biol. 2017;43:2488–93.

84. Ghosh D, Xiong F, Sirsi SR, Shaul PW, Mattrey RF, Hoyt K. Toward optimization of in vivo super-resolution ultrasound imaging using size-selected microbubble contrast agents. Med Phys. 2017;

85. Brown J, Christensen-Jeffries K, Harput S, Zhang G, Zhu J, Dunsby C, et al. Investigation of Microbubble Detection Methods for Super-resolution Imaging of Microvasculature. IEEE Trans Ultrason Ferroelectr Freq Control. 2019;66:676–91.

86. Kierski TM, Espindola D, Newsome IG, Cherin E, Yin J, Foster FS, et al. Super harmonic ultrasound for motion-independent localization microscopy: applications to microvascular imaging from low to high flow rates. IEEE Trans Ultrason Ferroelectr Freq Control. 2020;67:957–67.

87. Deruiter RM, Markley EN, Rojas JD, Pinton GF, Dayton PA. Transient acoustic vaporization signatures unique to low boiling point phase change contrast agents enable super-resolution ultrasound imaging without spatiotemporal filtering. AIP Adv. 2020;10:105124.

88. Zhang G, Harput S, Hu H, Christensen-Jeffries K, Zhu J, Brown J, et al. Fast acoustic wave sparsely activated localization microscopy: Ultrasound super-resolution using plane-wave activation of nanodroplets. IEEE Trans Ultrason Ferroelectr Freq Control. 2019;66:1039–46.

89. Zhang G, Harput S, Lin S, Christensen-Jeffries K, Leow CH, Brown J, et al. Acoustic wave sparsely activated localization microscopy (AWSALM): Super-resolution ultrasound imaging using acoustic activation and deactivation of nanodroplets. Appl Phys Lett. 2018;113.

90. Heiles B, Correia M, Hingot V, Pernot M, Provost J, Tanter M, et al. Ultrafast 3D Ultrasound Localization Microscopy Using a 32 × 32 Matrix Array. IEEE Trans Med Imaging. 2019;38:2005–15.

91. Harput S, Christensen-Jeffries K, Ramalli A, Brown J, Zhu J, Zhang G, et al. 3-D Super-Resolution Ultrasound Imaging with a 2-D Sparse Array. IEEE Trans Ultrason Ferroelectr Freq Control. 2019;67:1–1.

92. Dencks S, Piepenbrock M, Opacic T, Krauspe B, Stickeler E, Kiessling F, et al. Clinical Pilot Application of Super-Resolution US Imaging in Breast Cancer. IEEE Trans Ultrason Ferroelectr Freq Control. 2019;66:517–26.

93. Gramiak R, Shah PM. Echocardiography of the aortic root. Invest Radiol. 1968;3:356–66.

94. Hyvelin J-M, Gaud E, Costa M, Helbert A, Bussat P, Bettinger T, et al. Characteristics and Echogenicity of Clinical Ultrasound Contrast Agents: An In Vitro and In Vivo Comparison Study. J Ultrasound Med. 2017;36:941–53.

95. Feshitan JA, Chen CC, Kwan JJ, Borden MA. Microbubble size isolation by differential centrifugation. J Colloid Interface Sci. 2009;329:316–24.

96. Lee HJ, Yoon T-J, Yoon Y Il. Synthesis of ultrasound contrast agents: characteristics and size distribution analysis (secondary publication). Ultrasonography. 2017;36:378–84.

97. Frinking PJA, Bouakaz A, Kirkhorn J, Ten Cate FJ, De Jong N. Ultrasound contrast imaging: Current and new potential methods. Ultrasound Med Biol. 2000;26:965–75.

98. Shi WT, Forsberg F, Hall AL, Chiao RY, Liu J-B, Goldberg ' BB, et al. Subharmonic Imaging with Microbubble Contrast Agents: Initial Results. Ultrason Imaging. 1999;21:79–94.

99. Sridharan A, Eisenbrey JR, Liu J Bin, Machado P, Halldorsdottir VG, Dave JK, et al.

Perfusion estimation using contrast enhanced three-dimensional subharmonic ultrasound imaging: an in vivo study. Invest Radiol. 2013;48:654–60.

100. Hudson JM, Karshafian R, Burns PN. Quantification of Flow Using Ultrasound and Microbubbles: A Disruption Replenishment Model Based on Physical Principles. Ultrasound Med Biol. 2009;35:2007–20.

101. Fröhlich E, Muller R, Cui X-W, Schreiber-Dietrich D, Dietrich CF. Dynamic Contrast-Enhanced Ultrasound for Quantification of Tissue Perfusion. J Ultrasound Med. 2015;34:179–96.

102. Feingold S, Gessner R, Guracar IM, Dayton PA. Quantitative volumetric perfusion mapping of the microvasculature using contrast ultrasound. Invest Radiol. 2010;45.

103. Streeter J, Gessner R, Miles I, Dayton PA. Improving Sensitivity in Ultrasound Molecular Imaging by Tailoring Contrast Agent Size Distribution: In Vivo Studies. Mol Imaging. 2010;9:87–95.

104. Tsuruta JK, Schaub NP, Rojas JD, Streeter J, Klauber-DeMore N, Dayton P. Optimizing ultrasound molecular imaging of secreted frizzled related protein 2 expression in angiosarcoma. PLoS One. 2017;12:e0174281.

105. Kaufmann BA, Lewis C, Xie A, Mirza-Mohd A, Lindner JR. Detection of recent myocardial ischaemia by molecular imaging of P-selectin with targeted contrast echocardiography. Eur Heart J. 2007;28:2011–7.

106. Abou-Elkacem L, Bachawal S V, Willmann JK. Ultrasound Molecular Imaging: Moving Towards Clinical Translation. Eur J Radiol. 2015;84:1685–93.

107. Sirsi S, Feshitan J, Kwan J, Homma S, Borden M. Effect of Microbubble size on Fundamental Mode High Frequency Ultrasound Imaging in Mice. Ultrasound Med Biol. 2010;36:935–48.

108. Kaya M, Feingold S, Hettiarachchi K, Lee AP, Dayton PA. Acoustic responses of monodisperse lipid-encapsulated microbubble contrast agents produced by flow focusing. Bubble Sci Eng Technol. 2010;2:33–40.

109. Talu E, Hettiarachchi K, Zhao S, Powell RL, Lee AP, Longo L, et al. Tailoring the Size Distribution of Ultrasound Contrast Agents: Possible Method for Improving Sensitivity in Molecular Imaging. Mol Imaging. 2007;6:384–92.

110. Segers T, Kruizinga P, Kok MP, Lajoinie G, de Jong N, Versluis M. Monodisperse Versus Polydisperse Ultrasound Contrast Agents: Non-Linear Response, Sensitivity, and Deep Tissue Imaging Potential. Ultrasound Med Biol. 2018;44:1482–92.

111. Garg S, Thomas AA, Borden MA. The effect of lipid monolayer in-plane rigidity on in vivo microbubble circulation persistence. Biomaterials. 2013;34:6862–70.

112. Van Rooij T, Luan Y, Renaud G, Van Der Steen AFW, Versluis M, De Jong N, et al. NON-LINEAR RESPONSE AND VISCOELASTIC PROPERTIES OF LIPID-COATED MICROBUBBLES: DSPC VERSUS DPPC. Ultrasound Med Biol. 2015;41:1432–45.

113. Optison Package Insert. Marlborough, MA; 2016.

114. Definity Package Insert. North Billerica, MA; 2017.

115. Lindsey BD, Shelton SE, Martin KH, Ozgun KA, Rojas JD, Foster FS, et al. High Resolution Ultrasound Superharmonic Perfusion Imaging: In Vivo Feasibility and Quantification of Dynamic Contrast-Enhanced Acoustic Angiography. Ann Biomed Eng. 2017;45:939–48.

116. Kabalnov A, Bradley JA, Flaim S, Klein D, Pelura T, Peters B, et al. Dissolution of multicomponent microbubbles in the bloodstream: 2. Experiment. Ultrasound Med Biol. 1998;24:751–60.

117. de Jong N, Emmer M, van Wamel A, Versluis M. Ultrasonic characterization of ultrasound contrast agents. Med Biol Eng Comput. 2009;47:861–73.

118. Schneider M, Arditi M, Barrau MB, Brochot J, Broillet A, Ventrone R, et al. BR1: a new ultrasonographic contrast agent based on sulfur hexafluoride-filled micrububbles. Invest Radiol. 1995;30:451–7.

119. Kanbar E, Fouan D, Sennoga CA, Doinikov AA, Bouakaz A. Impact of Filling Gas on Subharmonic Emissions of Phospholipid Ultrasound Contrast Agents. Ultrasound Med Biol. 2017;43:1004–15.

120. Vevo MicroMarker ™ Non-Targeted Contrast Agent Kit : Protocol and Information Booklet. Toronto, ON;

121. Chomas JE, Dayton P, Alien J, Morgan K, Ferrara KW. Mechanisms of contrast agent destruction. IEEE Trans Ultrason Ferroelectr Freq Control. 2001;48:232–48.

122. Dayton PA, Morgan KE, Klibanov AL, Brandenburger GH, Ferrara KW. Optical and acoustical observations of the effects of ultrasound on contrast agents. IEEE Trans Ultrason Ferroelec, Freq Contr. 1999;46:220–32.

123. Streeter JE, Gessner R, Miles I, Dayton PA. Improving sensitivity in ultrasound molecular imaging by tailoring contrast agent size distribution: In vivo studies. Mol Imaging. 2010;9:87–95.

124. Fryar CD, Gu Q, Ogden CL. Anthropometric reference data for children and adults: United States, 2007-2010. Vital Heal Stat. 2012;1–40.

125. Nadler S, Hidalgo J, Bloch T. Prediction of blood volume in normal human adults. Surgery. 1962;51:224–32.

126. Yasui K, Lee J, Tuziuti T, Towata A, Kozuka T, Iida Y. Influence of the bubble-bubble interaction on destruction of encapsulated microbubbles under ultrasound. J Acoust Soc Am. 2009;126:973–82.

127. Morioka M. Theory of natural frequencies of two pulsating bubbles in infinite liquid. J Nucl Sci Technol. 1974;11:554–60.

128. Feuillade C. Scattering from collective modes of air bubbles in water and the physical mechanism of superresonances. J Acoust Soc Am. 1995;98:1178–90.

129. Weston DE. Acoustic Interaction Effects in Arrays of Small Spheres. J Acoust Soc Am. 1966;39:316–22.

130. Hsiao PY, Devaud M, Bacri JC. Acoustic coupling between two air bubbles in water. Eur Phys J E. 2001;4:5–10.

131. Payne EMB, Ooi A, Manasseh R. Symmetric mode resonance of bubbles near a rigid boundary - The nonlinear case with time delay effects. Proc 16th Australas Fluid Mech Conf. 2007;1336–9.

132. Accusizer: Single Particle Optical Sizing. Port Richey, FL; 2014.

133. Helfield B, Chen X, Qin B, Villanueva FS. Individual lipid encapsulated microbubble radial oscillations: Effects of fluid viscosity. J Acoust Soc Am. 2016;139:204–14.

134. Helfield B, Black JJ, Qin B, Pacella J, Chen X, Villanueva FS. Fluid Viscosity Affects the Fragmentation and Inertial Cavitation Threshold of Lipid-Encapsulated Microbubbles. Ultrasound Med Biol. 2016;42:782–94.

135. Thomas DH, Sboros V, Emmer M, Vos H, Jong N. Microbubble oscillations in capillary tubes. IEEE Trans Ultrason Ferroelectr Freq Control. 2013;60:105–14.

136. Caskey CF, Kruse DE, Dayton PA, Kitano TK, Ferrara KW. Microbubble oscillation in tubes with diameters of 12, 25, and 195 microns. Appl Phys Lett. 2006;88:1–3.

137. Sassaroli E, Hynynen K. On the impact of vessel size on the threshold of bubble collapse. Appl Phys Lett. 2006;89:1–3.

138. Wilson SR, Burns PN. Microbubble-enhanced US in Body Imaging: What Role? Radiology. 2010;257:24–39.

139. Shankar PM, Krishna PD, Newhouse VL. Advantages of subharmonic over second harmonic backscatter for contrast- to-tissue echo enhancement. Ultrasound Med Biol. 1998;24:395–9.

140. Heath Martin K, Lindsey BD, Ma J, Lee M, Li S, Stuart Foster F, et al. Dual-Frequency piezoelectric transducers for contrast enhanced ultrasound imaging. Sensors. 2014;14:20825–42.

141. Yang J, Cherin E, Yin J, Newsome IG, Pang G, Ivanytskyy O, et al. Characterization of an Array-Based Dual-Frequency Transducer for Superharmonic Contrast Imaging. IEEE Trans Ultrason Ferroelectr Freq Control. 2021;in press.

142. Newsome IG, Kierski TM, Dayton PA. Assessment of the Superharmonic Response of Microbubble Contrast Agents for Acoustic Angiography as a Function of Microbubble Parameters. Ultrasound Med Biol. 2019;45:2515–24.

143. Fix SM, Papadopoulou V, Velds H, Kasoji SK, Rivera JN, Borden MA, et al. Oxygen microbubbles improve radiotherapy tumor control in a rat fibrosarcoma model – A preliminary study. PLoS One. 2018;13:e0195667.

144. Santin MD, King DA, Foiret J, Haak A, O'Brien WDJ, Bridal SL. Encapsulated contrast microbubble radial oscillation associated with postexcitation pressure peaks. J Acoust Soc

Am. 2010;127:1156–64.

145. Cherin E, Yin J, Forbrich A, White C, Dayton PA, Foster FS, et al. In Vitro Superharmonic Contrast Imaging Using a Hybrid Dual-Frequency Probe. Ultrasound Med Biol. 2019;45:2525–39.

146. Stephens DN, Kruse DE, Ergun AS, Barnes S, Lu XM, Ferrara KW. Efficient array design for sonotherapy. Phys Med Biol. 2008;53:3943–69.

147. Li S, Kim J, Wang Z, Kasoji S, Lindsey BD, Dayton PA, et al. A dual-frequency colinear array for acoustic angiography in prostate cancer evaluation. IEEE Trans Ultrason Ferroelectr Freq Control. 2018;65:2418–28.

148. Martin KH, Lindsey BD, Ma J, Nichols TC, Jiang X, Dayton PA. Ex Vivo Porcine Arterial and Chorioallantoic Membrane Acoustic Angiography Using Dual-Frequency Intravascular Ultrasound Probes. Ultrasound Med Biol. 2016;42:2294–307.

149. Lindsey BD, Kim J, Dayton PA, Jiang X. Dual-Frequency Piezoelectric Endoscopic Transducer for Imaging Vascular Invasion in Pancreatic Cancer. IEEE Trans Ultrason Ferroelectr Freq Control. 2017;64:1078–86.

150. Newsome IG, Dayton PA. Visualization of Microvascular Angiogenesis Using Dual-Frequency Contrast-Enhanced Acoustic Angiography: A Review. Ultrasound Med Biol. 2020;46:2625–35.

151. Betzig E, Patterson GH, Sougrat R, Lindwasser OW, Olenych S, Bonifacino JS, et al. Imaging intracellular fluorescent proteins at nanometer resolution. Science. 2006;313:1642–5.

152. Noone AM, Howlader N, Krapcho M, Miller D, Brest A, Yu M, et al. SEER Cancer Statistics Review, 1975-2015. Bethesda, MD; 2018.

153. Allison KH, Abraham LA, Weaver DL, Tosteson AN, Nelson HD, Onega T, et al. Trends in Breast Tissue Sampling and Pathology Diagnoses among Women Undergoing Mammography in the U.S.: A Report from the Breast Cancer Surveillance Consortium. Cancer. 2015;121:1369–78.

154. Irvin VL, Kaplan RM. Screening Mammography & Breast Cancer Mortality: Meta-Analysis of Quasi-Experimental Studies. PLoS One. 2014;9:e98105.

155. Balleyguier C, Ayadi S, Nguyen K Van, Vanel D, Dromain C, Sigal R. BIRADS classification in mammography. Eur J Radiol. 2007;61:192–4.

156. Weaver DL, Rosenberg RD, Barlow WE, Ichikawa L, Carney PA, Kerlikowske K, et al. Pathologic findings from the breast cancer surveillance consortium: Population-based outcomes in women undergoing biopsy after screening mammography. Cancer. 2006;106:732–42.

157. Vlahiotis A, Griffin B, Stavros AT, Margolis J. Analysis of utilization patterns and associated costs of the breast imaging and diagnostic procedures after screening mammography. Clin Outcomes Res. 2018;10:157–67.

158. Berg WA, Bandos AI, Mendelson EB, Lehrer D, Jong RA, Pisano ED. Ultrasound as the primary screening test for breast cancer: Analysis from ACRIN 6666. J Natl Cancer Inst. 2016;108:dvj367.

159. Carmeliet P, Jain RK. Molecular mechanisms and clinical applications of angiogenesis. Nature. 2011;473:298–307.

160. Newsome IG, Kierski TM, Pang G, Yin J, Yang J, Cherin E, et al. Implementation of a novel 288-element dual-frequency array for acoustic angiography: in vitro & in vivo characterization. IEEE Trans Ultrason Ferroelectr Freq Control. 2021;in press.

161. Fedorov A, Beichel R, Kalpathy-Cramer J, Finet J, Fillion-Robin J-C, Pujol S, et al. 3D Slicer as an Image Computing Platform for the Quantitative Imaging Network. Magn Reson Imaging. 2012;30:1323–41.

162. Yu J, Yoon H, Khalifa YM, Emelianov SY. Design of a Volumetric Imaging Sequence Using a Vantage-256 Ultrasound Research Platform Multiplexed with a 1024-Element Fully Sampled Matrix Array. IEEE Trans Ultrason Ferroelectr Freq Control. 2020;67:248–57.

163. Démoré CEM, Joyce A, Wall K, Lockwood G. Real-time volume imaging using a crossed electrode array. IEEE Trans Ultrason Ferroelectr Freq Control. 2009;56:1252–61.

164. Jensen JA, Ommen ML, Øygard SH, Schou M, Sams T, Stuart MB, et al. Three-Dimensional Super-Resolution Imaging Using a Row – Column Array. IEEE Trans Ultrason Ferroelectr Freq Control. 2020;67:538–46.

165. Jain RK. Normalizing tumor microenvironment to treat cancer: Bench to bedside to biomarkers. J Clin Oncol. 2013;31:2205–18.

166. Zheng H, Kruse DE, Stephens DN, Ferrara KW, Sutcliffe P, Gardner E. A sensitive ultrasonic imaging method for targeted contrast microbubble detection. Proc 30th Annu Int Conf IEEE Eng Med Biol Soc EMBS'08 - "Personalized Healthc through Technol. 2008. page 5290–3.

167. Newsome IG, Kierski TM, Dayton PA. Assessment of the Superharmonic Response of Microbubble Contrast Agents for Acoustic Angiography as a Function of Microbubble Parameters. Ultrasound Med Biol. 2019;45:2515–24.

168. Humphrey VF. Nonlinear propagation in ultrasonic fields: Measurements, modelling and harmonic imaging. Ultrasonics. 2000;38:267–72.

169. Hayes WD, Runyan HL. Sonic-Boom Propagation through a Stratified Atmosphere. J Acoust Soc Am. 1972;51:695–701.

170. Luquet D, Marchiano R, Coulouvrat F. Long range numerical simulation of acoustical shock waves in a 3D moving heterogeneous and absorbing medium. J Comput Phys. 2019;379:237–61.

171. O'Donnell M, Jaynes ET, Miller JG. Kramers-kronig relationship between ultrasonic attenuation and phase velocity. J Acoust Soc Am. 1981;69:696–701.

172. Giammarinaro B, Coulouvrat F, Pinton G. Numerical Simulation of Focused Shock Shear Waves in Soft Solids and a Two-Dimensional Nonlinear Homogeneous Model of the Brain. J Biomech Eng. 2016;138:1–12.

173. Strang G. On the construction and comparison of different schemes. SIAM J Numer Anal. 1968;5:506–17.

174. Espíndola D, Lee S, Pinton G. Shear Shock Waves Observed in the Brain. Phys Rev Appl. 2017;8:1–9.

175. Marmottant P, van der Meer S, Emmer M, Versluis M, de Jong N, Hilgenfeldt S, et al. A model for large amplitude oscillations of coated bubbles accounting for buckling and rupture. J Acoust Soc Am. 2005;118:3499–505.

176. King DA, O'Brien WDJ. Comparison between maximum radial expansion of ultrasound contrast agents and experimental postexcitation signal results. J Acoust Soc Am. 2011;129:114–21.

177. Paul S, Katiyar A, Sarkar K, Chatterjee D, Shi WT, Forsberg F. Material characterization of the encapsulation of an ultrasound contrast microbubble and its subharmonic response: Strain-softening interfacial elasticity model. J Acoust Soc Am. 2010;127:3846–57.

178. Helfield BL, Goertz DE. Nonlinear resonance behavior and linear shell estimates for Definity™ and MicroMarker™ assessed with acoustic microbubble spectroscopy. J Acoust Soc Am. 2013;133:1158–68.

179. Faez T, Goertz D, De Jong N. Characterization of Definity™ Ultrasound Contrast Agent at Frequency Range of 5-15 MHz. Ultrasound Med Biol. 2011;37:338–42.

180. Chomas JE, Dayton P, May D, Ferrara K. Threshold of fragmentation for ultrasonic contrast agents. J Biomed Opt. 2001;6:141.

181. Vokurka K. On Rayleigh's model of a freely oscillating bubble. I. Basic relations. Czechoslov J Phys. 1985;35:28–40.

182. Azhari H. Appendix A: Typical Acoustic Properties of Tissues. Basics Biomed Ultrasound Eng. John Wiley & Sons, Inc.; 2010. page 313–4.

183. Zheng H, Barker A, Shandas R. Predicting backscatter characteristics from micron- And submicron- Scale ultrasound contrast agents using a size-integration technique. IEEE Trans Ultrason Ferroelectr Freq Control. 2006;53:639–44.

184. Lumason Package Insert. Monroe Township, NJ; 2016.

185. Newsome IG, Lindsey BD, Shelton SE, Cherin E, Yin J, Foster FS, et al. Characterization of a prototype transmit 2 MHz receive 21 MHz array for superharmonic imaging. Proc - IEEE Int Ultrason Symp. 2017;20–2.

186. Christensen-Jeffries K, Couture O, Dayton PA, Eldar YC, Hynynen K, Kiessling F, et al. Super-resolution Ultrasound Imaging. Ultrasound Med Biol. 2020;46:865–91.

187. Khuri-Yakub BT, Oralkan Ö. Capacitive micromachined ultrasonic transducers for medical imaging and therapy. J Micromechanics Microengineering. 2011;21:054004–14.

188. Mahmud MM, Wu X, Sanders JL, Biliroglu AO, Adelegan OJ, Newsome IG, et al. An Improved CMUT Structure Enabling Release and Collapse of the Plate in the Same Tx/Rx Cycle for Dual-Frequency Acoustic Angiography. IEEE Trans Ultrason Ferroelectr Freq Control. 2020;67:2291–302.

189. Sanders JL, Biliroglu AO, Newsome IG, Adelegan OJ, Yamaner FY, Dayton PA, et al. An Ultra-Wideband Capacitive Micromachined Ultrasonic Transducer (CMUT) Array for Acoustic Angiography: Preliminary Results. Proc - IEEE Int Ultrason Symp. 2020;

190. Shultz LD, Brehm MA, Garcia JV, Greiner DL. Humanized mice for immune system investigation: progress, promise and challenges. Nat Rev Immunol. 2012;12:786–98.

191. Chong DC, Yu Z, Brighton HE, Bear JE, Bautch VL. Tortuous Microvessels Contribute to Wound Healing via Sprouting Angiogenesis. Arterioscler Thromb Vasc Biol. 2017;37:1903–12.

192. Erickson BJ, Korfiatis P, Akkus Z, Kline TL. Machine learning for medical imaging. Radiographics. 2017;37:505–15.

193. Van Sloun RJG, Demi L. Localizing B-Lines in Lung Ultrasonography by Weakly Supervised Deep Learning, In-Vivo Results. IEEE J Biomed Heal Informatics. 2020;24:957–64.

194. Tan M, Le Q V. EfficientNet: Rethinking model scaling for convolutional neural networks. arXiv. 2019;1905.11946v5.